DEVELOPMENT OF SOLAR CELLS BASED ON SURFACE PASSIVATED LEAD TELLURIDE QUANTUM DOTS AND LEAD SELENIDE NANORODS; A COMPREHENSIVE APPROACH TARGETING THE INSTABILITY AND SURFACE MEDIATED TRAP STATES

A THESIS SUBMITTED TO
THE GRADUATE SCHOOL OF NATURAL AND APPLIED SCIENCES
OF
MIDDLE EAST TECHNICAL UNIVERSITY

BY

TUĞBA HACIEFENDIOĞLU

IN PARTIAL FULFILLMENT OF THE REQUIREMENTS
FOR
THE DEGREE OF MASTER OF SCIENCE
IN
CHEMISTRY

JANUARY 2020

Approval of the thesis:

DEVELOPMENT OF SOLAR CELLS BASED ON SURFACE PASSIVATED LEAD TELLURIDE QUANTUM DOTS AND LEAD SELENIDE NANORODS; A COMPREHENSIVE APPROACH TARGETING THE INSTABILITY AND SURFACE MEDIATED TRAP STATES

submitted by **TUĞBA HACIEFENDİOĞLU** in partial fulfillment of the requirements for the degree of **Master of Science in Chemistry Department, Middle East Technical University** by,

Prof. Dr. Halil Kalıpçılar
Dean, Graduate School of **Natural and Applied Sciences** __________________

Prof. Dr. Cihangir Tanyeli
Head of Department, **Chemistry** __________________

Assist. Prof. Dr. Demet Asil Alptekin
Supervisor, **Chemistry, METU** __________________

Examining Committee Members:

Prof. Dr. Ahmet Muhtar Önal
Chemistry, Middle East Technical University __________________

Assist. Prof. Dr. Demet Asil Alptekin
Chemistry, METU __________________

Prof. Dr. Mehmet Parlak
Physics, Middle East Technical University __________________

Prof. Dr. Atilla Cihaner
Chemical Engineering and Applied Chemistry, Atılım University__________________

Assist. Prof. Dr. Erol Yıldırım
Chemistry, Middle East Technical University __________________

Date: 10.01.2020

I hereby declare that all information in this document has been obtained and presented in accordance with academic rules and ethical conduct. I also declare that, as required by these rules and conduct, I have fully cited and referenced all material and results that are not original to this work.

Name, Surname: Tuğba Hacıefendioğlu

Signature:

ABSTRACT

DEVELOPMENT OF SOLAR CELLS BASED ON SURFACE PASSIVATED LEAD TELLURIDE QUANTUM DOTS AND LEAD SELENIDE NANORODS; A COMPREHENSIVE APPROACH TARGETING THE INSTABILITY AND SURFACE MEDIATED TRAP STATES

Hacıefendioğlu, Tuğba
Master of Science, Chemistry
Supervisor: Assist. Prof. Dr. Demet Asil Alptekin

January 2020, 82 pages

One of the underlying reasons for the 33% theoretical limit of solar cells (Shockley–Queisser limit) is the losses originating from non-absorbed ultra violet and infrared regions of the solar spectrum. PbTe Quantum Dots-(QDs) and PbSe Nanorods-(NRs) are two of the intriguing nanocrystals which can be utilized to overcome the efficiency limit due to unique properties such as band gap tunability, large exciton Bohr radius and highly absorbing nature in ultra-violet and infrared regions. However, air instability and limited knowledge on the surface properties hinder their utilization in the field of optoelectronics. In this respect, a detailed understanding on the instability of those nanocrystals was presented and combinatorial passivation protocols based on engineering of the surface during the growth phase and solid-state ligand exchange process were developed. Dual passivation approach controls shape, ligand exchange rate, packing direction and mid gap state formation by dictating the {111}/ {200} facet ratio and yield solar cells with outstanding stabilities. Optical properties, stability behavior and band energies depend mainly on the aspect ratio of the NRs which is tuned by reaction parameters such as injection temperature, concentration of oleic acid and diphenylphosphine. We also found that the ligand choice was the key factor in improving the solar cell performance as affecting the thin film morphology by controlling the NR packing. Optimization of the cell fabrication protocols yields PbSe NR based solar cells with 80% external quantum efficiency (EQE) and 2.60% power conversion efficiency (PCE) and enhanced stability up to 54 days under inert atmosphere for the first time in literature.

Keywords: Quantum Dot, Nanorod, Surface Modification, Stability, Solar Cells

ÖZ

YÜZEY MODİFİKASYONU YAPILMIŞ KURŞUN TELERYUM KUANTUM NOKTA VE KURŞUN SELENYUM NANOÇUBUK TEMELLİ GÜNEŞ HÜCRELERİNİN GELİŞTİRİLMESİ; KARARSIZLIĞIN VE YÜZEY KAYNAKLI TUZAK BANTLARININ ORTADAN KALDIRILMASI

Hacıefendioğlu, Tuğba
Yüksek Lisans, Kimya
Tez Danışmanı: Dr. Öğr. Üyesi Demet Asil Alptekin

Ocak 2020, 82 sayfa

Güneş hücrelerinin %33 lük teorik limitinin (Shockley-Queisser limiti) altında yatan temel sebeplerden biri, morötesi ve kızılötesi bölgelere karşılık gelen dalga boylarının soğrulmamasından kaynaklanmaktadır. PbTe kuantum noktaları ve PbSe nanoçubuklar gibi kurşun kalkojenitlerin bu bölgelerdeki yüksek derecede soğurabilme yeteneği, ayarlanabilir bant aralığı ve yüksek eksiton Bohr yarıçapı gibi benzersiz özellikleri teorik verim limitlerin ötesine geçme konusunda mükemmel adaylar haline getirir. Ancak oksijene karşı olan duyarlılıkları ve yüzey morfolojileri hakkındaki sınırlı bilgi birikimi bu nanokristallerin üstün özelliklerini ve optoelektronik alanlardaki kullanımlarını sınırlamaktadır. Bu bağlamda, bu çalışmada bahsedilen nanokristallerin oksijen ortamına karşı duyarlılıkları hakkında ayrıntılı bir yaklaşım sunulmuş, sentez sırasında ve katı halde yüzey modifikasyonlarının bu nanokristallere etkisi incelenmiştir. Geliştirilen ikili yüzey modifikasyonu {111}/{200} faset oranı ve miktarını değiştirerek PbTe kuantum noktaların şeklini, reaktif değişim oranını, paketlenme örgüsünü ve ara bant oluşumunu etkilemektedir. Sonuç olarak, geliştirilen bu teknik ile atmosferik koşullar altında olağanüstü kararlılığa sahip PbTe kuantum nokta bazlı güneş hücrelerinin üretilmesi mümkün kılmıştır. PbSe nanoçubuklarının foto-fiziksel özellikleri ve kararlılık davranışı en boy oranına bağlı olarak yüksek değişkenlik gösterdiği bulunmuştur. Nanoçubuk en-boy oranı, enjeksiyon sıcaklığı, oleik asit ve difenilfosfin konsantrasyonu gibi bazı reaksiyon parametreleri ile ayarlanmıştır. Ayrıca, ligand yer değiştirme esnasında kullanılan yüzey reaktifi seçiminin ince film morfolojisi, foto-fiziksel özellikler ve hücre performansını etkileyen en önemli parametrelerden biri olduğu bulunmuştur. Sonuç olarak, literatürde ilk kez atmosferik koşullar altında 54 güne kadar kararlılığını koruyan, %80 harici kuantum verimi ve %2.6 hücre verimine sahip PbSe nanoçubuk güneş hücreleri geliştirilmiştir.

Anahtar Kelimeler: Kuantum Nokta, Nanoçubuk, Yüzey Modifikasyonu, Kararlılık, Güneş Hücresi

To my beloved family...

ACKNOWLEDGEMENTS

First and foremost, my grateful thank goes to my mom, dad and brothers for their wonderful support in my life. Without their support, unconditional love and understanding, I have never ever would be same person to come to this point in my journey.

My deepest gratitude for Assoc. Prof. Dr. Demet Asil Alptekin I would like to thank her for being a truly unique and wonderful supervisor. I am grateful for her excellent patience, guidance and support.

Also, I extend thanks to all members of our research lab for their friendship, support and help during this study.

I would like to thank to Prof. Dr. Atilla Cihaner from Atılım University for giving us to opportunity to use his solar cell fabrication facilities at ATOMSEL. Also, Thanks to Assoc. Prof. Dr. Emrullah Görkem Günbaş to allows me use his laboratory for the thermal evaporator system and Dr. İbrahim Murat Öztürk for maintaining the photoluminescence set-up. In addition, I thank to METU Central Laboratory staff for TEM, XRD, XPS and SEM measurements. I am also grateful to Scientific and Technological Research Council of Turkey (TÜBİTAK) for the financial support (Project Number: 115F187 and 117E787) and Research Fund of the Middle East Technical University (Project Number: BAP-08- 11-2016-061 and 10154).

For days and nights, this was not an easy journey to be calm, dedicated and motivated all the time, since sometimes I failed, and failed again. However, I always motivate myself with the help of some special people. First, I owe a debt of gratitude to Özgün Aydın to be with me in every single part of my thesis study. Then, I would like to thank to Dilara Görüm for her special friendship and support.

TABLE OF CONTENTS

CHAPTERS

LIST OF TABLES

TABLES

LIST OF FIGURES

FIGURES

LIST OF ABBREVIATIONS

ABBREVIATIONS

ACN : Acetonitrile

BDT :1,3-Benzenedithiol

DCM : Dicholoromethane

DMF : Dimethylformamide

DPP : Diphenylphosphine

EDT : Ethanedithiol

E_G : Band gap

ETL : Electron transport layer

EQE : External quantum efficiency

FF : Fill factor

FTIR : Fourier-transform infrared spectroscopy

FWHM: Full width at half maximum

HDA : Hexadecylamine

HRTEM: High resolution transmission electron microscopy

Hyd. : Hydrazine

I_{MP} : Current at the maximum power point

I_{SC} : Short circuit current

IPA : Isopropyl alcohol

ITO : Indium Tin Oxide

IQE : Internal quantum efficiency

J_{SC} : Short circuit current density

LBL : Layer by layer

MEG : Multiple Exciton Generation

MGS : Mid gap state

MeOH : Methanol

NPs : Nanoparticles

NRs : Nanorods

NWs : Nanowires

OA : Oleic acid

ODE : Octadecene

PCE : Power conversion efficiency

PL : Photoluminescence

P_{MP} : Maximum power point

R_S : Series resistance

R_{SH} : Shunt resistance

QDs : Quantum dots

SAED : Selected area electron diffraction

SEM : Scanning electron microscopy

SynP : Growth phase surface passivation method

TBAI : Tetrabutylammonium Iodide

TCE : Tetrachloroethylene

TDP : Tris(diethylamino)phosphine

TDPA : Tetradecylphosphonic acid

TEM : Transmission Electron Microscopy

UP : Unpassivated

UPS : Ultra-Violet Photoelectron Spectroscopy

V_{MP} : Voltage at the maximum power point

V_{OC} : Open circuit voltage

XPS : X-Ray Photoelectron Spectroscopy

XRD : X-Ray Diffraction

TOP : Trioctylphosphine

TOPO : Trioctylphosphine oxide

TTIP : Titanium (IV) isopropoxide

CHAPTER 1

INTRODUCTION

What would the properties of materials be if we could really arrange the atoms the way we want them?

Richard Feynman, ‘’There’s Plenty of Room at the Bottom’’ Dec. 29 1959.

Beginning of the nanotechnology and nanoscience was depended on the lecture by physicist Richard Feynman at the California Institute of Technology on December 29, 1959. Feynman explained how scientist would be able to arrange, control and manipulate the atoms or molecules and over the years, nanotechnology and applications of nanoscience have been forefront for research studies.

Developments in optoelectronics also provide successful collaborations for nanostructured materials within this field. Improved and novel optoelectronics areas such as the application of energy harvesting, photodetectors and displays have been extensive and popular topics by solar energy market. For example, nanoparticle (NP) solar cells containing quantum dots (QDs), nanowires (NWs), or nanorods (NRs) are being developed as third generation solar cells. As the crystal silicon technology reaching its theoretical limits, third generation solar cells are being developed with the aim of harnessing solar energy in a more effective manner[1,2]. One of the underlying reasons for the 33% theoretical limit of today’s crystal silicon solar cells (Shockley–Queisser limit) is the losses originating from non-absorbed ultraviolet and infrared regions of the solar spectrum[3]. In this sense, extraordinary properties such as large exciton Bohr radius, band gap (E_G) tunability, multiple exciton generation and near-infrared absorption ability make lead chalcogenide NPs favorable and intriguing candidates for solar cell applications. However, challenges such as high air sensitivity and undiscovered surface properties of lead chalcogenide NPs limit their utilization in solar energy field.

In this study, a comprehensive approach targeting the instability and surface mediated trap states of PbTe QDs and PbSe NRs and also optoelectronic device applications of these NPs are discussed.

In Chapter 2, background information that helps to understand and examine the experimental study are given. First of all, brief information about the properties of QDs and their optoelectronic properties are provided. Synthesis methods for production of NPs as well as the working principle of solar cells are also discussed.

In Chapter 3, all the experimental methods used in this study are explained. Characterization, sample preparation, synthesis and purification techniques are also given in detail.

In Chapter 4, firstly surface chemistry of PbTe QDs are discussed and analysis of passivation methods for enhancing the air stability are given prior to the solar cell applications. Secondly, characterization of all synthetic conditions for PbSe NRs is explained, then the role of PbSe NRs in solar cell application is expressed.

In Chapter 5, conclusions for the characterization, stability and solar cell application studies for PbTe QDs and PbSe NRs are stated.

CHAPTER 2

BACKGROUND

2.1. Quantum Dots

Quantum dots which are also known as ‘artificial atoms’ are nanoparticles (NPs) of semiconductor materials, which are so small in size that the excitons are squeezed and exhibit 3-dimensional quantum confinement effect. Their unique chemical, physical and optoelectronic properties can be readily tuned via their synthesis (e.g. shape, size, and size distribution), making them intriguing candidates for use in applications including bio-imaging, solar cells, light emitting diodes, lasers, and infrared photodetectors.[1,4,5,6,7] Production of QDs matters as it directly controls the band gap (E_G) of the crystal.[8,9] Over the last few years, QDs have been explored due to their possibility to tune the bandgap that enables adaptation and optimization of the spectral absorption profile of these active materials to match the solar spectrum. Especially near-infrared active lead chalcogenides QDs like PbSe, PbTe, and PbS have been used for photovoltaic applications due to their efficient charge separation and transportation, quantum confinement effects, multiple excitons generation (MEG) ability, large light absorption coefficient and large Bohr radius.[8]

A natural length scale of electronic excitations in macroscopic (bulk) semiconductors is given by the exciton Bohr radius which is determined by the strength of the Coulomb interaction between electron and hole pair (exciton).[10] However, in ultrasmall (sub-10 nm) semiconductor elements belong to IV, III-V and II-VI groups this property shows some differences.[11] When their size is equal or smaller than Bohr radius, the dimensions of the NPs itself but not the strength of the electron and hole Coulomb coupling define the spatial distance of the electron and hole pair state. In this case, electronic energies are directly dependent on the degree of spatial confinement of electronic wave functions and NP dimensions, which is known as the quantum size effect.[10] With this effect, it is possible to change the band gap continuously, resulting in a control of the emission color and the spectral onset of the absorption.

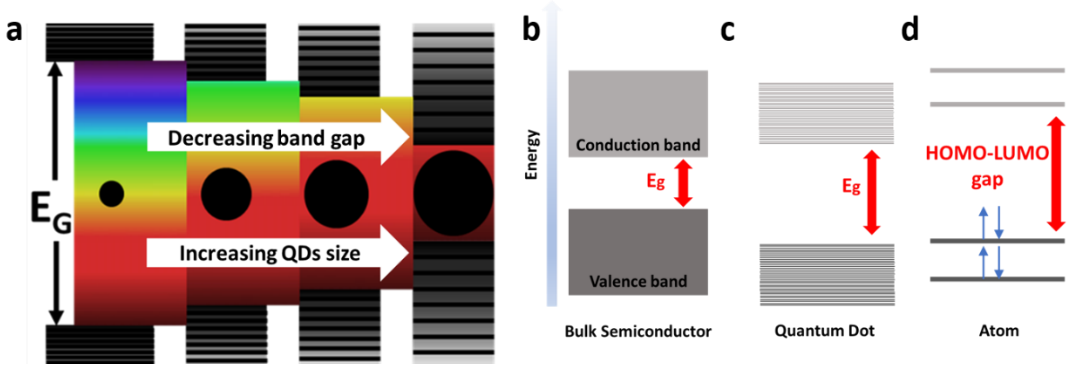

Figure 2.1. **a)** Schematic representation of relation between bandgap energy (E_G) and size of QDs. Band gap energy of **b)** bulk semiconductor, **c)** QDs and **d)** atom.

As shown in Figure 2.1-a, since the size of QDs decreases, the bandgap increases, causing a blue shift of the emission spectrum. This effect can be described using a simple particle-in-a-box potential model.[10] For a spherical QD with radius $\boldsymbol{r}$, this model predicts that the size-dependent contribution to the energy gap is simply proportional to $\boldsymbol{1}/_{\boldsymbol{r}^2}$. This relation can be explained by the Brus equation;

$$\boldsymbol{E_g(QD) \approx E_{g,0} + \frac{h^2}{8r^2}\left(\frac{1}{m_e^*} + \frac{1}{m_h^*}\right)}$$

where $\boldsymbol{E_g(QD)}$ is bandgap energy of QDs, $\boldsymbol{E_{g,0}}$ is bandgap energy of bulk semiconductor, $\boldsymbol{h}$ is Planck’s constant, $\boldsymbol{r}$ is radius of QD, $\boldsymbol{m_e^*}$ is effective mass of excited electron and $\boldsymbol{m_h^*}$ is effective mass of excited hole.[12] In addition to quantum-size effects, when the size of the QD reaches the size of the Bohr radius of material, just as the particle in a box, quantum confinement effect becomes dominant, leading to the a collapse of the continuous bands into a series of discrete atomic-like energy levels (Figure 2.1-c,d) in contrast to the bulk material as represented in Figure 2.1-b.

2.1.1. Hot Injection Nanoparticle Synthesis Method

A typical colloidal NP synthesis starts with the introduction of the molecular precursors into reaction medium, where the precursors undergo a chemical transformation forming active species (monomers) for the nucleation stage.[8] Following the homogeneous nucleation of NPs, growth takes place depending on the surface of the NPs as shown in Figure 2.2 where the concentration of the monomers is schematically plotted as a function of time.

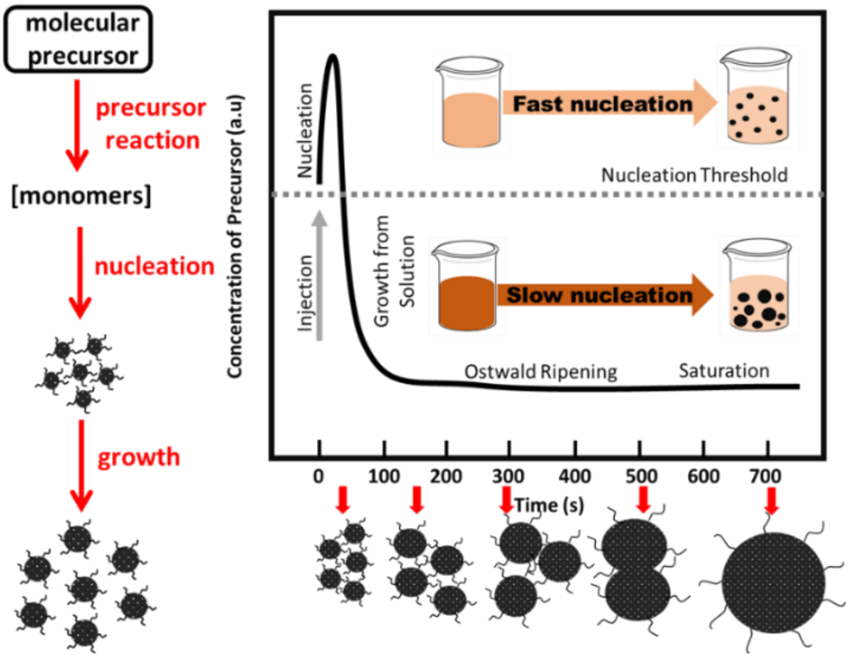

Figure 2.2. Schematic diagram of the nucleation and growth stages for synthesis of NPs using hot-injection method.

Depending on the time elapsed after the injection of the precursors, larger NPs can form by the dissolution of smaller NPs, named Ostwald ripening process. These three stages occur in the presence of capping ligands which are also known as stabilizers or surfactants. These capping molecules (ligands) such as long chain carboxylic acids, phosphonic acids, alkyl thiols, alkyl phosphines, alkyl phosphine oxides, and alkylamines have crucial roles in adjusting the kinetics of the nucleation and growth as they adhere to the surface of the NPs and provide colloidal and chemical stability.[13] In addition, the starting concentration of stabilizers affects the high quality and monodispersity of NPs.[14] Concentrated capping ligand causes slow nucleation resulting in a wide size distribution, while diluted concentration yields fast nucleation and homogeneously distributed size for forming NPs as illustrated in Figure 2.2. La Mer and others proposed a ‘’burst’’ nucleation concept that is related with a rapid nucleation occurring after the concentration of monomers passes the nucleation threshold.[15,16] Therefore, the technique in which one of the precursors are rapidly injected into another precursor in a hot solvent to form fast nucleation of monomers is called as hot injection method. Non-coordinating, chemically inert solvents that have high boiling point are preferred to widen the reaction temperature range.[10] Besides the speed of injection and capping ligand concentration, the temperature regime for injection and growth, growth time and precursor concentration affect the size and size distribution of the NPs.[17]

Typical reactions for the productions of II-VI (CdSe, CdTe, CdS), and IV-VI (PbS, PbSe, PbTe) NPs are listed by reactions 1 and 2.[13] For these synthesis, long-chain alkylphosphines such as trioctylphosphine (TOP), alkylamines such as hexadecylamine (HDA) and alkylphosphine oxides such as trioctylphosphine oxide (TOPO) are used as capping ligands at elevated injection temperature.[18] Due to the high sensitivity of lead, contact with oxygen is particularly important during the synthesis.[19] Prevention of oxidation is provided by using Schlenk techniques under dry inert atmosphere for the synthesis and nitrogen-filled glove box for the purification. A detailed explanation for NPs synthesis is given in Chapter 3.2 for the quantum dots and nanorods investigated in this thesis.

$$Cd(CH_3)_2 + (C_8H_{17})_3PSe \xrightarrow{300\ ^{\circ}C} CdSe\ NPs \qquad (1)$$

$$Pb(CH_3COO)_2 + (C_8H_{17})_3PSe \xrightarrow{260\ ^{\circ}C} PbSe\ NPs \qquad (2)$$

NP shape and morphology are controlled by the type and concentration of stabilizing agents during the synthesis. Capping ligands with selective adhesion lead for arranging the growth of different crystal facets and change the shape of NP from nearly round (0D) to highly anisotropic (1D, 2D, 3D) by increasing the surface area such as cubes, rods, hollow rings or stars.[20] Comparison of simple isotropic shaped inorganic NPs with anisotropic shaped NPs reveals the new physical and chemical properties of high surface area to volume ratio in the nanometer scale for anisotropic shaped NPs.[21] 0D morphologies contain the cubic, dodecahedral, octahedral, and tetrahedral shaped NPs while 1D structures cover nanorods, nanoneedles, nanowires, and hollow shaped NPs. Belts, sheets, and hollow rings are categorized as 2D, and more complex structures like nanoflowers, nano-stars belong to 3D shape family.[20] Besides the surfactants, temperature for injection and precipitation, additives, pH of the reaction medium, seeds and templates are other effective mediators for anisotropic driven morphology transitions.[21] As shown in transmission electron microscopy (TEM) images in Figure 2.3, PbSe QD and PbSe NRs were synthesized using trioctylphospine (TOP) and tris(diehylamino)phosphine (TDP) as stabilizing agents, respectively.

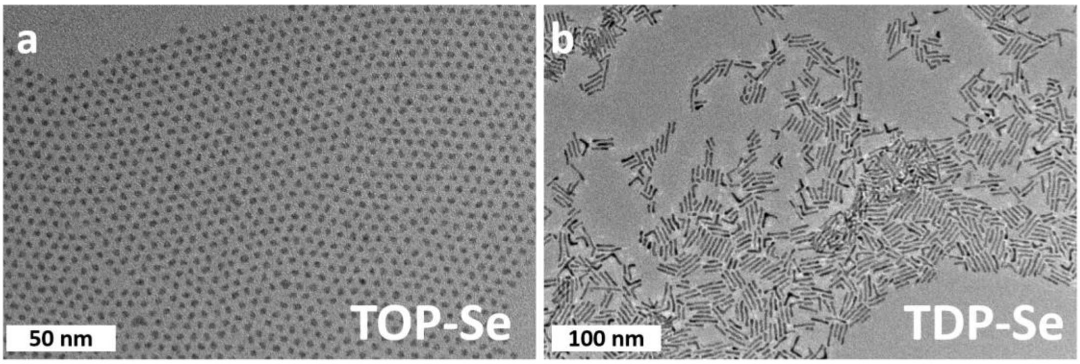

Figure 2.3. TEM images of **a)** PbSe QDs for which TOP is used as the stabilizing agent and **b)** PbSe NRs for which TDP is used as the stabilizing agent.

2.1.2. Defects and Air Instability

The surfactants (ligands) play critical roles in the production and application of colloidal lead chalcogenide NPs by proving stabilization in the solution, keeping charge balance on the surface and eliminating/reducing the trap states. The most widely used synthetical ligand types for lead chalcogenide NPs relies on the long hydrophobic saturated hydrocarbon chains with at least one anchoring end group. Shape and length of the ligands change the morphology and physicochemical properties of the formed particles. Long hydrocarbon ligands give rise to insulating and nonfunctional properties which are unsuitable for applications like bioimaging or optoelectronics. Hindered charge transport between the nanoparticles can be prevented by suitable and efficient ligand replacement on the surface of the particles. However, complete replacement of the organic ligands with any other functional or smaller surfactants has shown to be very challenging, as the surface traps can be created on surface atoms. Annealing can be a solution for removal of organic groups, however it can cause the sintering of NPs or remaining of some carbonaceous ligands on the surface of NPs.[13] The majority of successful elimination of these bulky ligands based on the replacement of them with smaller organic group like hydrazine, phenylenediamine, ethanethiol, pyridine or mercaptopropionic acid to improve the charge transfer by decreasing the spacing between the NPs. Besides organic molecules some inorganic molecules such as metal chalcogenide complexes (eg., Na_4SnS_6), metal-free chalcogenide complex (eg., HS^-), halides (eg., CI^-, Br^-or I^-)., or metal halide ligands (eg., CH_3NH_3X where X: CI^-, Br^-or I^-) can be used to passivate the trap states and improve the charge transport.[8]

There are some methods for the replacement of synthetic ligands with more useful ligands to enhance the stability and electron transfer between the particles. Growth phase ligand exchange, and solid-phase ligand passivation techniques are some of the commonly used methods for the modification of the surface of the NPs. These surface modification techniques are explained in detail in Chapter 3.4.

2.2. Solar Cells

Sun is an average star that has been burning for more than four billion years. It is an enormous source of energy and releases 95% of its output energy as light.[22] On the solar spectrum (Figure 2.4) visible (VIS) region detectable by the human eye has less energy than the ultraviolet (UV) region which cannot be seen but felt by the skin, and infrared (IR) region has less energy than the visible region. Direct sunlight on earth's atmosphere does not completely reach the ground. Most of the X-rays and the UV radiation are absorbed by the ozone, water, vapor and carbon dioxide with certain wavelengths through the atmosphere before arriving on the earth's surface. Some of the coming radiations are reflected back from the ground whereas some of the sunlight is scattered by the atmosphere.

Air mass (AM) is a term that is associated with the amount of sunlight at the surface of the earth and is related to the distance and angle of arriving radiation. Air mass zero (AM0) is considered where the region above the atmosphere in the absence of the atmospheric attenuation for solar radiation. There are also other spectra like AM1 and AM1.5 that are denoted for solar radiation under specified conditions like the angle of the arrival sunlight or tilt of the earth with respect to the sun.[23] AM1.5 (where the sun is about 41° above the horizon) spectra provide a standard calibration for photovoltaic (PV) cells corresponding to a particular set of conditions and air mass shown in Figure 2.4.[24] For AM1.5, total irradiance is 100 mW/cm^2 and the pressure is at sea level under standard pressure (1013.25 millibars).[25]

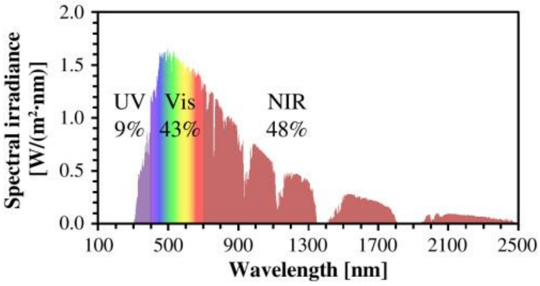

Figure 2.4. Solar energy distribution of sun on the earth's atmosphere at AM1.5 spectrum.[26]

The photovoltaic effect was first observed in 1839 by Alexandre Edmund Becquerel. Around 1880, Charles Fritts created the first photovoltaic of selenium resulting in 1% efficiency.[27] After 1953, scientists from Bell Laboratories figured out that silicon is more efficient than selenium to be used in practical photovoltaics.[28] In 1994, the efficiency of the conversion was scaled up to 30% with a cell made from gallium indium phosphide and gallium arsenide by National Renewable Energy Laboratory (NREL). Today, with the growing demand for renewable energy, research and development studies for efficient and inexpensive photovoltaics are conducted all over the world and best efficiencies are shown in the chart represented in Figure 2.5.

2.2.1. Working Principle of Solar Cells

Solar cells are basic photovoltaics that allow photons to knock electrons free from a atom and generate electricity. In general, the power of the devices is expressed with power conversion efficiency (PCE). PCE depends on various parameters like type of material, design of layers, preparation method or incident radiation. The efficiency of a device can be deducted from I-V characteristics at a certain temperature and irradiance. Parameters calculated from the I-V characteristics of the cells are open circuit voltage (V_{OC}), short circuit current (I_{SC}), fill factor (FF), efficiency (η), shunt resistance (R_{SH}) and series resistance (R_S).

Isc, short circuit current is the maximum current that flows through the cell without damaging its own construction. It is measured when the voltage of the cell equals to zero where the electrodes are short circuited. I_{SC} is related to the carriers which are created and collected after illumination. Therefore, it depends on the incident solar radiation and illumination area. It is generally expressed as short circuit density (J_{SC}) by removing the area dependency. J_{SC} can be formulated as;

$$J_{SC} = \frac{I_{SC}}{A}$$

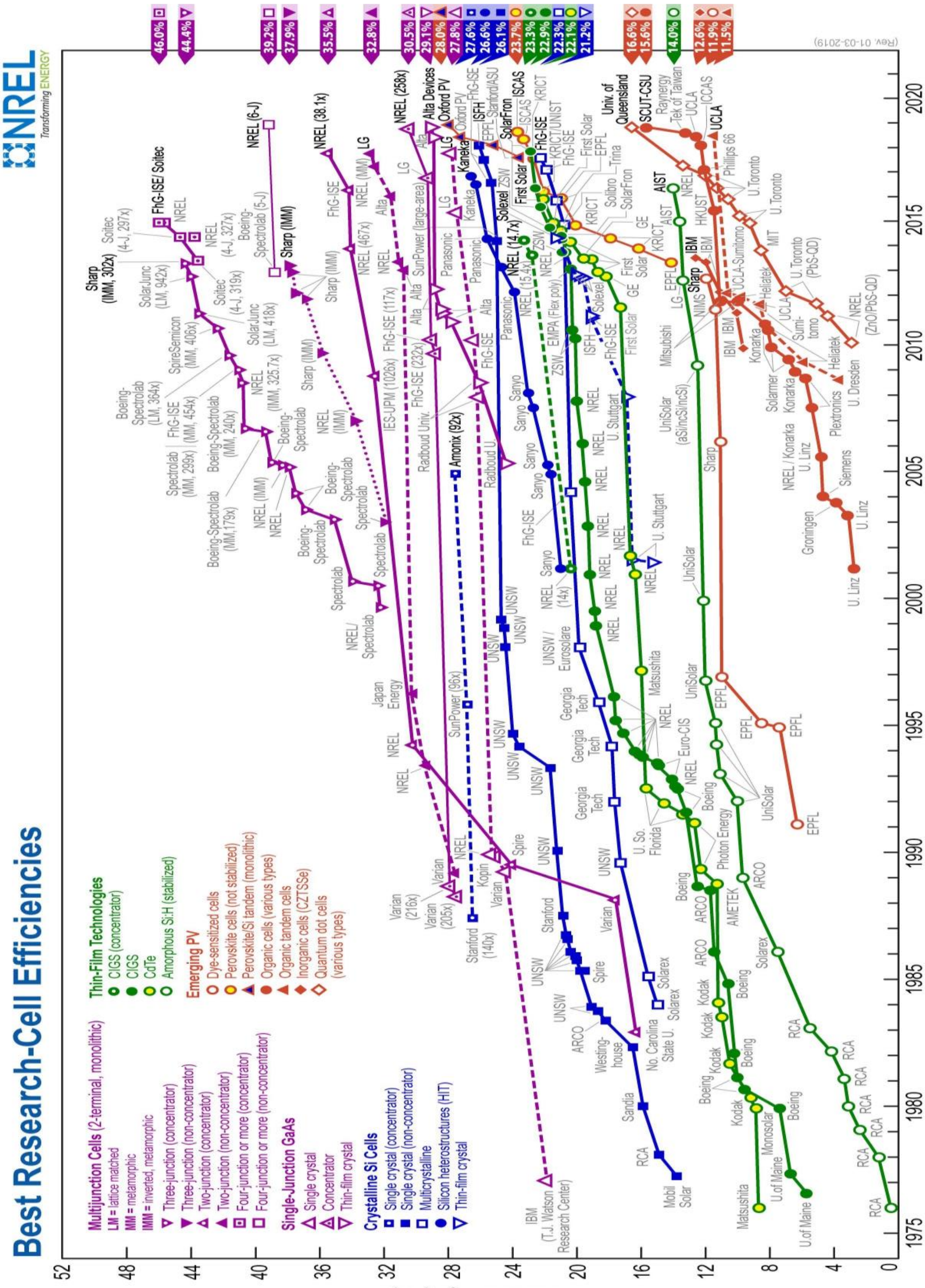

Figure 2.5. Chart of the best efficiencies for different type of solar cells. [29]

where, the A is illuminated area of the solar cell.[10]

V_{OC}, open circuit voltage is the maximum voltage that is measured when there is no flow of current through the device. For an ideal solar cell, it does not depend on the incident light or the area of the solar cell, but photo-generated current, the temperature and construction of the device. V_{OC} can be formulated as;

$$V_{OC} = \frac{E_G}{q} - \eta k_B T \ln \frac{J_0}{J_L}$$

where, E_G is bandgap of the active material used in the solar cell, q is the elementary charge, η is the ideality factor, k_B is the Boltzmann constant, T is the temperature of the solar cell, J_0 is the reverse saturation current and J_L is the photocurrent.[30] Assuming the net charge in the solar cell is zero, it is derived that increase in temperatures has a decreasing impact on Voc of the cell.

FF, fill factor is the ratio of maximum power point (P_{MP}) to the product of J_{SC} and V_{OC}. The maximum power is calculated from the product of current and voltage at the maximum power point (I_{MP}, V_{MP}).[10] It can be calculated by following equation.

$$FF = \frac{P_{MP}}{V_{OC} I_{SC}} = \frac{V_{MP} I_{MP}}{V_{OC} I_{SC}}$$

Efficiency of a solar cell is expressed as a percentage of a ratio between the maximum electrical power output and incident radiation.[10] The incident light is described by the AM1.5 spectrum and has an irradiance of P_{in} is 1000 W/m^2. It can be formulated as;

$$\text{Efficiency}(\eta) = \frac{P_{MP}}{P_{in}} = \frac{I_{SC} V_{OC} FF}{P_{in}\ A} = \frac{J_{SC} V_{OC} FF}{P_{in}}$$

All parameters are shown on the I-V characteristics as represented in Figure 2.6. [22]

The other parameters are shunt and series resistance which are denoted as R_{SH} and R_S, respectively. Series resistance is generally caused by contact resistance between the metal contact and the active material, rear and top metal contact problems or current

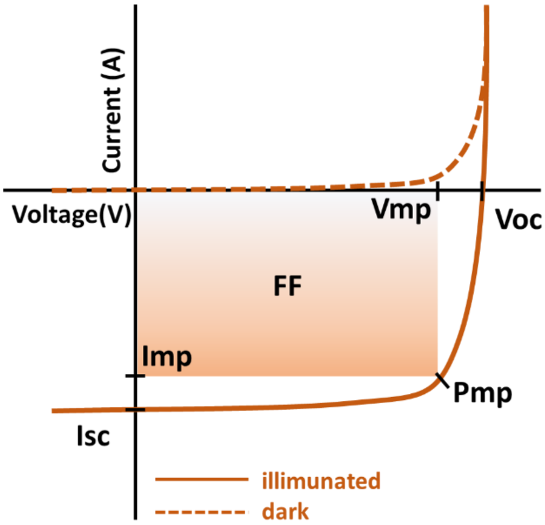

Figure 2.6. I-V characteristics of solar cell. [22]

movement problems through the active material.[31] It has a decreasing impact on the FF. It can be simply estimated from the slope of the point of V_{OC} on the I-V curve. Not poor solar cell design, but defects formed during the fabrication of cell can cause a significant power loss in solar cell and this brings a shunt resistance with itself. The presence of shunt resistance leads some paths for current flow and this brings together a decrease in J_{SC} and V_{OC} parameters.[32] Basically, the estimation of the R_{SH} is possible by calculating the slope of the point of J_{SC} on I-V curve.

Besides the I-V characteristics, there is also a key parameter for solar cell characterization which is the external quantum efficiency (EQE). EQE is the ratio of the number of the extracted charge carriers to the number of the incident photons on the solar cell. EQE is given as a function of wavelength or energy of the incident light. If all incident photons are absorbed by the active materials in the solar cell, and all created charge carriers are collected from the electrodes of the solar cell then the external quantum efficiency is 100%. However, there are some reflective and transmissive losses outside of the active layer. Therefore, quantum efficiency can be categorized as EQE and internal quantum efficiency (IQE). The EQE of a solar cell counts in the effect of these optical losses while IQE refers to the efficiency with which photons that are not reflected or transmitted out of the cell can generate collectable carriers. That is why the value of IQE is always higher than EQE.[33] Quantum efficiency is formulated as;

$$QE = \frac{100\% * h * c * I_{cell}(\lambda)}{e * \lambda * I_{ref}(\lambda) * R(\lambda)}$$

where, h is Planck’s constant, c is speed of light, $I_{cell}(\lambda)$ is current of measuring cell, $I_{ref}(\lambda)$ is current of calibrated reference cell and $R(\lambda)$ is known responsivity value of the reference cell.[34] EQE and IQE are also formulized as;

$$EQE = \frac{number\ of\ the\ collected\ charge\ carriers\ from\ solar\ cell}{number\ of\ the\ incident\ photons\ to\ the\ solar\ cell}$$

$$IQE = \frac{number\ of\ the\ collected\ charge\ carriers\ from\ solar\ cell}{number\ of\ the\ absorbed\ incident\ photons\ from\ the\ solar\ cell}$$

When the light or photons come and knock the electron free in the active material, electrons absorb the energy and jump into a higher energy level. Excited electrons and the holes left at the ground state are loosely bound to each other and are called as excitons. Extractions of the electrons and holes from the opposite electrodes create electricity. However, duration of the electron staying on the excited state is so small that a successful collection of the charge carriers may be very challenging. The process of electrons meeting a hole is called as recombination and it is one of the major reasons for the decreases in the PCE of the solar cell.

Solar cells are categorized as first, second and third generation.[35] First-generation solar cells are the most efficient and durable solar cells that consist of monocrystalline silicon, polycrystalline silicon, and amorphous silicon solar cells. Second-generation solar cells which are called as thin film solar cells consist of micrometer thick layered semiconductor active material. Cadmium telluride (CdTe) solar cells and copper indium gallium diselenide (CIGD) solar cells are in this category that have a lower manufacturing cost with respect to the first-generation solar cells. [35] Third generation solar cell category consists of brand-new materials like inks, nanotubes, nano wires, nanoparticles or conductive polymers. Although the efficiencies of third generation solar cells are way behind the first generation solar cells, lowering fabrication costs and enhanced efficiency by widening the absorption spectrum matching the solar radiation spectrum makes third generation solar cells are favorable and intriguing.

The absorption of the light in semiconductors materials is restricted with the bandgap of the material. Semiconductors can absorb the incident light if the bandgap of the material is equal or smaller than the energy of the photon. Besides this limit, there is also a detailed balance limit which is called as Shockley-Queisser limit. Shockley-Queisser is a physical theoretical limit that refers to the maximum achievable power conversion efficiency from a photovoltaic.[36] It is calculated as 33% for a single-junction solar cell, and 47% of solar loss is caused by the conversion of heat, 18% of loss is a result of photons passing through the active material in solar cell and recombination of charge carriers is made of the 2% of the total loss.[37] Recent studies show that some of the third generation solar cells offer a potential to break the theoretical Shockley–Queisser limit with the process of multiple exciton generation (MEG) or hot carrier collection.[2,38–40]

In the theory of conventional solar cells, each photon can only excite one electron across the bandgap of a semiconductor and excess energy turns into the heat. However, multiple exciton generation (MEG) is a process that allows creation of more than one electron-hole pair under one incident photon. MEG is observed in some semiconductors, like PbTe, PbSe, and PbS QDs and has been investigated intensively with the aim of breaking the Shockley-Queisser limit.[17,39,41] In quantum dot solar cells (QDSC), the excited electron on the conduction band interacts with the hole left behind in the valence band as shown in Figure 2.7-a (process 1). In process 2, the excited electron falls into conduction bands with lower energy relaxing its excess energy. When this excess energy which is equal or higher than the bandgap energy is absorbed by another electron on the valence band, this electron jumps into the conduction band as shown in process 3. Therefore, at least two electron and hole pairs can be obtained under one sun condition.

MEG process occurs when the absorbed photons have energy at least twice of the band gap (E_G) of NP, however for bulk semiconductors higher activation energy is need for the excitation of multiple excitons. As shown in Figure 2.7-b, bulk PbSe has activation energy as almost eight times of E_G, whereas the PbSe QD has less than three times of E_G. The composition and shape of the material have also a significant effect on MEG yield.[42] According to recent studies done on Pb based semiconductors, PbTe QDs have the highest MEG yield whereas PbS QDs have the lowest performance for MEG process.[42] In addition to the composition, shape also affects the MEG yield. As shown in Figure 2.7-b, to reach 120% QE PbSe NRs needs 3 times higher energy then E_G,

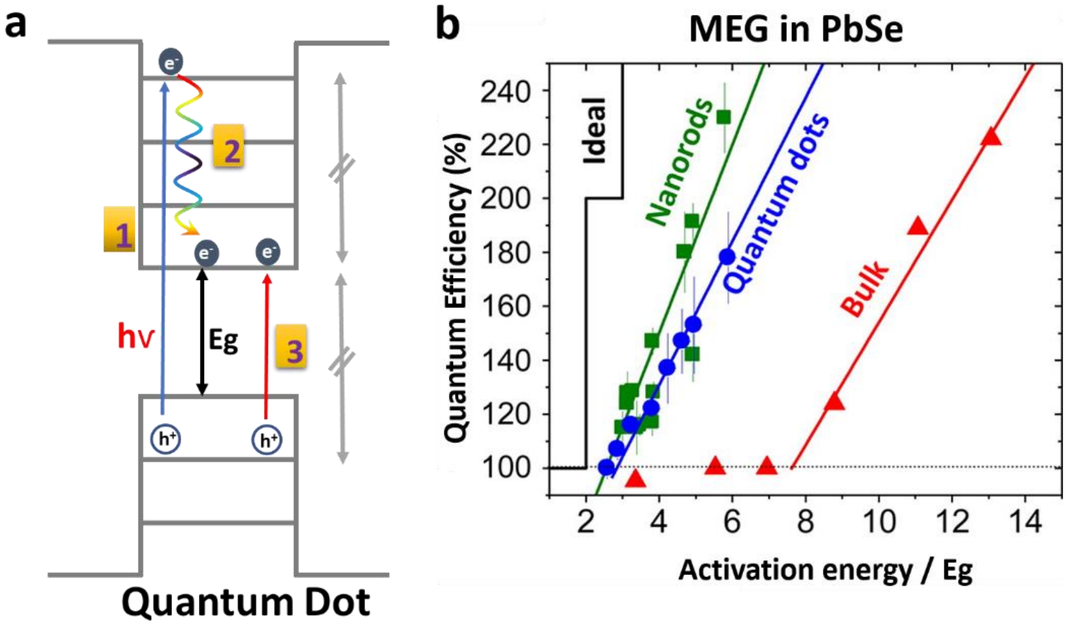

Figure 2.7. **a)** Schematic representation of MEG: 1) absorption of incident photon; excitation of electron leaves behind a hole. 2) relaxation of the electron 3) excitation of another electron to the conduction band from valence band. **b)** Quantum efficiencies versus activation energy to band gap energy (E_G) ratio graph of thin films of PbSe NRs (green), PbSe QDs (blue) and bulk PbSe.[42]

whereas for PbSe QDs this value increases to four times of E_G. Although, spectroscopic studies show quantum efficiency can be greater than 100 % which correspond to MEG process, challenges related to the extraction of the charge carriers limits its utilization in solar energy field.

In the literature, first working solar cell with a MEG process was shown by Semonin et al. for PbSe QDs. [40] Scanning electron microscopy (SEM) images of solar cell and external quantum efficiencies are shown in Figure 2.8-a and d. Solar cells were fabricated by using PbSe QDs with band gaps 0.71 eV (yellow), 0.72 eV (blue), and 0.73 eV (red), ZnO, Au, and MgF_2 were used as electron transport layer, back electrode and anti-reflection coating on the glass (black), respectively. In this study, maximum EQE was measured as 114 % from the PbSe QD with band gap 0.72 eV with anti-reflection coating glass. Later, another study showed the MEG process for a solar cell which contains PbSe NR with different band gap energy; 0.80 eV (green), 0.95 eV (blue), 1.05 eV (red) with ZnO as electron transport layer, MoOx as a hole

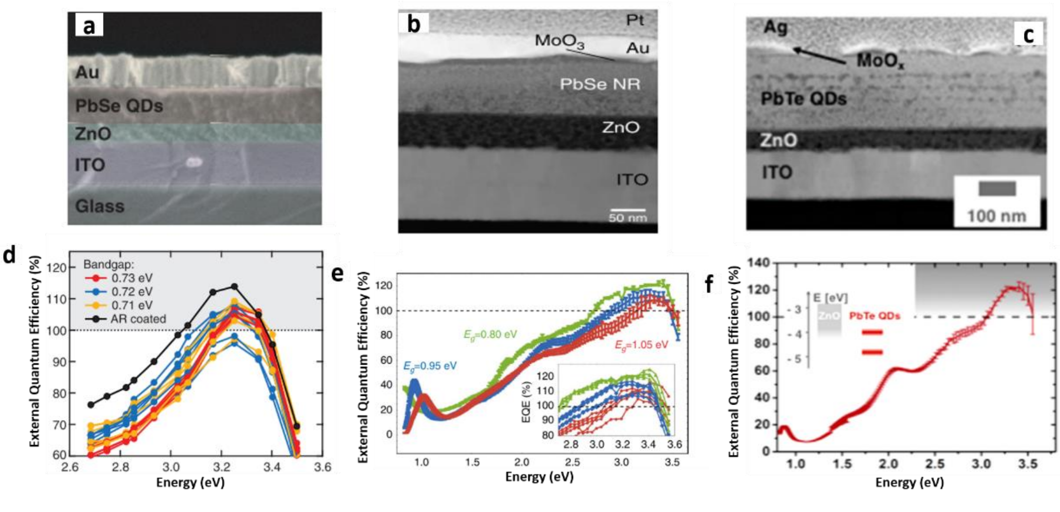

Figure 2.8. Comparison of EQEs for PbSe QDs[40], PbSe NRs[2], PbTe QDs[39] solar cells in the literature. SEM images of solar cells containing **a)** PbSe QDs, **b)** PbSe NRs, **c)** PbTe QDs and EQE of solar cells consisting **d)** PbSe QDs, **e)** PbSe NRs and **f)** PbTe QDs.

transport layer and Pt as a back electrode.[2] The solar cell architecture is shown in SEM images in Figure 2.8-b. Maximum EQE as 122 % was reached from the solar cell contains PbSe NR with band gap of 0.80 eV as shown in EQE in Figure 2.8-e. The third successful MEG yield was the PbTe QDSC with a maximum EQE of 122 %.[39] As represented in SEM images in Figure 2.8-c, they also used ZnO as an electron transport layer for the solar cell of PbTe QDs with the band gap of 0.95 eV.

CHAPTER 3

EXPERIMENTAL

3.1. Materials

All chemicals were of the highest purity available unless otherwise noted and used as received. Lead(II) oxide, (PbO, 99.999%, Aldrich), lead(II) acetate trihydrate ($Pb(CH_3CO_2)_2{\cdot}3H_2O$, 99.9% Aldrich), oleyamine (90%, Aldrich), 1-octadacene (ODE, 90%, Aldrich), oleic acid (OA, 90 %, Aldrich), squalene, 90%, Aldrich), tetradecylphosphonic acid (TDPA, 98%, Alfa Aeasar).

All chemicals listed below were anhydrous and were used as received. Tellurium powder (200 mesh, 99.999 %, Alfa Aesar), selenium powder (200 mesh, 99.999 %, Alfa Aesar), Diphenylphosphine (DPP, 98%, Aldrich), trioctylphosphine (TOP, 90%, Aldrich), tris(diethylamino)phosphine (TDP, 97%, Aldrich), cadmium chloride ($CdCl_2$, 99.9%, Aldrich), benzene1,3-dithiol (BDT, 99%, Aldrich), 1,2-ethanedithiol (EDT, ≥98%, Aldrich), tetrabutylammonium iodide (TBAI, 99% Aldrich), cadmium iodide (CdI_2, 99.999%, Aldrich), rubidium iodide (RbI, 99,9%, Aldrich), lead (II) iodide (PbI_2,99.999%, Alfa Aesar), titanium (IV) isopropoxide (TTIP, 99.999%, Aldrich), tetrachloroethylene (TCE, 99%, Aldrich), N-methylformamide (DMF, 99%, Aldrich), acetone (99.8%, Acros Organics™), methanol (99.8%, Aldrich), buthanol (99.8%, Aldrich), hexane (99%, Aldrich), 2-propanol (99.5%, Aldrich), acetonitrile, (99.8%, Aldrich), octane (≥99%, Aldrich).

3.2. Synthesis

PbSe and PbTe NPs formation reactions were performed using nitrogen-filled Schlenk line techniques and purifications were carried out in nitrogen filled glovebox. PbSe and PbTe NPs were kept in octane for the device fabrication applications or in TCE for the spectroscopic analysis after they purified and dried at least overnight in nitrogen filled glovebox.

3.2.1. Lead Telluride Quantum Dot Synthesis

All PbTe QDs were synthesized according to the modified methods reported by Urban et. al[43] and Murphy et al[44]. In a typical synthesis, 0.89 g PbO (4 mmol), 2.86 ml oleic acid (9 mmol) and 24 ml octadecene (75.8 mmol) are combined in a three-necked flask. The mixture is degassed under vacuum at 90 °C - 100 °C for three hours. The reaction medium is taken under nitrogen flow and the temperature is raised to the injection temperature where 8 ml of 0.5 M TOP-Te with 4 µl DPP (DPP: Pb 1µl/ 1 mmol) solution is rapidly injected while vigorous stirring. TOP-Te stock solution is prepared by dissolving 6.38 g tellurium powder (0.05 mol) in 100 ml TOP and kept in a nitrogen-filled glovebox for further use. The injection temperature is set as 150 °C for 2.50 ± 0.22 nm PbTe QDs. After the injection, the dots are allowed to grow for 120 s while the temperature of the reaction medium is maintained at about 110 °C with the temperature controller unit. The growth process is then rapidly terminated by injecting ice-cold anhydrous hexane (10 ml) and placing the flask in an ice-cold water bath. The crude solution is transferred to the glovebox for the purification. IPA/ACN solvent mixture is added until maintaining a turbid solution and the solution is centrifuged for 5 min at 5000 rpm for further precipitation. After discarding the supernatant, the PbTe QDs are re-dispersed in hexane and precipitated by IPA/ACN or acetone two more times.

All synthetic parameters were optimized to synthesize high-quality PbTe QD. The ratio of OA to Pb was optimized as 2.25 for solar cell application, and the ratio of the volume of DPP to mmol of Pb was optimized as 1 µl/ mmol for small size PbTe QDs.

3.2.2. Lead Selenide Quantum Dot Synthesis

The synthesis of PbSe QDs was carried out following the previous report. [1] In a typical synthesis, 1.31 g $Pb(OAc)_2 \cdot 3H_2O$ (3.44 mmol) and 2.68 ml OA (9 mmol) in 24 ml ODE (75.8 mmol) are combined in a three-necked flask and the mixture is degassed for about 3 h at 100 °C under vacuum. The reaction medium is taken under nitrogen flow and the temperature is raised to the desired injection temperature where 10 ml of 1 M TOP-Se solution containing 104 µl DPP (DPP/Pb = 0.17 molar ratio) is then rapidly injected to the lead oleate solution while vigorous stirring. TOP-Se stock solution is prepared by dissolving 7.89 g selenium powder (1 mol) in 100 ml TOP and kept in a nitrogen-filled glovebox for further use. The PbSe QDs are left for growing for about 100 s. The growth process is then rapidly terminated by injecting 10 ml ice-cold anhydrous hexane and placing the flask in an ice-cold water bath. The crude solution is transferred to the glovebox for the purification. Isopropyl alcohol and acetonitrile are added until maintaining a turbid solution and the solution is centrifuged for five minutes at 5000 rpm for further precipitation. After discarding the supernatant, the PbSe QDs are re-dispersed in hexane and precipitated by acetone two more times.

3.2.3. Lead Selenide Nanorod Synthesis

The synthesis of PbSe NRs was carried out following the modified versions of the previous reports by Koh et al. [45] The bandgap of PbSe NRs was tuned by adjusting the lead to oleic acid ratio (Pb/OA) while the injection temperature and the growth time was adjusted according to the desired bandgap of NRs. For OA/Pb ratio of 3.22, 0.22 g PbO (0.98 mmol) was loaded into a three-neck flask, along with 1 ml oleic acid (3.16 mmol) and 5 ml squalene (9.57 mmol). Once connected to the Schlenk line, the solution was degassed along with heating to 110 °C for 2 hours under vacuum. 3 ml TDP-Se (1 M) precursor solution was then rapidly injected into the lead precursor solution. TDP-Se stock solution is prepared by dissolving 1.57 g selenium powder (0.02 mol) in 20 ml TOP and kept in a nitrogen-filled glovebox for further use. The reaction was terminated in 2 minutes by placing an ice bath under the reaction flask. Purification and size-selective precipitation of the NRs were done using anhydrous hexane/isopropanol solvent system. The precipitated PbSe NRs were isolated by centrifugation at 5000 rpm for 5 min. and dispersed in hexane. These steps were repeated three times.

3.2.4. Titanium Dioxide Nanoparticle Synthesis

Synthesis of TiO_2 NPs was adapted from the literature.[46] The titanium precursor was prepared by mixing solutions of 175 μL TTIP (0.60 mmol) in 1.25 ml ethanol and addition of 17.5 μL hydrochloric acid (2 M, 0.35 mmol) in 1.25 ml ethanol under vigorous stirring. It was prepared as fresh and coated on the substrates just after oxygen plasma.

3.3. Material Characterization

3.3.1. Absorption Spectroscopy

Absorption spectra were recorded by a Shimadzu 3600 plus UV-Vis-NIR spectrometer. NPs were suspended in TCE in the nitrogen filled glovebox using an air tight quartz cuvettes.

3.3.2. Photoluminescence Spectroscopy (PL)

Photoluminescence (PL) measurements were performed by exciting the samples with a 980 nm laser diode. The PL emitted at a right angle relative to the excitation source was directed to a Newport emission monochromator and the PL signal was detected with a thermoelectrically cooled InGaAs photodiode (Hamamatsu-G6126). The spectra were corrected by using the responsivity of the G6126 detector provided by the company NPs were suspended in TCE in the nitrogen filled glovebox using an air tight quartz cuvettes. Optical densities of all the samples were kept same at the excitation wavelength of laser (λ_x = 980 nm) for comparative studies.

3.3.3. Transmission Electron Microscopy (TEM)

Transmission electron microscopy (TEM) samples were prepared by drop-casting a small volume of dilute NP in TCE onto 200 Mesh, carbon coated copper TEM grids and allowing the solvent to evaporate at room temperature. Jem Jeol 2100F 200kV high-resolution transmission electron microscopy (HRTEM) operating at 80-200 kV with Schottky type field emission gun as a source of electron was used for TEM measurements. The CCD camera on which the images were recorded was GATAN, Orius SC10002. At least 140 NPs were examined by using ImageJ analysis program to determine the size distribution and the percentage of branching for PbSe nanorods.[47]

3.3.4. Scanning Electron Microscopy (SEM)

Cross-sectional SEM images of our devices were taken using a Zeiss Auriga CrossBeam workstation and the images were taken at 5 kV voltage and 30 μm aperture size using an in-lens detector. The incident electron beam is accelerated by a voltage of 10 kV. The best resolution of images is 1-5 nm.

3.3.5. Fourier-transform Infrared Spectroscopy (FTIR)

FTIR spectra were acquired in transmission mode using an HYPERRION spectrometer with a resolution of 64. Samples for FTIR measurements were prepared by spin casting of dilute nanoparticle solution (25 mg/ml) in octane. Clean quartz substrates were used for background measurements, and OA-capped or ligand exchanged nanoparticles were spin casted onto the quartz substrates.

3.3.6. X-Ray Photoelectron Spectroscopy (XPS) and Ultra-Violet Photoelectron Spectroscopy (UPS)

XPS and UPS measurements were performed with PHI 5000 VersaProbe in ultrahigh vacuum conditions (10^{-10} mbar). Monochromatic K X-ray source (1486.74 eV) and monochromatic HeI UV source (21.2 eV) were used in XPS and UPS measurements, respectively. The XPS spectra were calibrated using the C1s peak at a binding energy of 284.8 eV. For the UPS studies, samples were biased at -7.00 V for the determination of the low energy cut-off. Ligand exchanged (or oleic acid capped) nanoparticle thin film samples were prepared by spin coating onto Si/Cr (10 nm)/Au (150 nm) substrates. Preparation of the samples were carried out in N_2 filled glove-box and transferred to UPS with an air-tight tube. The samples were exposed to air only during loading to the instrument. Fermi level (reference to vacuum) was determined by the difference between the incident photon energy (21.2 eV) and high binding energy edge. Valance band energy minimum was determined from the low binding energy edge. Conduction band minimum was calculated from the subtraction of valance band minimum from the bandgap (determined from the absorption peak maximum).[2,48]

3.3.7. X-Ray Diffractometry (XRD)

XRD measurements were performed on a high resolution Rigaku Ultima IV X-ray diffractometer with Cu X-Ray source, high resolution graphite monochromator and cross beam optics mechanism. For XRD measurements, samples were prepared by spin casting of 25 mg/ml NP solutions in octane onto a pre-cleaned glass substrate. Average sizes were estimated by counting the number of lattice planes for 10-20 nanoparticles and/or applying the Scherrer equation:

$$t = \frac{K\,\lambda}{b\cos(\theta)}$$

where t is the apparent crystallite size, K ($0.89 \leq K \leq 0.94$, round up to 0.9)is the Scherrer constant , λ is the wavelength of the radiation, b is the additional broadening (in radians), and θ is the Bragg angle.[49] The distances between the adjacent lattice fringes was measured as 3.2 Å which are in agreement with the PbTe (200) d spacing (3.23 Å-JCPDS-ICDD card 38-1435). For PbSe NRs, d spacing 3.0 Å, that is consistent with the PbSe (200) d spacing (JCPDS-ICDD card 06-0354).

3.4. Passivation

3.4.1. Solid State Ligand Exchange Method

The ligand exchange process was performed under inert atmosphere in a nitrogen-filled glovebox. Layers were deposited by a typical layer by layer (LBL) spin coating method using a spin coater. All inorganic and organic ligand solutions were prepared as fresh and filtered through a PTFA syringe filter with a 0.2 µl pore size before use. Each cycle was consisted of three basic steps; introducing of NPs, applying passivation ligand, and removing of excess NPs and ligand from surface. In a typical ligand exchange of OA-capped NPs with ligand, the substrate (Spectrosil, ITO etc.) was covered uniformly with NPs dissolved in octane and spun cast after 5 s at 1500 rpm for 2 s and 2500 rpm for 10 s prior to the ligand treatment and rinsing steps. Then, ligand was introduced to the surface and spun after 5-30 s of wait. Residual ligand and un-exchanged NPs were removed by rinsing two times with the solvent that was used to dissolve the ligand and octane one time, respectively. Exact same procedures were applied for the rest and the cycle was repeated up to the desired thickness. For solid state ligand exchange method, all used ligands and their properties were shown in Table 3.1. The concentration of the solutions and the waiting period before spin casting were changed depending on the type of the ligand.

Table 3.1. Ligand parameters used for solid state ligand exchange method.

Ligand	**Concentration**	**Solvent**	**Waiting Period**
CdI_2 / PbI_2	0.05 M	DMF	30 s
BDT	0.2 v%	ACN	30 s
EDT	0.02 v%	ACN	30 s
TBAI / RbI	0.05 M	MeOH	30 s
Hydrazine	1 M	ACN	-
MPA	10 v %	ACN	-

3.4.2. Growth Phase Ligand Exchange Method

The technique was adopted from published procedures with slight modifications.[1] Cdl_2 or $CdCI_2$ solution was prepared from 465.5 mg Cdl_2 or 232.8 mg $CdCI_2$ (1.27 mmol) and 25.9 mg TDPA (0.093 mmol) in 3.87 ml oleyamine (11.76 mmol) and degassed for 16 h at 100 °C. Desired Cdl_2 solution (Cd: Pb; 1mmol/4mmol) is injected right after the growth of the dots or rods is complete. The temperature of the solution is gradually decreased from 100 to 65 ± 5 °C in a certain passivation period then the reaction is terminated via ice cold hexane injection and placing a water bath under the flask. The passivation period was changed as 2min, 1 min and 10 s.

3.5. Device Fabrication

Schematic representation of solar cell fabrication is shown Figure 3.1. Indium tin oxide (ITO, Psiotec) patterned substrates were cleaned by sonication in warm acetone, isopropyl alcohol, detergent and boiling deionized water for 15 min in sequence, and then dried under a nitrogen stream and left in oven at least for 3 h with a temperature set as 100 °C. After plasma etching of the cleaned substrates for 15 min to remove any organic residue, the electron-transporting TiO_2 layer was coated on ITO substrates. TiO_2 NPs in ethanol was filtered through 0.45 μl pore sized PTFE syringe filter and spun on to ITO substrates at 2500 rpm for 3 s and 5000 rpm for 30 s. These sol-gel TiO_2-covered substrates were annealed in air at 115 °C for 30 min on a hot plate then 450 °C for 30 min in a muffle furnace and left in air for a night. Then the substrates were transferred into a nitrogen-filled glovebox for spin-coating of the active layer. NPs were dissolved in octane (50 mg/ml for QD 25 mg/ml for NR) and were deposited in a L-B-L approach on top of TiO_2 at 1500 rpm for 2 s and 2500 rpm for 10 s. Solid state ligand exchange method was performed as described in Chapter 3.4.1. The devices were loaded into a thermal evaporator in order to evaporate 7 nm MoO_x and 100 nm Au at pressures 10^{-7} mbar through a shadow mask with active area 4.5 mm^2. Finally, the devices were legged for electrical contact and then encapsulated using transparent epoxy/resin and glass slides.

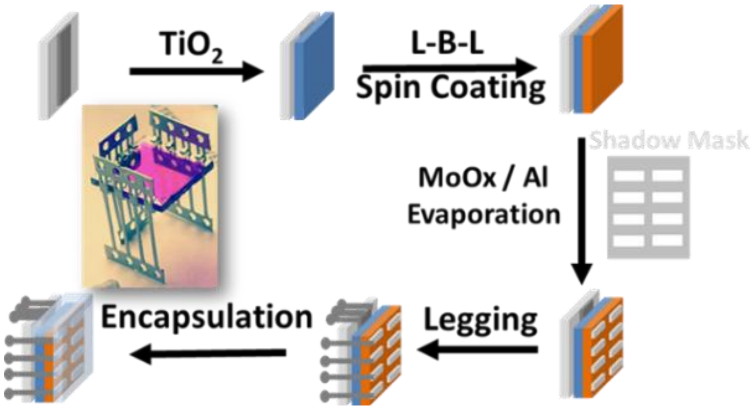

Figure 3.1. Schematic representation of device fabrication process.

Device architecture will be represented in a brief notation as represented in Figure 3.2. Here, ITO and TiO_2 was used as substrate and electron transport layer (ETL) for all the devices, respectively. Each NP composition and type were indicated in the device architecture with subscripted numbers showing the bandgap of the NPs. Different ligands were used for the surface passivation, and abbreviations of each ligand were stated near of the NPs. Thickness optimizations were applied for some of the devices changing the number of spin casted layers, which is also shown between parentheses and each slash shows the separation of the layer type. Also, MoOx and Au were used as a hole transport layer (HTL) and back metal electrode for all the devices.

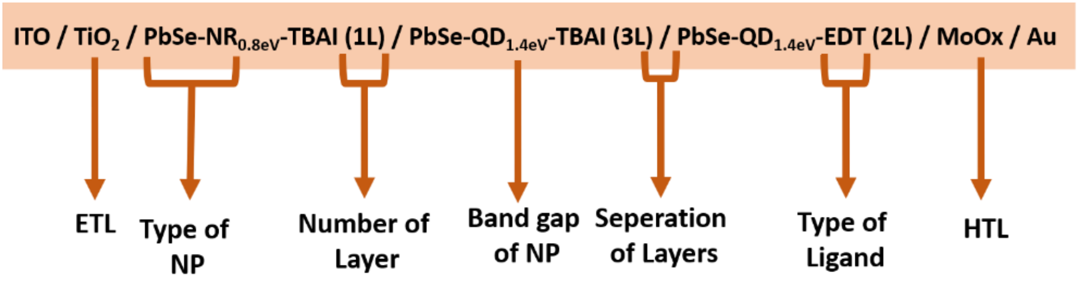

Figure 3.2. Device architecture notation and explanation of the symbols and abbreviations.

3.6. Device Characterization

3.6.1. Current-Voltage Measurement

I-V measurements were taken with a solar simulator inside the N_2 filled glove box at 25 ± 2 °C and a Keithley 2400 source measuring unit. ABET SunLite solar simulator (ASTM Class A stability) with AM1.5 G sun irradiance over 50x50 mm area utilizing 100 W Xe arc lamp (PN: 13013) was used. Results were averaged with standard deviation across 5-8 devices. Standard deviation between the devices is caused by the heating up of the cells under solar simulation during the measurements. The J_{SC}, V_{OC}, FF, and PCE of the devices with maximum efficiencies are quoted in the brackets.

3.6.2. Quantum Efficiency Measurement

External quantum efficiency (EQE), internal quantum efficiency (IQE) and solar cell parameters were measured outside (at 20-28 °C with 85 mm working distance) with a Newport QUANTX-300 apparatus. For EQE and IQE measurements, the current generated by the test solar cell (603415 QUANTX-300) was compared to that generated by the calibrated photodiodes that have a known EQE. An Oriel Monochromator (CS130) was used to filter out a narrow bandwidth of the incident white light source (100 W Xenon lamp) and tune its center wavelength across a desired range. Silicon-germanium detector (PN: 603621) calibrated at NRC (Newport Research Center) within the accuracy specified by NIST (National Institute of Science and Technology) according to the 17025 certification standards was used as calibrated reference detector for 325-1800 nm range. EQE was measured with an uncertainty of ± 25%, ± 7% and ± 3% for the wavelengths in between 300 nm -330 nm, 330 nm -340 nm and 350 nm -1800 nm, respectively. Newport IQE200B (603414 QUANTX-300 Specular Reflectance Standard) was used as Hi-Low calibrated reflectance standard for the IQE measurements. Spectral response was measured with an uncertainty of ± 0.5% of the measured value and compared to that of the test cell before each measurement. Quantum efficiency measurement set-up and measurement process is shown in Figure 3.3.

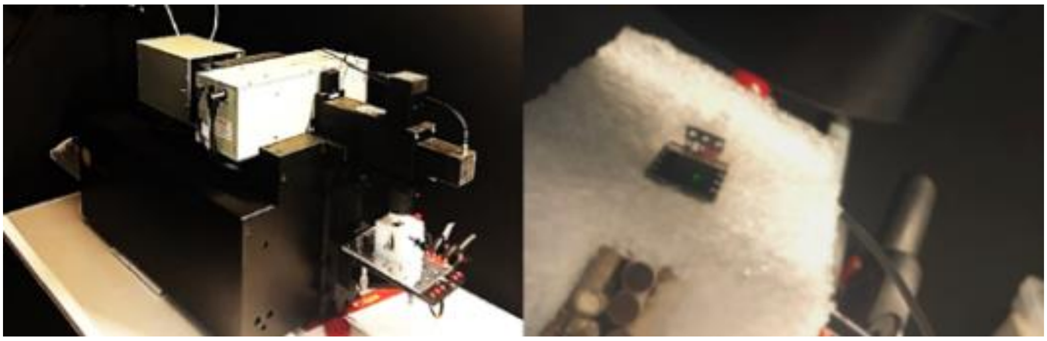

Figure 3.3. Newport QUANTX-300 quantum efficiency measurement set-up (left), measurement process of QDSC (right).

CHAPTER 4

RESULTS & DISSCUSSION

4.1. PbTe Quantum Dots

PbTe QDs with smaller electron and hole masses and larger excitonic Bohr radius (~ 46nm) have been considered as better alternative as compared to the other members of the lead chalcogenides family.[50] One of the greatest barriers for the employment of PbTe QDs in photovoltaics is their high sensitivity towards oxygen and moisture and in parallel their less explored surface chemistry; therefore, all synthetic treatments were performed using Schlenk techniques. For the post-synthetic treatment, oleate-capped PbTe QDs were isolated from starting materials and side products by purifying with anhydrous IPA and then precipitating the QDs with anhydrous ACN in the nitrogen-filled glovebox. Precipitated QDs were then re-dissolved in hexane and isolated using the same solvent system (see Chapter 3.2.1 for the details of the experimental methods).

The synthesis procedure was modified to achieve the ultra-small PbTe QDs with enhanced synthesis yield and stability towards oxygen.[43,44] A series of QDs, having the lowest energy excitonic transition tuned from 898 to 1504 nm and with sizes from 1.7 ± 0.2 nm to 5.0 ± 0.5 nm, was synthesized to assess the effect of size on stability. Absorption spectra and high-resolution TEM images of these QDs were shown in Figure 4.1.

4.1.1. Surface Stability and Passivation

Development of strategies aiming to control the surface states and improve the material quality through surface passivation is an ongoing challenge for attaining QD based photovoltaic cells with outstanding efficiencies.[8] PbTe QDs, when stored in the solid form, decompose due to the adsorption of moisture and oxygen.[51] As shown in

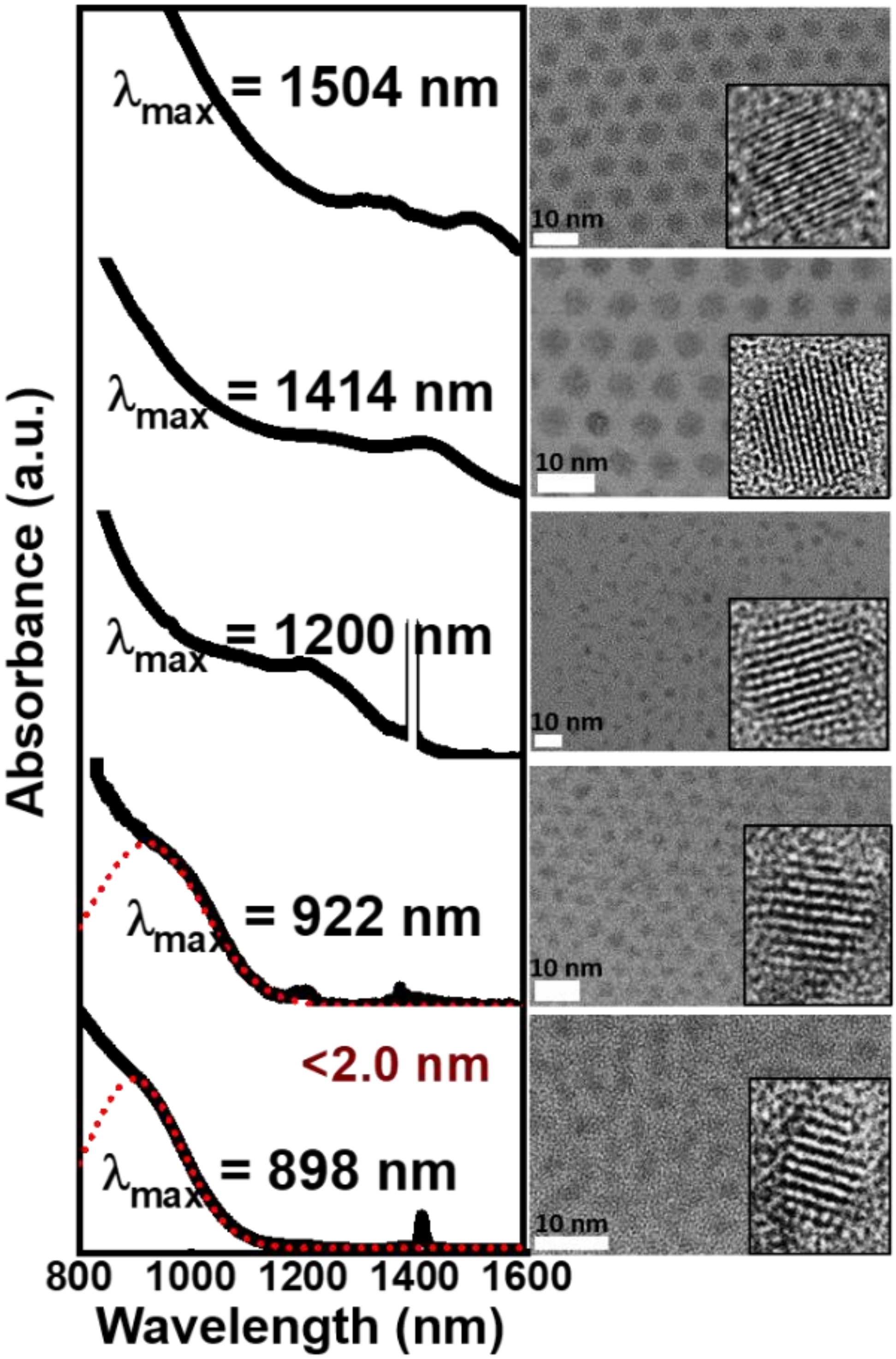

Figure 4.1. Absorption spectra and HRTEM images of the QDs with diameters changing between 1.7 ± 0.2 nm to 5.0 ± 0.5 nm. The peak around 1450 nm is belong to the liquid water.[52]

Figure 4.2, PbTe QDs showed a strong size and shape dependent air stability. Larger PbTe QDs were more susceptible to oxidation as compared to the smaller QDs as shown in Figure 4.2 by yellow dots. PbTe QDs having size <2 nm had a well resolved octahedron shape which transferred to truncated octahedron in between 3.6 nm and 3.9 nm and finally to cuboctahedron at 5.0 nm. The ambient stability abruptly changed other members of the lead chalcogenide family (PbS and PbSe QDs).[53]

In order to enhance the endurance of PbTe QDs towards oxidation, growth phase surface passivation method (SynP) which is previously explored for PbS and PbSe QDs were adopted with some modifications.[1,54] $CdCI_2$ passivation were performed with growth phase ligand exchange method were applied to the PbTe QDs as mentioned in Chapter 3.4. After 60 s of passivation time, SynP-PbTe QDs were

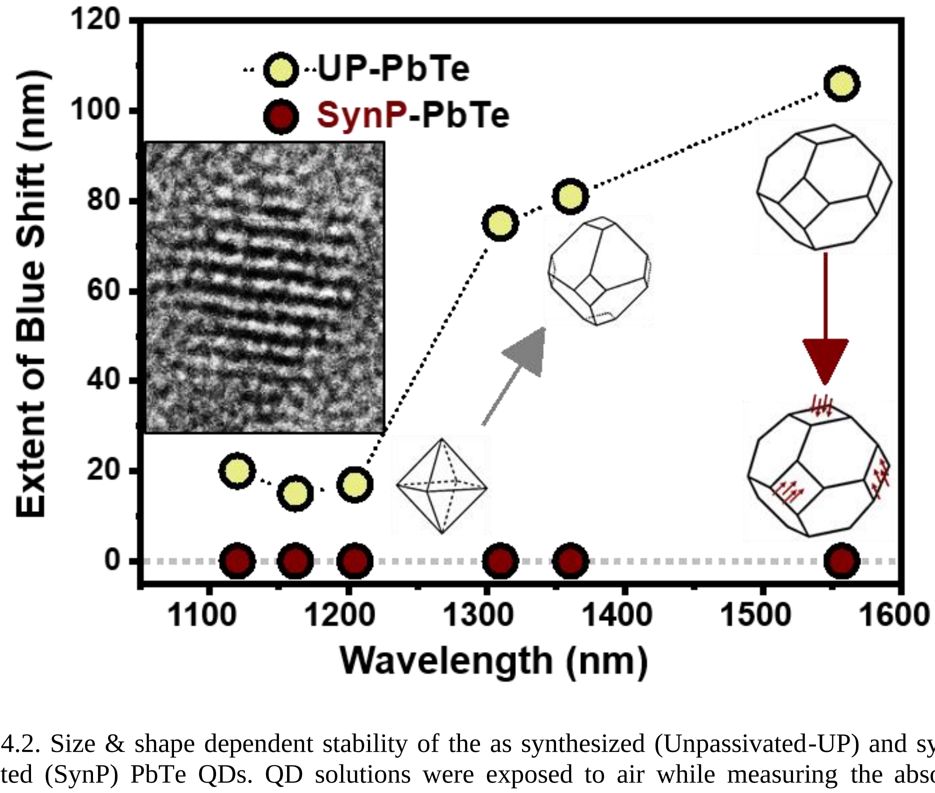

Figure 4.2. Size & shape dependent stability of the as synthesized (Unpassivated-UP) and synthesis passivated (SynP) PbTe QDs. QD solutions were exposed to air while measuring the absorbance spectrum in two minutes time interval for an hour. Inset: HRTEM image of a highly crystalline PbTe QD with an octahedral shape.

isolated with an optimized Pb/Cd mole ratio of 4:1. PbTe QDs passivated with the SynP method preserved their absorption peak when stored under ambient conditions in TCE as shown in Figure 4.2 (shown by red dots). Absence of the blue shift under ambient conditions for a wide variety of sizes shows the effectiveness of the SynP method applied in this study.

To investigate the effects of SynP passivation approach on the crystallographic structure of the QD, X-ray diffraction (XRD) measurements on thin films spin coated on glass substrates were utilized. Thin film XRD patterns of the oleate capped UP and SynP PbTe QDs showed a well-defined fcc structure with the Fm3m space group (a = 6.459 Å; JCPDS-ICDD card 38-1435) as represented in Figure 4.3. The relative intensities were reported by averaging with a standard deviation across 2-3 samples from different batches for each treatment. Average sizes were estimated by counting the number of lattice planes for 10-20 quantum dots from the TEM images of dots and applying the Scherrer equation to the line broadening of the main XRD (200) peak (see Chapter 3.3.7). The distances between the adjacent lattice fringes were measured as 3.2 ± 0.1 Å which were in agreement with the PbTe (200) d spacing as 3.23 Å at the JCPDS-ICDD card number of 38-1435.

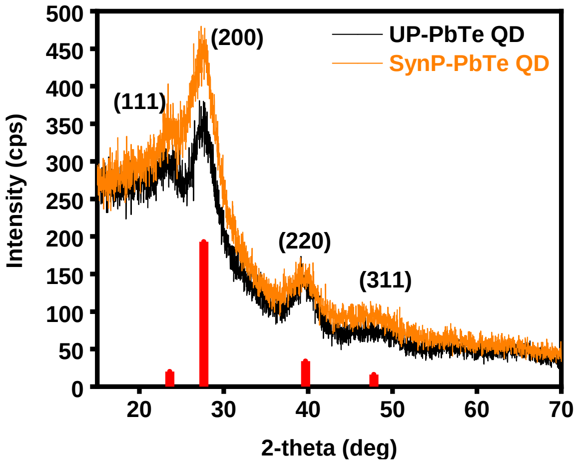

Figure 4.3. Thin film XRD patterns of UP (black), SynP (orange) PbTe QDs spin coated on glass and values from JCPDS-ICDD card number of 38-1435 (red).

To examine the chemical environment of the surface atoms XPS measurement were utilized for the PbTe thin film samples prepared by spin coating on Si/Cr (10 nm)/Au (150 nm) substrates. Pb/Te ratio markedly increased from 1.5 to 2.4 with the SynP procedure as shown in APP-1 and APP-2. From the combination of the XPS and XRD measurements, it is reasonable to conclude that the SynP QDs have more Pb-terminated {111} facets compared to the UP QDs.[55] Figure 4.4 shows the high resolution XPS spectra of Pb-4f, Te-3d and Cl-2p for the UP and SynP oleate capped PbTe QDs. The Te-3d peak at 572.0 eV corresponds to the binding energy of Pb–Te while the peaks at 198.0 eV and 199.6 eV correspond to the binding energy of Pb-Cl[56]. A well resolved shoulder in the Pb 4f signal for the SynP QDs (4f7/2 and 4f5/2 core electronic states) is a sign of perturbations from the local chemical bonding. The 4f7/2 peak fitted with two components centered at 137.5 eV and 138.5 eV corresponds to the binding energy of Pb–Te and Pb–Cl bonds, respectively.[56,57]

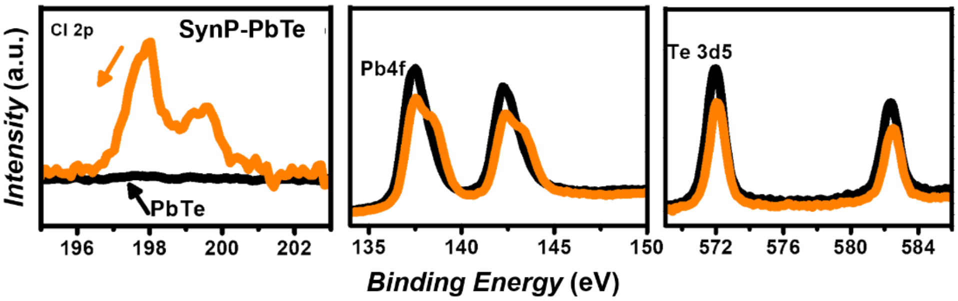

Figure 4.4. High resolution XPS spectra of Pb-4f, Te-3d and Cl-2p for the as synthesized (UP) (black) and growth phase passivated (SynP) oleate capped PbTe QDs (orange).

To get more insight the instability of the PbTe QDs, thin films prepared from oleate capped as synthesized oleate capped QDs (UP) were compared with growth state passivated SynP-PbTe QDs. Extremely unstable large size PbTe QDs were used for thin film preparation to assess the effectiveness of the developed method. Also, the combinatorial passivation method based on engineering the quantum dot surface during the growth phase and solid-state ligand exchange process on the thin films were investigated. As a solid-state ligand exchange ligand, TBAI, known to be an effective surface stabilizer for the other lead chalcogenides, surprisingly did not improve the stability of the PbTe QDs. The absorption signal disappeared in less than 20 minutes after exposing the thin films to the atmospheric conditions as shown in Figure 4.6-a for UP-TBAI PbTe QDs. Figure 4.5-a shows that BDT ligand exchanged PbTe QD thin films (UP-BDT) were also unstable under ambient conditions, in agreement with the previous reports for the BDT exchanged PbS and PbSe QDs.[1] On the other hand,

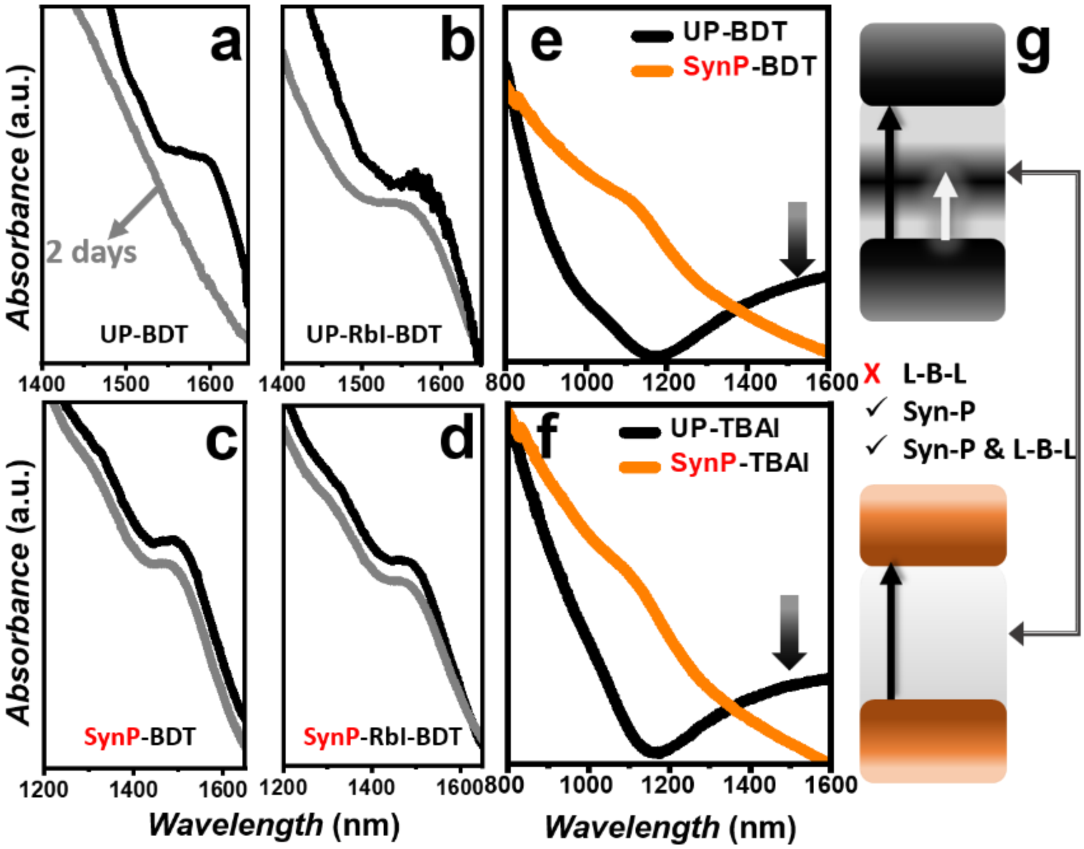

Figure 4.5. Improving the ambient stability and removal of the mid gap states (MGS) via passivation during growth phase (SynP) and passivation during LBL process for small and large PbTe QDs. Absorption spectra of **a)** BDT and **b)** RbI-BDT ligand exchanged thin films prepared from as-synthesized (UP) QDs. Absorption spectra of **c)** BDT and **d)** RbI-BDT ligand exchanged thin films prepared from SynP QDs. Absorption spectra of the **e)** BDT and **f)** TBAI ligand exchanged thin films prepared from UP and SynP QDs. **g)** MGS originate mainly from the LBL process and can only be controlled by using SynP QDs.

treatment of the UP-PbTe QD surface with RbI (UP-RbI-BDT) or CdI_2 (UP-CdI_2-BDT) prior to the BDT treatment improved the stability with a moderate (36 nm) blue shift upon oxidation as shown in Figure 4.5-b (see Figure 4.6-b for UP-CdI_2-BDT). The presence of the blue shift in the UP-RbI-BDT and UP-CdI_2-BDT thin films shows that all of the sites are prone to oxidation, and they are not accessible during LBL treatment however additional sites should be introduced during the ligand exchange process.

Above mentioned sources of the instability were overcome by using the SynP-QDs instead of the UP-PbTe QDs for the thin film preparation process. In this way, the SynP-BDT thin films had better air stability when compared to the UP-BDT thin films as shown in Figure 4.5-a and Figure 4.5-c. Moreover, dually passivated SynP-RbI-BDT and SynP-CdI_2-BDT thin films showed remarkable air stability by preserving their absorbance peak with an indistinguishable blue shift (0-2nm) under ambient conditions as shown in Figure 4.5-d (see Figure 4.6-c for SynP-CdI_2-BDT). Therefore, surface defects formed mainly during the LBL process can only be avoided by passivating the PbTe QDs with the SynP procedure, which stabilizes the QD surface by increasing their capacity to withstand the harsh conditions of the ligand exchange process.

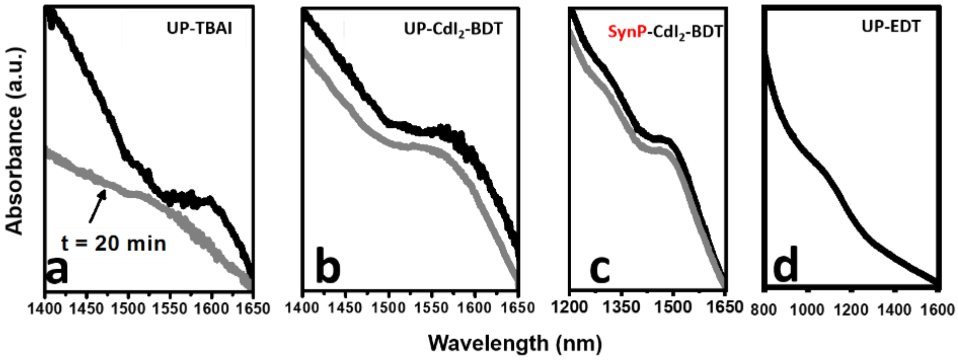

Figure 4.6. Investigation of the ambient stability of PbTe QD thin films. Absorption spectra of the **a)** TBAI ligand exchanged and **b)** CdI_2-BDT ligand exchanged thin films prepared from as-synthesized (UP) PbTe QDs. **c)** absorption spectra of CdI_2-BDT ligand exchanged thin films prepared from growth phase passivated (SynP) PbTe QDs. **d)** Absorption spectra of the EDT ligand exchanged thin film prepared from UP PbTe QDs.

The effects of the combinatorial passivation method based on engineering the quantum dot surface during the growth phase and solid-state ligand exchange process on the thin films were investigated by preparing films from small size PbTe QDs. Figure 4.5-e compares the absorption spectra of the UP-BDT and SynP-BDT thin films. The most striking observation in Figure 4.5-e is the pronounced feature on the low energy side for the UP-BDT thin films which may be ascribed to the presence of mid gap states (MGSs).[58] Notably, the MGS absorption disappeared when the UP QDs were ligand exchanged with EDT instead of BDT. As shown in Figure 4.6-d, elimination of the low energy side absorption feature in UP-EDT points out to the fact that the formation mechanism of the MGSs depends strongly on the type, structure, size etc. of the ligand used. To reveal the effect of halide passivation on the formation of MGSs during the LBL process, UP and SynP QDs were ligand exchanged with a halide source, TBAI, instead of BDT. Disappearance of the low energy absorption feature in the SynP-TBAI thin films, in contrast to the UP-TBAI thin films with a pronounced MGS absorption, points out to the fact that the utilization of the solid-state halide passivation alone is not sufficient for the inhibition of the MGS formation. It is worth noting that the fabrication of defect free thin films irrespective of the ligand type can only be achieved by using the SynP QDs for the thin film fabrication process.

XRD measurements were utilized to examine the effects of the combinatorial passivation approach on the crystallographic structure of the QD. Figure 4.7-a,b displays the change of the main XRD peaks of the BDT, RbI-BDT and CdI_2-BDT ligand exchanged thin films prepared from the UP and SynP PbTe QDs. An increase of the {111} / {200} plane ratio from 0.19 ± 0.13 for the UP QDs to 0.52 ± 0.16 for the SynP QDs were observed. Differences in TEM images and the {111} / {200} plane ratio for the QDs similar in size showed that the in-situ metal halide passivation method had a control over the shape. Shape, being an important parameter for the packing preferences of the QDs[53], affected the degree of long range order as demonstrated in the TEM images as represented in Figure 4.7-c and d. The thin films prepared from the oleate capped SynP QDs were preferentially oriented with a long-range order and had higher crystallinity compared to the thin films prepared from oleate capped UP-QDs. XRD patterns of the ligand exchanged thin films were investigated to assess the packing preferences during LBL processing. Thin films prepared from the SynP QDs preserved the {111} / {200} plane ratio by packing along <111> direction during the LBL ligand exchange process, irrespective of the ligand type (BDT, RbI-BDT or CdI_2-BDT), whereas the same size UP QDs lost the {111} plane by packing along <200> direction during the LBL ligand exchange process as shown in Figure 4.7-a,b. As a result, the bound halides on the QD surface not only improve the shelf life of the QDs but also dictate the packing preference during the LBL ligand exchange process.

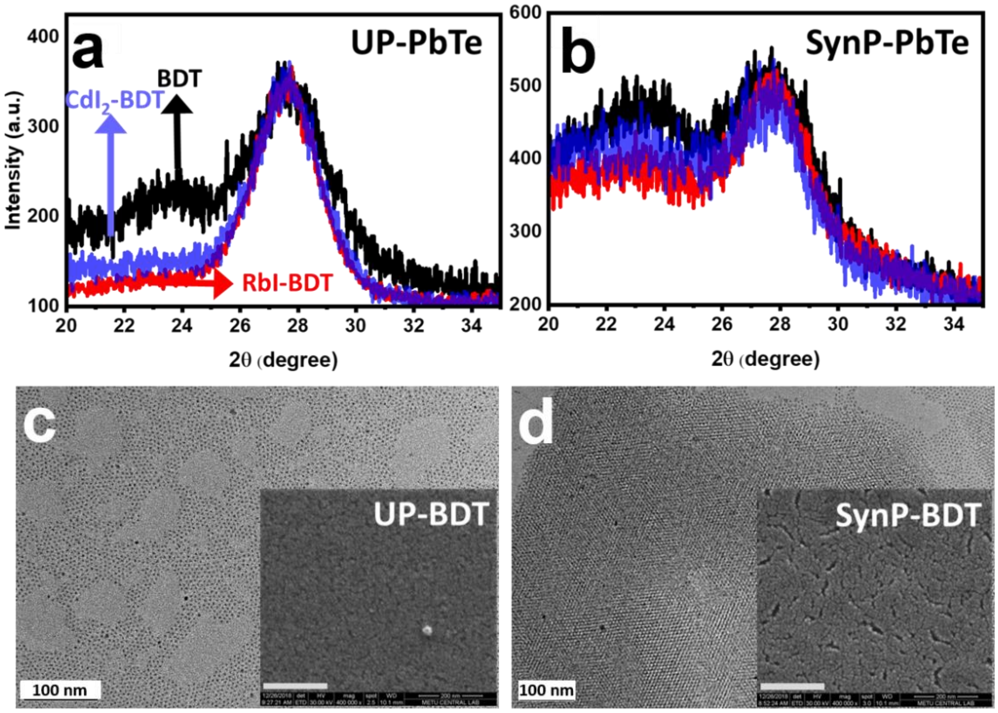

Figure 4.7. Thin film XRD patterns of the BDT, RbI-BDT and CdI_2 -BDT ligand exchanged thin films prepared from **a)** UP-QDs and **b)** SynP PbTe QDs. Introducing metal halides to the UP-QD surface prior to the BDT treatment promotes the packing along the direction as indicated by the disappearance of the (111) diffraction for the UP-RbI-BDT and UP-CdI_2 -BDT thin films. TEM images of the **c)** UP and **d)** SynP, OA capped PbTe QDs. Inset: SEM images of the BDT ligand exchanged thin films on ITO.

Table 4.1 shows the atomic percentages of the elements in the ligand exchanged thin films. Carbon content of the BDT ligand exchanged thin films increased significantly from 0.04% to 0.06% when the SynP-QDs were used for the thin film preparation process. Higher carbon atomic percentage in the SynP-BDT ligand exchanged thin films was attributed to the higher ligand exchange rate of the SynP-QDs. Improved ligand exchange rate for the SynP-QDs was also supported by the scanning electron microscopy (SEM) measurements. Figure 4.7-c and Figure 4.7-d (inset) show the SEM images of the UP- BDT and SynP-BDT thin films prepared from the PbTe QDs that were similar in supported by the scanning electron size. A higher ratio of cracks observed in the SynP-BDT thin films was mainly assigned to the presence of polar and highly reactive {111} surfaces leading to a more volume contraction during the ligand exchange process.[55]

Table 4.1. Atomic percentage of the elements in ligand exchanged thin films that are normalized to Pb and determined by XPS.[a]

Thin Film	Pb	Te	I	C	Pb/(Te+I)
UP-BDT	1	0.76	-	0.04	1.31
UP-RbI-BDT	1	0.62	0.69	0.08	0.76
UP-CdI_2-BDT	1	0.68	0.51	0.06	0.84
SynP-BDT	1	0.68	-	0.06	1.47
SynP-RbI-BDT	1	0.51	0.49	0.14	1.00

[a] Atomic percentages of the metal cations Cd and Rb are well below the resolution of the XPS spectrometer utilized in this study. Lack of Cl in SynP-BDT and SynP-RbI thin films shows that Cl is washed out during the ligand exchange process.

In light of these observations, significant recovery of the blue shift in air exposed SynP thin films points out to the essential role of the facet specific ligand exchange rate mechanism.[59,60] In this sense, higher stability of the thin films prepared from the SynP-QDs can be assigned to the effective passivation the facets of kinds on the QD surface during the ligand exchange process. Distinct differences in the morphology signify that the shape of the QD may also affect the accessibility of the passivating ligands to the QD surface.[53] In this respect, QD shape is another parameter to be considered for a successful ligand exchange process with a high ligand exchange rate.[59,60] A remarkable thin film stability for a wide range of sizes and shapes can be achieved by an optimized surface passivation strategy that controls the {111}/ {200} plane ratio during the ligand exchange processes.

4.1.2. Solar Cell Application

Solar cells from 8 layers of UP (E_G = 1.08 eV) and SynP (E_G= 0.97 eV) PbTe QDs treated with BDT, RbI-BDT and CdI_2-BDT were fabricated to get more insight into the effects of the passivation techniques on the photovoltaic performance. The device architecture, valence and conduction band edges and the solar cell characteristics are represented in Figure 4.8. TiO_2 used as electron transport layer, whereas the Au was used as the back-contact material for the devices. Figure 4.9 shows the UPS spectra of corresponding thin films.

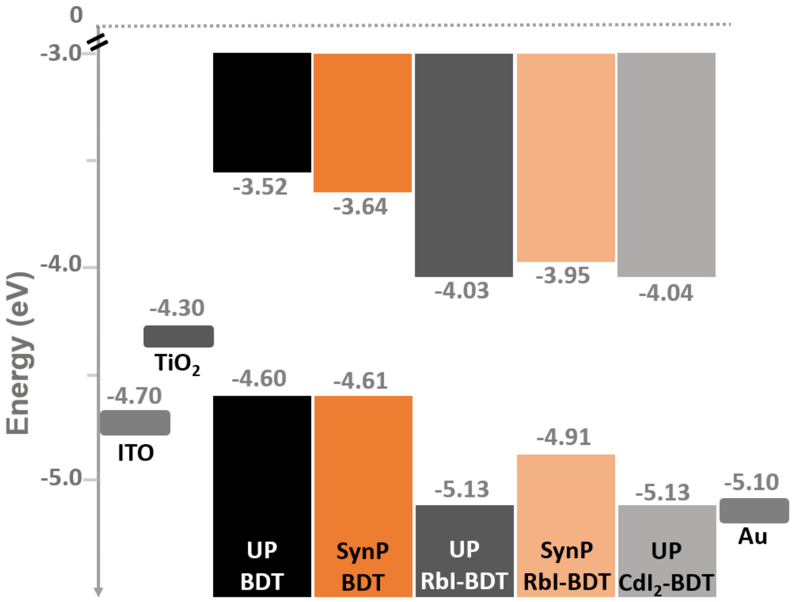

Figure 4.8. Band edge energies of PbTe QDs with respect to vacuum were determined by UPS spectroscopy.

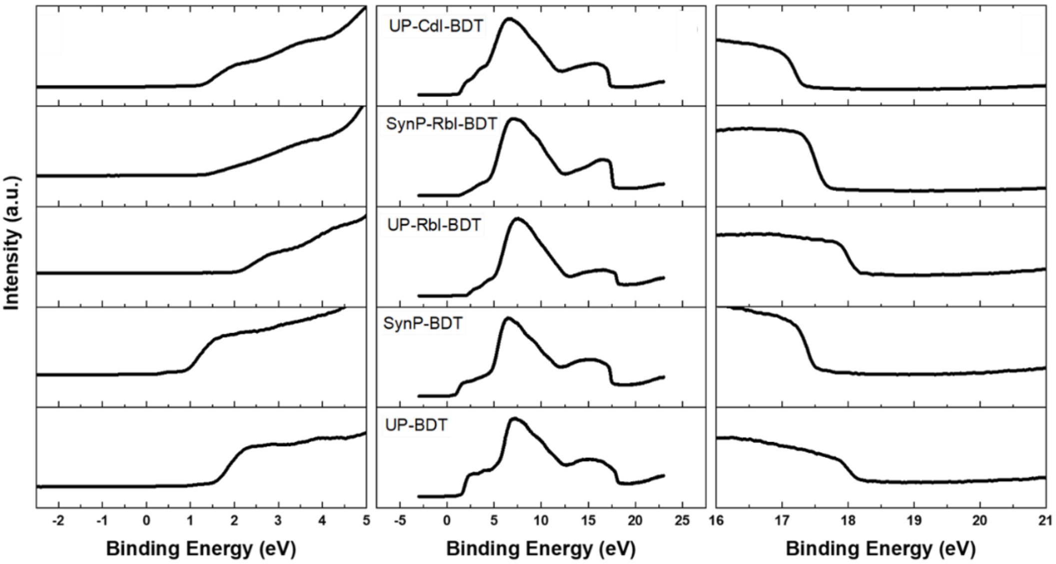

Figure 4.9. UPS spectra of thin films represented in Figure 4.8.

Table 4.2 shows the device performance of the corresponding solar cells. Open circuit voltage (V_{OC}) increased from 0.27 ± 0.01 V to 0.31 ± 0.01 V when the SynP PbTe QDs were used in the preparation of the BDT ligand exchanged active layer. Increase in the V_{OC} (>14%) despite the lower band gap of the SynP QDs can be attributed to the effective removal of the defect states in the SynP QDs.

Table 4.2. Device Parameters for PbTe QD Solar Cells (ITO/TiO_2/PbTe QDs/MoOx/Au) under AM 1.5 spectral illumination (1000 W/m^2). [a]

Device	**V_{OC} (V)**	**J_{SC} (mA/cm^2)**	**FF**	**PCE (%)**
UP-BDT	0.27 ± 0.01 (0.28)	2.8 ± 0.1 (3.1)	0.35 ± 0.01 (0.33)	0.27 ± 0.02 (0.28)
SynP-BDT	0.31 ± 0.01 (0.32)	2.1 ± 0.2 (2.3)	0.30 ± 0.02 (0.33)	0.20 ± 0.04 (0.24)
UP-RbI-BDT	0.12 ± 0.01 (0.12)	8.7 ± 1.1 (9.7)	0.27 ± 0.01 (0.27)	0.29 ± 0.02 (0.31)
SynP-RbI-BDT	0.14 ± 0.01 (0.15)	12.1 ± 0.5 (12.5)	0.27 ± 0.01 (0.27)	0.45 ± 0.04 (0.50)
UP-CdI_2-BDT	0.12 ± 0.01 (0.12)	14.7 ± 3.4 (17.2)	0.28 ± 0.01 (0.26)	0.48 ± 0.11 (0.69)

[a] Results were averaged with standard deviation across 5-8 devices. The J_{SC}, V_{OC}, FF, and PCE of the devices with maximum efficiencies are quoted in the brackets.

It is worth to mention that the metal halide passivation with RbI (or CdI_2) prior to the BDT treatment dramatically affects the cell parameters. In this sense, RbI treatment led to a decrease in the V_{OC} from 0.27 ± 0.01 to 0.12 ± 0.01 V for the UP QDs. Lower Voc with the RbI-BDT treatment was attributed to the shift of the valence and conduction band edges to the lower energy side as represented in Figure 4.8, in contrast to the study reported by Ko et al.[61,62] Short circuit current (J_{SC}) increased markedly from 2.8 ± 0.1 mA/cm^2 to 8.7 ± 1.1 mA/cm^2 when the RbI is introduced prior to the BDT which was mainly ascribed to the lower band offset of the RbI-BDT treated active layer with the electron accepting TiO_2 layer. As a whole, PCE was not affected much when the UP QDs were ligand exchanged with RbI-BDT as the loss in Voc was compensated with the gain in J_{SC}. Noticeably higher PCE for the UP-CdI_2-BDT solar cells was mainly due to a significant rise in J_{SC} (14.7 ± 3.4 mA/cm^2). Notably, RbI-BDT treatment led to a dramatic rise in the PCE of the SynP-PbTe QDs in contrast to the UP PbTe QDs where the PCE was not affected. J_{SC} values were measured as 2.1 ± 0.2 mA/cm^2 and 12.1 ± 0.5 mA/cm^2 for the SynP- BDT and SynP-RbI-BDT solar cells, respectively. As a whole, RbI treatment, when utilized with the SynP PbTe QDs, improved the PCE from 0.20 ± 0.04% to 0.45 ± 0.04%.

Noticeably higher increase in the J_{SC} for the solar cells where the SynP-PbTe QDs were used as an active layer was assigned to the increase in the charge collection efficiency due to the smaller number of trap states acting as electron−hole recombination centers. Furthermore, the solar cells prepared from the SynP-QDs and treated with RbI-BDT showed a robust stability. Figure 4.10-b compares the EQE responses of the six months old devices prepared from the UP and SynP-PbTe QDs treated with RbI-BDT. The J_{SC} value of the SynP-RbI-BDT solar cell, calculated by integrating the EQE spectra with the AM 1.5 G solar spectrum, was 14.5 mA/cm^2 which showed a good agreement with the initial J_{SC} (12.1 ± 0.5 mA/cm^2). In this respect, avoiding trap state formation during solid state ligand exchange process by using SynP PbTe QDs is a key strategy to maximize the PCE and stability. The trends in the PCE with various metal halide treatments might also be attributed to the charge balances (sum of the positive formal charges/sum of the negative formal charges = (Pb + Cd + Rb)/(Te + Cl + I) calculated from the XPS compositional analysis (see Table 4.1). Previous studies showed the effect of stoichiometry on the mid gap states and concluded that the off stoichiometry introduces mid gap states in the gap and leads to poor performing solar cells. [63,64] Charge balance for the UP-BDT thin film was calculated as 1.31, which decreased to 0.76 for the UP-RbI-BDT thin film. The drop in the charge balance might be ascribed to the insertion of halides with the RbI treatment. The PCE, on the other hand, was not affected much as the extent of deviation from unity were similar for the UP-BDT (1.31) and UP-RbI-BDT (0.76) thin films. The charge balance for the UP-CdI_2-BDT was calculated as 0.84. Improved stoichiometry for the UP-CdI_2-BDT thin film compared to the UP-RbI-BDT (0.76) was ascribed to the introduction of a smaller number of halides with the CdI_2 reagent. As a result, the best PCE for the UP QDs was obtained with the CdI_2 treatment. On the other hand, SynP-BDT thin film yielded slightly more off stoichiometric QDs (1.47) as compared to UP-BDT (1.31) which was attributed to the alteration of the

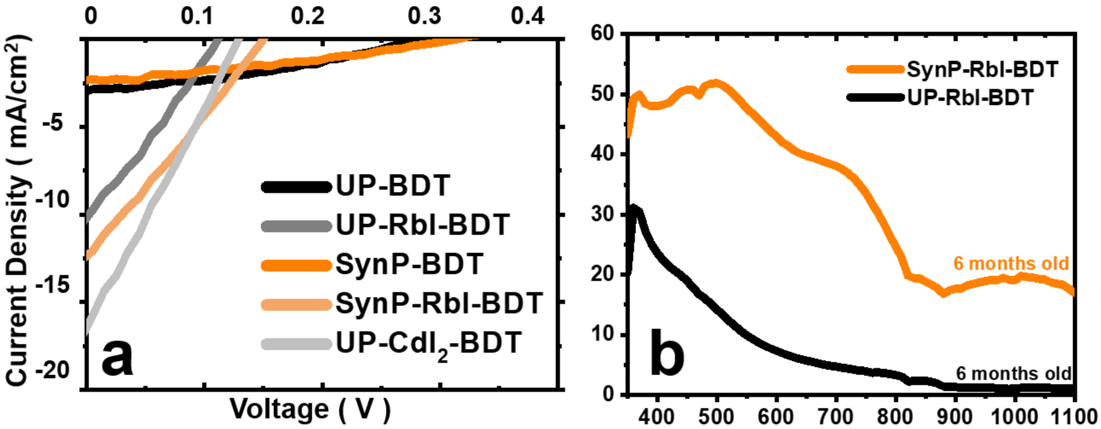

Figure 4.10. **a)** Current density-voltage behavior of the solar cells prepared from the UP and SynP PbTe QDs that were ligand exchanged with BDT, RbI-BDT and CdI_2-BDT. The solar cells exhibit ITO/TiO_2/PbTe-QDs/MoOx/Au device architecture (refer to the Table 4.2 for the results averaged with standard deviation across 5-8 devices). **b)** External quantum efficiency spectrum of the six months old solar cells prepared from the SynP and UP PbTe QDs treated with RbI-BDT.

Pb/Te ratio with the SynP procedure. As represented in Table 4.1, RbI-BDT treatment shifted the charge balance of the SynP-BDT thin films from 1.47 to unity and yielded stoichiometric PbTe QDs with the highest PCE.

As a result of all optimization studies, the champion device was fabricated using SynP-PbTe QDs with the treatment of BDT resulting 11.74 ± 0.63 mA/cm^2 of J_{SC} and 0.44 ± 0.01 V of V_{OC} which is the highest V_{OC} in the literature as shown in J-V characteristics in Figure 4.11-a. Also, EQE spectrum (shown in Figure 4.11-b) with the AM 1.5 G solar spectrum showed maximum peak intensity around 65%.

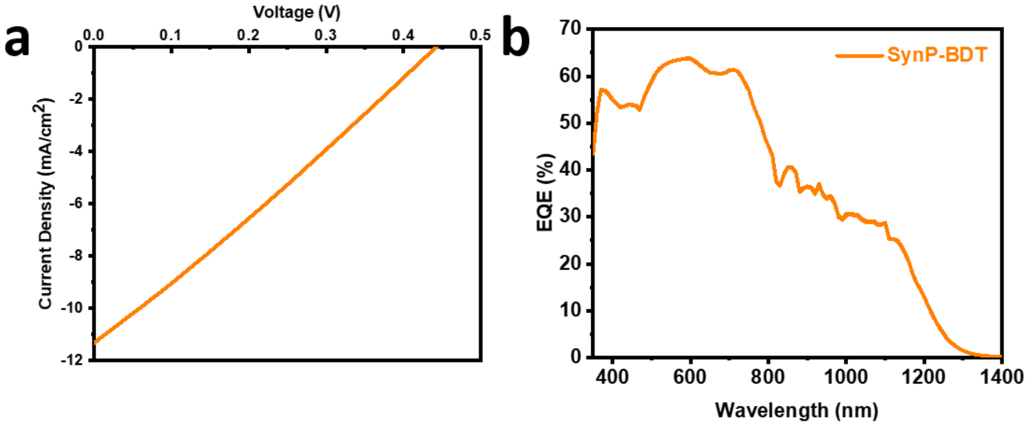

Figure 4.11. **a)** Current density-voltage behavior and **b)** External quantum efficiency spectrum of the solar cells prepared from SynP PbTe QDs that were ligand exchanged with BDT. The solar cells exhibit ITO/TiO_2/PbTe-QDs/MoO_x/Au device architecture.

4.2. PbSe Nanorods

Colloidal quantum dots have been of particular interest for inexpensive solar cells due to their high MEG yields.[65] According to the recent reports, 2-D nanostructures are better alternative for MEG compared to dots.[66] Strategies aiming to increase the NR yield and improve the material quality is an ongoing challenge for the high-performance NC photovoltaic cells. Through the systematical manipulation of synthesis parameters, the effects of each reaction parameter on the optical and morphological properties of PbSe NRs were managed during this study. Sensitivity of PbSe NRs towards oxygen was studied on resulting more stable rods for the solar cell application. Successful fabrication of PbSe NRs solar cells were performed collaborating with PbSe QDs to create better films and enhance photo current efficiency.

4.2.1. Optimization of Synthetic Parameters

The effect of different temperature profile, OA/Pb ratio and catalyst on the optical and morphological properties of PbSe NRs were investigated.

Controlling the temperature during NR growth affects the optical and morphological properties of the NRs in parallel to the literature reports.[2] In the light of this, the effect of temperature profile during growth under three different conditions were investigated as shown in Figure 4.12. Reactions during which the heating source was kept intact but switched off, were allowed to cool down gradually (from 170 °C to 140 °C) during growth. On the other hand, temperature dropped suddenly when the heating source was removed right after the injection and a sharp decrease (from 170 °C to 110 °C) in temperature during growth affected the optical properties of NRs. Figure 4.12-b represents the change in absorbance peak points of NRs synthesized under different temperature profiles and with different OA/Pb ratios. NRs synthesized with a sudden drop in growth temperature had an absorption peak at 1370 nm whereas the NRs synthesized with a gradual drop in growth temperature had an absorption peak at 1569 nm. Larger size of NRs with gradual drop temperature profile can be attributed to the increasing rate of formation of monomers at higher temperature according to the established nucleation theory. Different trends were observed when the effect of OA/Pb ratio on the absorption peak under sudden and gradual temperature drop profiles are compared. As the OA/Pb ratio increases, the bandgap (E_G (eV) = 1240/λ (nm)) of the NRs decreases for the gradual temperature drop and increases for the sudden of the NRs decreases for the gradual temperature drop and increases for the sudden temperature drop. According to the represented data, it is observed that temperature profile plays a significant role in optical properties of the NRs. Due to lower repeatability of the experiments done with gradual drop and sudden drop temperature profiles, the heating source was switched to an oil bath with a preset temperature right after the injection. NRs synthesized with a steady temperature profile (from 170 °C to 150 °C) throughout growth shows a similar trend with gradual drop profile as expected.

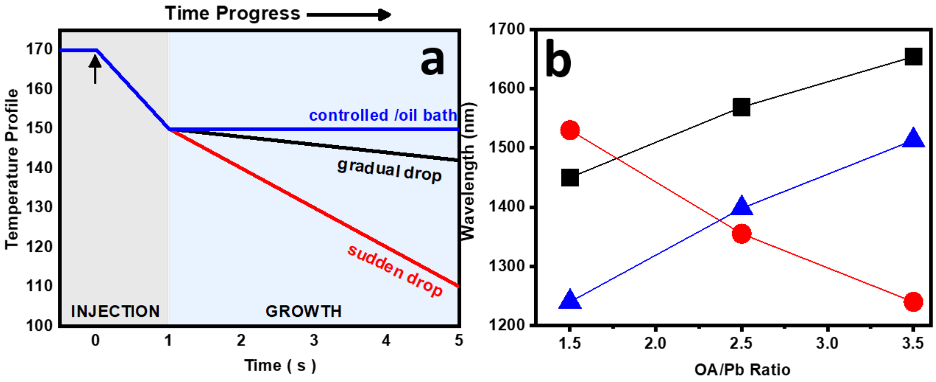

Figure 4.12. Effect of different growth temperature profiles on the optical properties of PbSe NRs. **a)** Gradual temperature drop (black solid line) provided by keeping the heating source under reaction balloon, sudden temperature drop (red solid line) by removing the heating source after the injection, and controlled temperature (blue solid line) by switching the heating source to an oil bath with preset growth temperature. **b)** Change of absorbance peak points of PbSe NRs synthesized with temperature profiles shown in Figure 4.13-a.

To get more insight in to the effects of reaction conditions on PbSe NR, the effect of OA/Pb ratio on NR properties was investigated. In parallel to the previous studies, relationship between the aspect ratio of PbSe NRs and OA/Pb stoichiometric ratio were investigated.[2] As shown in Figure 4.14, aspect ratio and the bandgap of NRs increases with an increase in OA/Pb ratio. Figure 4.14-b and c show the change in the length and the diameter of the NRs with OA/Pb ratio. Increase in OA/Pb ratio leads to longer thinner NRs with a 50 meV increase in the bandgap. Figure 4.14-d, e and f represent the TEM images of the NRs synthesized with OA/Pb ratio of 3.5, 2.5, and 1.5 respectively. Decrease in OA /Pb ratio from 3.5 to 1.5 shortens the NRs from 28.54 ± 5.85 nm to 10.66 ± 1.77 nm whereas the diameter spans a range from 3.20 ± 0.48

nm to 4.30 ± 0.59 nm. Additionally, OA/Pb stoichiometric ratio affects the branching ratio of NRs as reported by Boercher et al.[67] as represented Figure 4.14-d, higher OA/Pb ratio leads to NRs with a significantly high branching percentage, approximately 91%, according to the statistical calculations performed on 140 nanoparticles. On the other hand, very uniform NRs with zero branching percentage were obtained with an optimized OA/Pb ratio (Figure 4.14-e and f).

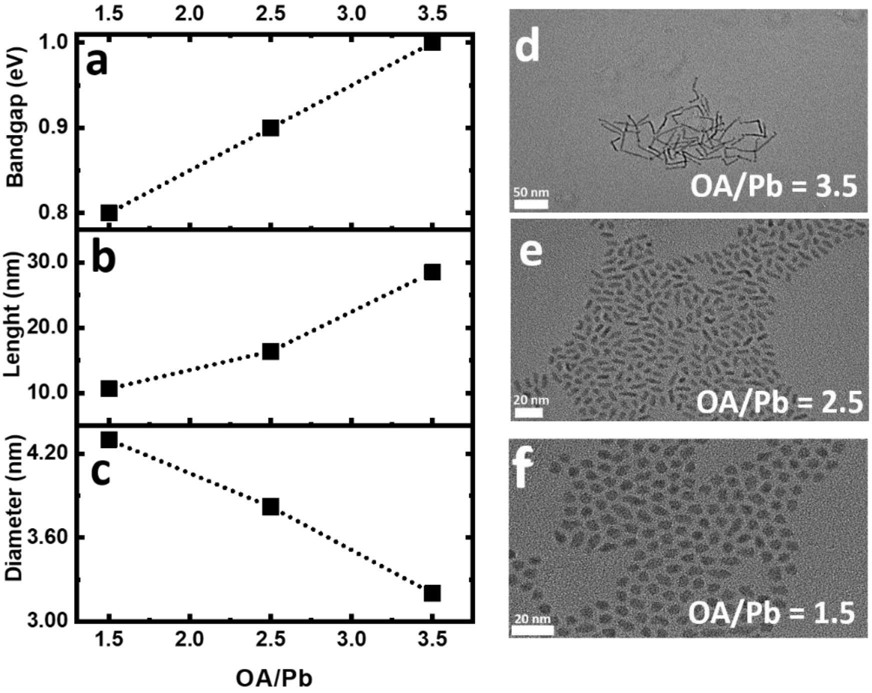

Figure 4.14. The effect of OA/Pb ratio on **a)** bandgap, **b)** length and **c)** diameter of the PbSe NRs. TEM images of PbSe NRs with OA/Pb ratio of **d)** 3.5, **e)** 2.5, and **f)** 1.5. The injection temperature and growth time was 170° C and 2 minutes, respectively.

Previous studies show that the existence of diphenyl phosphine (DPP), a strong reducing agent, plays a profound role in the yield of the quantum dots due to the enhancement of nucleation and faster reaction kinetics.[61,62] Han et al. investigated the effect of DPP on yield of NR synthesis and showed that almost 50% increase in yield can be reached when trans-2-octenoic acid used as an additional ligand source along with oleic acid.[67] The effect of same catalyst, DPP, in the PbSe NR synthesis and on the optical and morphological properties of NRs were investigated. It is observed that a very fast color change right after the injection in the presence of DPP which can be directly attributed to the faster reaction kinetics. Figure 4.15 shows the TEM images of the samples taken at 30, 60 and 90 s after the TDP-Se injection in the absence of DPP catalyst. Dots observed at early stages of the synthesis rapidly fuses to form rods in 90 s in the absence of DPP.

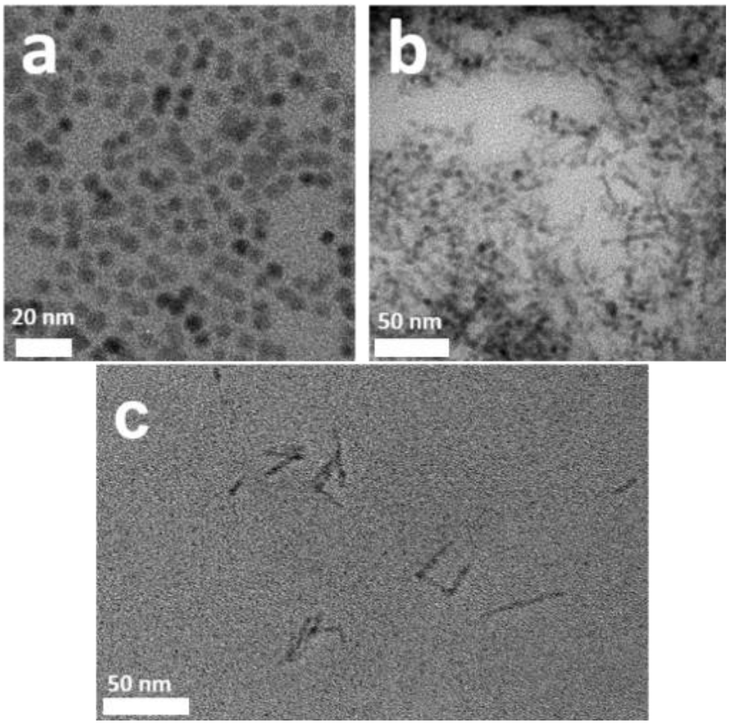

Figure 4.15. TEM images of PbSe NCs with the growth time **a)** 30 s, **b)** 60 s, and **c)** 90 s. The synthesis was done in the absence of DPP. OA/Pb ratio and the injection temperature was 3.5 and 170 °C, respectively.

To assess the effect of DPP on the optical and morphological properties of NRs, a series of synthesis in the presence of various amount of DPP at different injection temperatures were conducted. Table 4.3 summarizes the details of the reaction parameters for the TEM images given in Figure 4.16. HRTEM images of the PbSe

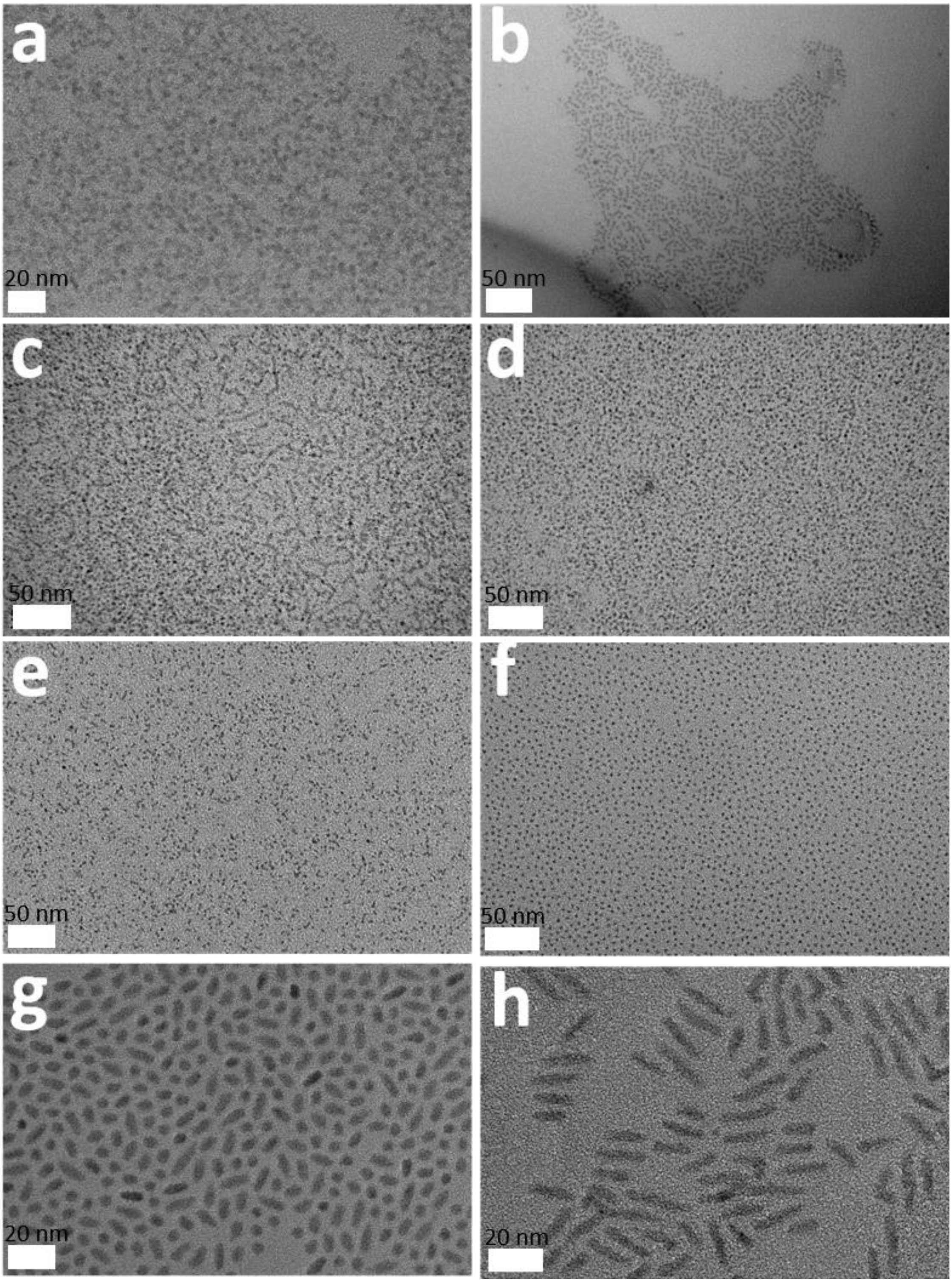

Figure 4.16 Effect of reaction parameters on the morphological properties of PbSe NRs. Details of the reaction parameters of the TEM images are given in Table 4.3.

Table 4.3. Details of the reaction parameters for the HRTEM images given in Figure 4.16.

TEM Label	OA/Pb	T_{INJ} (°C)	V_{DPP} (µl)	Time (s)
a	2.50	170	5	30
b	2.50	170	5	120
c	2.25	120	5	30
d	2.25	120	5	120
e	2.25	120	24.5	120
f	2.25	150	24.5	120
g	2.50	170	1	120
h	2.50	170	0	120

NRs synthesized in the presence of 5 µl DPP, with an injection temperature of 170 °C are shown in Figure 4.16-a and b. Uniform NR formation was not observed in the samples taken from the reaction medium at 30 and 120 s after the injection. Addition of catalyst at a significantly high injection temperature (170 °C) prevents the NR formation due to very fast reaction kinetics. Therefore, the injection temperature was decreased to 120 °C and the catalyst volume was kept constant as 5 µl. Figure 4.16-c and d represent the HRTEM images of the samples taken at 30 and 120 s after the injection. According to the represented data, the NRs formed at early stages breaks up to the dots in time during the growth period. It was noted that the NRs synthesized at lower temperature (120 °C) in the presence of 5 µl DPP were not uniform with a high branching ratio as shown in Figure 4.16-c. In order to reveal the role of concentration of DPP in the NR growth, injection was performed in the presence of 24.5 µl DPP at 120 °C. Figure 4.16-e shows that the percentage of dots increases when catalyst concentration increases. In analogy, increasing the injection temperature to 150 °C in the presence of 24.5 µl DPP leads to the formation of PbSe quantum dots as indicated in Figure 4.16-f.

Results show that DPP is a key parameter in controlling the yield, however has detrimental effect on the NR formation mechanism. NRs with lower uniformity, higher branching percentage and lower yield could be synthesized observed at lower injection temperatures with relatively higher DPP concentration. NRs formed in less than 30 s after the injection breaks up to dots in time as represented in Figure 4.16-a. Splitting of NRs to dots at the beginning of the growth can be controlled with careful optimization of the DPP concentration. As represented in HRTEM image of Figure 4.16-g, more than 50% of the nanostructure were NRs with a diameter and length of 4.3 ± 0.48 nm and 10.6 ± 0.48 nm, respectively when the DPP volume is lowered to 1 µl at an injection temperature of 170 °C.

It can be concluded that PbSe NRs growth mechanism depends on the injection temperature and catalyst (DPP) concentration. In addition, DPP concentration affects both the optical and morphological properties of the PbSe NRs. It was already observed that the excess DPP promotes the formation of QDs by splitting up already formed NRs to QDs at early stages of the growth process. Figure 4.17 displays the change of the bandgap of PbSe NCs synthesized with varying DPP concentration. The optimal injection temperature and growth time were set as 170 °C and 2 minutes, respectively. NR to quantum dot transition was observed at DPP concentration above 1 µl. HRTEM images of the NRs synthesized with 1 µl DPP and without DPP were shown in Figure 4.16-g and h, respectively. Addition of DPP increases the diameter from 3.8 ± 0.45 nm to 4.3 ± 0.48 nm and decreases the length from 16.41 ± 3.47 nm to 10.66 ± 1.82 nm.

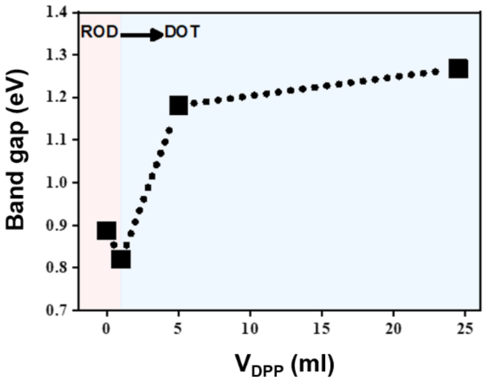

Figure 4.17. The effect of DPP concentration on the optical properties of PbSe NRs. All of the data points belong to separate experiments with injection temperature and growth time set to 170 °C and 2 min, respectively.

4.2.2. Surface Stability and Passivation

It is well known that PbSe QDs undergo surface oxidation and up to 50% of their volume is transformed into PbO, SeO_2, or $PbSeO_3$ within 24 h in ambient conditions.[68] Stability tests done by spectroscopic measurements indicated in Figure 4.18 shows that PbSe NRs also have high sensitivity toward air and moisture. 30 nm blue shift in the absorbance peak was observed for the PbSe NRs stored in air for 90 days as indicated in Figure 4.18-a. Blue shift in absorbance peaks of the PbSe quantum dots has been attributed to the oxidation of surface atoms.[69] 78% loss in intensity is attributed to the non-radiative decay channels formed due to surface oxidation of NRs in air, as represented in PL spectrum in Figure 4.18-b.[70] HRTEM images of the fresh and aged PbSe NRs indicated as insets in Figure 4.18 show that the oxidation starts from the surface and proceeds towards core.

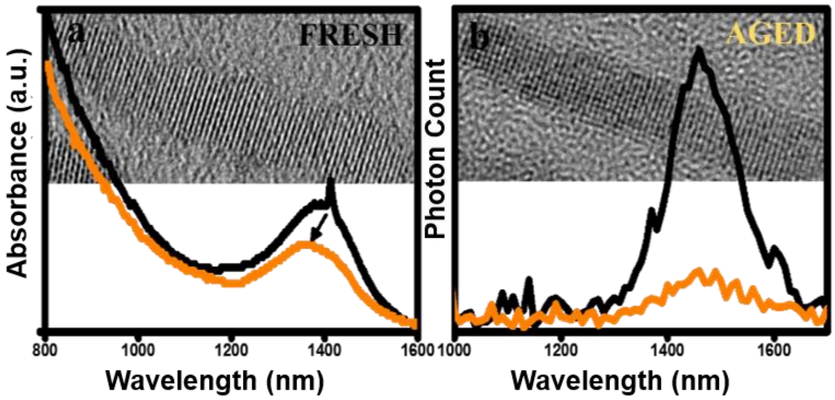

Figure 4.18. Effects of air exposure on the optical and surface properties of PbSe NRs. **a)** Absorption of fresh (black) and aged (orange) PbSe NRs. Inset: HRTEM images of the fresh PbSe NRs. **b)** Photoluminescence spectra of fresh (black) and aged (orange) PbSe NRs. Inset: HRTEM images of the aged PbSe NRs (λ_{ex}=980 nm).

A series of PbSe NRs (as shown in Figure 4.19) with aspect ratios is changing from 10.44 ± 2.69 nm to 2.98 ± 0.63 nm were synthesized to examine the impact of length and diameter on the air exposure. Aspect ratio of NRs were controlled by varying the

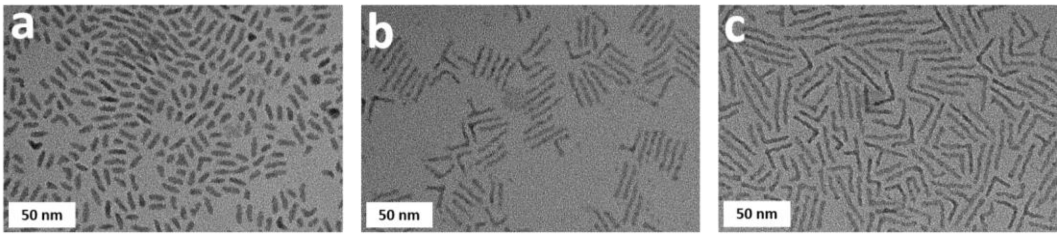

Figure 4.19. TEM images of **a)** shortest NRs with >1% branching percentage, **b)** medium NRs with 12% branching percentage, **c)** longest NRs with 37% branching percentage. Injection temperature is 170 °C for all of the experiment, OA/Pb ratio was 3.22, 2.75 and 1.75, respectively.

stabilizing agent concentration. The general trend is the formation of elongated and thinner PbSe NRs with higher concentrations of capping ligand. Figure 4.19 shows HRTEM images of NRs which in an increasing branching ratio from less than 1% to 37% as OA/Pb ratio increases. Figure 4.20 shows the diameter and length distribution which synthesized in three different OA/Pb ratio at 170 °C. Size statistics were measured from HRTEM images using ImageJ analysis program.[47] It is noteworthy

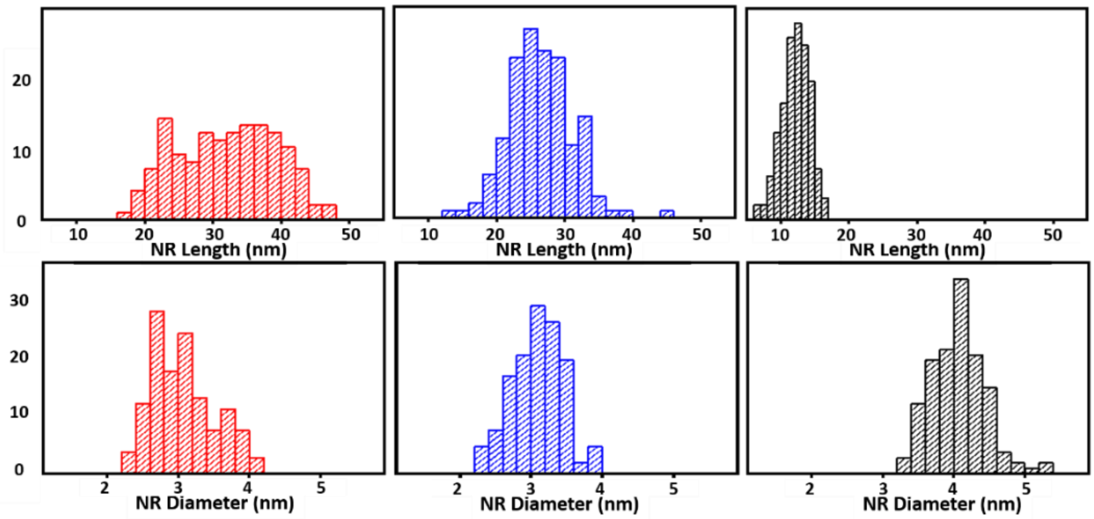

Figure 4.20. The diameter and length distribution of NRs with the aspect ratio as longest (red), medium (blue), and shortest (black). Injection temperature is 170 °C for all experiment. OA/Pb ratio was 3.22 (red), 2.75 (blue) and 1.75 (black). TEM images of corresponding PbSe NR are shown in Figure 4.19.

that lower aspect ratio and lower ratio of branching were obtained for lower OA/Pb ratio.

Absorbance and photoluminescence of dilute solution of as synthesized OA-capped NRs were measured in atmospheric conditions. Figure 4.21-a and b show absorption and photoluminescence spectra and same samples measured again after air exposure for a defined time interval. The first transition peak of the un-passivated PbSe NR solution samples blue shifted by 4.8 meV, 8.9 meV and 38.7 meV for NRs with lengths 31.95 ± 7.14 nm, 26.43 ± 4.69 nm and 12.12 ± 2.28 nm, respectively. Thin films of PbSe NRs ligand exchanged with BDT were prepared with LBL spin casting method for the Fourier-transform infrared (FTIR) as shown in Figure 4.21-d. FTIR spectra demonstrate that NRs with lower aspect ratio have a larger intensity absorption at the C–H stretching frequency around 2900 cm^{-1} (2855, 2924 and 2956 cm^{-1}). Thin films were exposed to air to investigate the stability behavior of NRs in solid state as shown

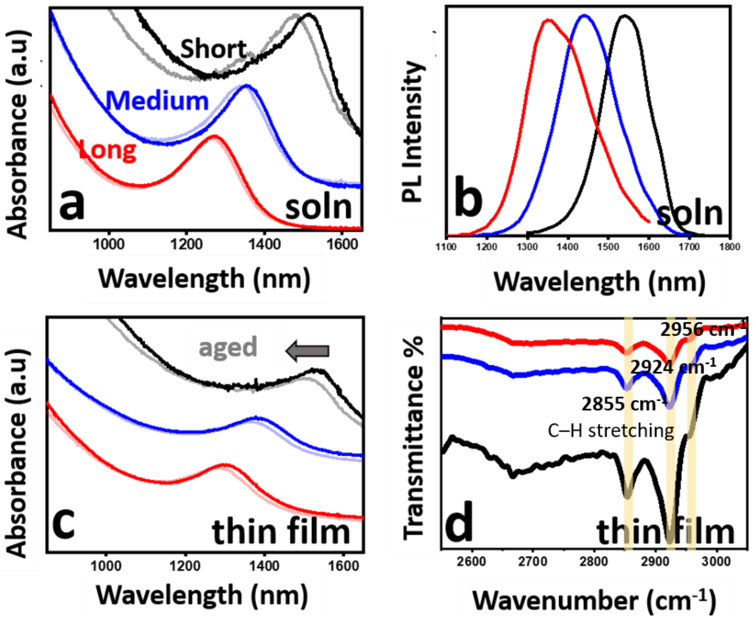

Figure 4.21. **a)** Absorbance spectra and, **b)** photoluminescence spectra of the of PbSe NRs in solution (λ_{ex}=980 nm). **c)** Absorbance spectra, and **d)** FTIR spectra of BDT exchanged PbSe NRs with bandgap energies 0.95 eV (red), 0.90 eV (blue) and 0.81 eV (black) within a decreasing aspect ratio. FTIR spectrum was normalized with respect to the absorption spectra of the samples.

in Figure 4.21-c. Within two weeks, NRs with largest aspect ratio showed 6 nm blue shift whereas the NRs with smallest aspect ratio showed lower air resistance and exhibited a 48 nm shift.

Additionally, X-ray scattering diffraction (XRD) pattern shown in Figure 4.22-a, showed (111), (200), (220), (331), (400, (420) and (422) lattice planes at 24.04, 29.17, 41.67, 48.83, 51.71, 68.62, 76.08 degree, respectively (JCPDS-ICDD card 06-0354). According to previous studies, the attachment of PbSe NCs can be along of {100}, {110}, or {111} facets, depending on the surfactant molecules present in the reaction solution.[71,55] In the presence of shorter chain capping agents, preferred alignment of NRs were reported along the ⟨100⟩ direction as shown in Figure 4.24 by the enhanced (200) peak in XRD pattern. Also, HRTEM images of individual rods show well-resolved lattice planes corresponding to the interplanar distance of 0.30 nm, consistent with the (200) d-spacing of PbSe rock-salt structure as shown in Figure 4.22-b.

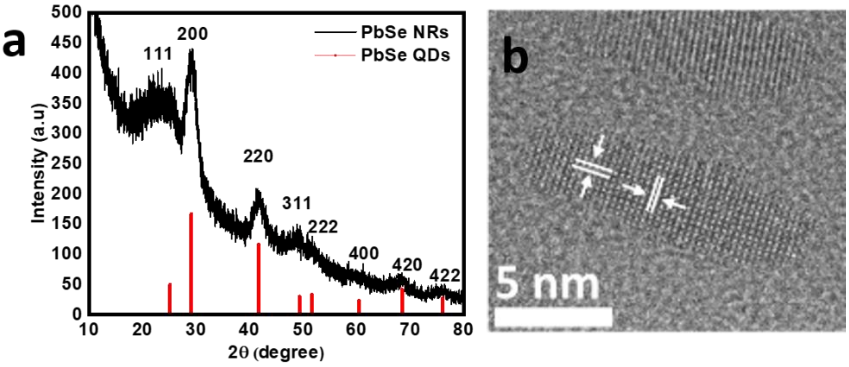

Figure 4.22. **a)** XRD diffractions of thin film of EDT exchanged PbSe NRs spin coated on glass **b)** HRTEM image of PbSe NRs with lattice fringes of 0.30 nm.

Faster oxidation rate of the shorter PbSe NRs may also be in relation to the ratio of {100}/{111} facets which have known to have a significant effect on the surface stability.[72] Presence of excess Pb atoms on the {111} facets and higher affinity for ligand binding to the Pb atoms leads to a higher degree of protection on the surface Se atoms, which in turn suggest that {100} facets are more susceptible to oxidation due to higher degree of ligand loss.[73] NRs align preferentially along the ⟨100⟩ direction with ⟨111⟩ facets placed on the outer shell which is proved from the enhanced (200) diffraction signal in XRD pattern. This suggests that the shorter NRs with higher {100} facets (NR ends) relative to {111} facets will lead to higher sensitivity towards oxidation due to less protected Se atoms on the surface.

Ultraviolet photoelectron spectroscopy (UPS) method was adopted to determine the band edge energies with respect to vacuum in PbSe NR films with three different NRs samples, whereas the conduction band are getting closer to the vacuum within an increasing aspect ratio as shown in Table 4.4 and Figure 4.23.

Table 4.4. Band edge energies of the PbSe NRs within a changing aspect ratio based on UPS measurement.

d (nm)	l (nm)	E_G (eV)	V_B (eV)	C_B (eV)	E_F / E_v	Shift[a] (nm)
4.07 ± 0.39	12.12 ± 2.28	0.81	4.79 ± 0.05	3.98 ± 0.05	3.84	48
3.19 ± 0.34	26.43 ± 4.69	0.89	4.84 ± 0.05	3.95 ± 0.05	3.84	11
3.06 ± 0.45	31.95 ± 7.14	0.95	4.79 ± 0.05	3.84 ± 0.05	3.84	6

[a] blue shift on the peak point of absorbance signal of the sample during the two weeks in atmospheric conditions.

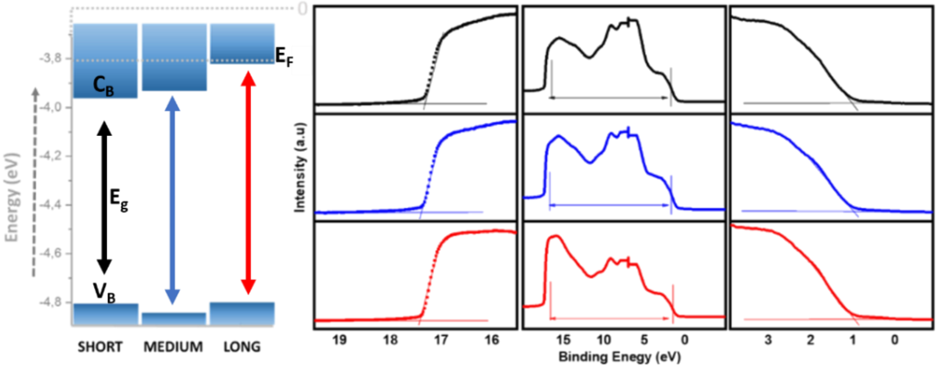

Figure 4.23. Band edge energies based on the UPS measurements of the PbSe NRs thin films with a length as longest (red), medium (blue), and shortest (black).

To contribute to the endurance of the PbSe NRs towards oxidation and remove the MGSs, a modified passivation procedure with $CdCI_2$ was adopted for NRs.[2] The reaction temperature was decreased to 100 °C after TDP-Se injection and prepared $CdCI_2$ solution was injected to reaction medium. The reaction was terminated in 10 s and the growth phase passivated SynP-PbSe NRs were isolated (for details see Chapter 3.4.2). According to Figure 4.24, the PL count of the SynP-PbSe NRs is 5 times higher than that of UP-PbSe NRs. Higher PL count can be assigned to the removal of MGSs.

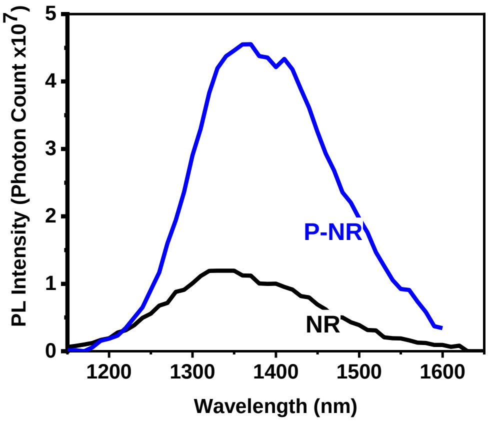

Figure 4.24.Effect of growth phase passivation on PbSe NRs. Photoluminescence spectra of thin films of EDT treated PbSe NRs (black) and SynP-NR (blue) (λ_{ex}=980 nm).

4.2.3. Solar Cell Fabrication

Utilization of PbSe NRs in solar cells have been studied in few studies (see Chapter 2.2.1 for details). [2,74] High ability to generate multiple excitons is one of the most intriguing properties of the PbSe NRs. However, only-NR (E_G = 1.0 eV) cells treated with TBAI and EDT showed poor device performance as well as the photocurrent extractions as shown in Figure 4.25 due to structural obstacles like forming poor quality thin films resulting aggregations and pinholes was also shown by Han et al.[74]

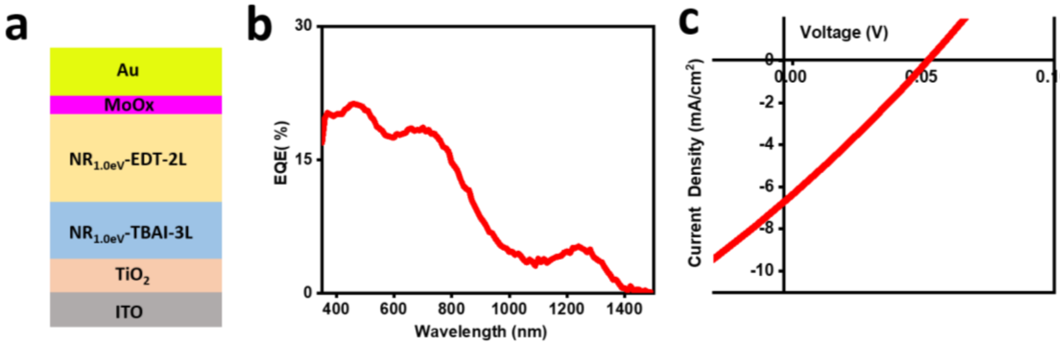

Figure 4.25. Role of NRs in solar cell application. **a)** Device architecture **b)** external quantum efficiencies and **c)** current density-voltage behavior of the cells with a device architecture of NR1.0 eV-TBAI -3L / NR1.0 eV- EDT-2L.

4.2.3.1. What is the role of NR in photovoltaics?

To get more insight about the photovoltaic performance of NRs, devices consists of PbSe NRs and also QDs with hydrazine and EDT functionalized ligand were fabricated. NR cells consisted of five layers of PbSe NRs (E_G = 0.8 eV) and two layers of PbSe QDs (E_G = 1.4 eV) as electron blocking layer shown in Figure 4.26. The band alignment demonstrates the role of the PbSe-EDT (E_G = 1.4 eV) layer as an electron blocking/hole extraction layer between the PbSe NR layer and the anode (Au), which leads to an improved photocurrent as illustrated in Figure 4.26-c and Table 4.5. In NR device (see Figure 4.26-a), electron flow from PbSe NR layer to the anode, which is in the opposite direction to the photocurrent, and interfacial recombination at the interface between PbSe NR and anode are possible loss mechanisms. When two layers of EDT exchanged PbSe QD (E_G = 1.4 eV) were used, the conduction band offset between the NR and EDT-QD layers provides an energy barrier that prevents photogenerated electrons (filled circles) from flowing to the EDT-QD layer as shown in Figure 4.26-b. The addition of the EDT-QD (E_G = 1.4 eV) layer not only prevents electron flow from PbSe NR layer to the anode but may also minimize surface recombination of photogenerated electrons and holes at the interface between PbSe NR and the anode due to filling the empty spaces.[75]

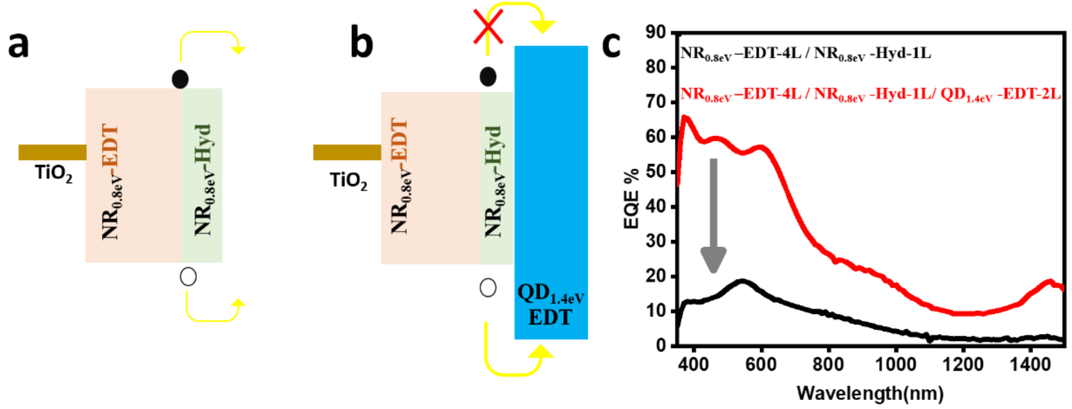

Figure 4.26. The role of the electron blocking layer. Band edge energies with respect to vacuum were determined by UPS spectroscopy **a)** with and **b)** without electron blocking layer (QD$_{1.4\ eV}$- EDT -2L). **a)** External quantum efficiencies of the cells with a device architecture of NR$_{0.8\ eV}$- EDT -4L / NR$_{0.8\ eV}$- Hyrazine-1L (black) and NR$_{0.80\ eV}$ - EDT-4L / NR$_{0.8\ eV}$- Hyrazine-1L / QD$_{1.4\ eV}$- EDT -2L (red).

Table 4.5. Device parameters for PbSe QD and NR Solar Cells (ITO/TiO$_2$/PbSe QDs-PbSe NRs/ MoOx/Au) (shown in Figure 4.26) under AM 1.5 spectral illumination (1000 W/m^2). [a]

Device Architecture	**V$_{OC}$ (V)**	**J$_{SC}$ (mA/cm^2)**	**FF (%)**	**PCE (%)**
NR$_{0.8\ eV}$- EDT -4L/ NR$_{0.8\ eV}$ -Hyd. -1L	0.03 ± 0.01 (0.03)	5.60 ± 0.56 (6.5)	25.3 ± 3.4 (29.31)	0.04 ± 0.01 (0.05)
NR$_{0.8\ eV}$- EDT -4L/ NR$_{0.8\ eV}$ -Hyd. -1L/ **QD$_{1.4\ eV}$- EDT -2L**	0.27 ± 0.01 (0.27)	13.3 ± 0.56 (14.1)	23.9 ± 0.6 (24.51)	0.87 ±0.02 (0.90)

[a] Results were averaged with standard deviation across 5-8 devices. The J$_{SC}$, V$_{OC}$, FF, and PCE of the devices with maximum efficiencies are quoted in the brackets.

[b] Theoretical J$_{SC}$ calculated by integrating the EQE spectrum with the AM 1.5 G solar spectrum.

In order to investigate the photovoltaic performance of NRs, devices consist of post-preparative surface passivated NRs and also QDs with thiol-functionalized ligand (EDT) were fabricated. NR devices (device B) consisted of two layers of PbSe NRs (E$_G$ = 0.95 eV) and two layers of PbSe QDs (E$_G$ = 1.4 eV) as electron blocking layer. For the reference device (device A), first two layers of NR were replaced with the PbSe QDs with similar band gap energy (E$_G$ = 1.0 eV). Band energies with respect to vacuum level were determined by UPS measurement and illustrated in Figure 4.27-a,b. Current-voltage behavior showed a sharp increase in V_{OC} for device B (0.33 ± 0.01 V) while the V_{OC} of reference device A yielded 0.17 ± 0.01 V as shown in Figure 4.27-c. The reason of this rise can be explained by higher band banding between the TiO_2 layer and the active layer of device B (PbSe NR). The collected photocurrent from device A and device B were measured as 17.50 ± 0.74 mA/cm^2 and 16.37 ± 0.07 mA/cm^2, respectively. Theoretical J_{SC} value of the solar cells calculated by integrating the EQE spectrum with the AM 1.5 G solar spectrum was calculated as 17.68 mA/cm^2 and 16.07 mA/cm^2 for device A and device B, respectively as represented in Figure 4.27-d. Good agreement of the J_{SC} measured from J-V test station and calculated from EQE measurements allows one to crosscheck the

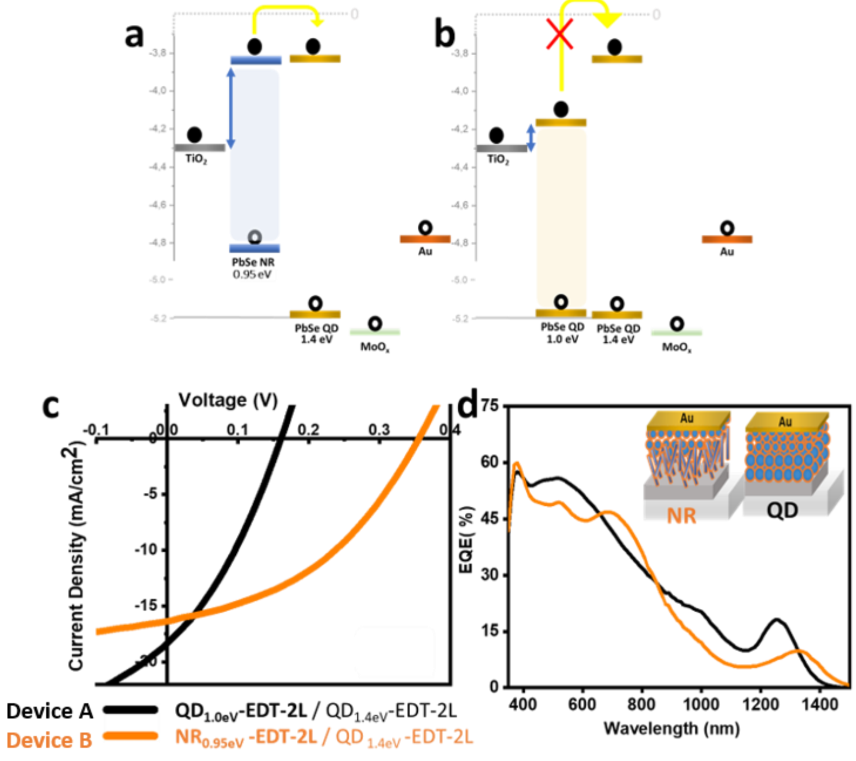

Figure 4.27. Band edge energies with respect to vacuum were determined by UPS spectroscopy for **a)** PbSe NR **b)** PbSe QD solar cells. **c)** Current density-voltage behavior and **d)** external quantum efficiencies of the cells with a device architecture of $QD_{1.0\ eV}$- EDT -2L / $QD_{1.4\ eV}$- EDT-2L (device A, black) and SynP-$NR_{0.95\ eV}$ - EDT-2L / $QD_{1.4\ eV}$- EDT -2L (device B, orange).

consistency of the measurements. The slight decrease can be a as result of the pinholes in the NR layer or due to trap states which are known to affect the charge collection efficiencies.[76]

As shown in Table 4.6, the sharp rise in the V_{OC} and FF lead to an enhancement in PCE from 1.01 ± 0.08 % to 2.11 ± 0.20 % when QDs are replaced with NRs, which can be attributed to the improved charge carrier mobility of NRs compared with QDs.[42] Also, as shown in Table 4.7, the shunt resistance (R_{SH}) of the device B was about five times higher than that of the device A, which is in a good agreement with the improved V_{OC} and FF. The high R_{SH} indicates that the NR layers can significantly reduce the number of current leakage pathways and charge carrier recombination in the devices.

Table 4.6. Device parameters for PbSe QD and NR Solar Cells (ITO/TiO$_2$/PbSe QDs-PbSe NRs/ MoOx/Au) (shown in Figure 4.27) under AM 1.5 spectral illumination (1000 W/m^2). [a]

Device Architecture	**V_{OC} (V)**	**J_{SC} (mA/cm^2)**	**FF (%)**	**PCE (%)**	**J_{SC} from EQE [b] (mA/cm^2)**
Device A **QD$_{1.0\ eV}$- EDT -2L** / QD$_{1.4\ eV}$- EDT-2L	0.17 ± 0.01 (0.18)	17.50 ± 0.74 (18.76)	34.06 ± 0.90 (34.9)	1.01 ± 0.08 (1.10)	16.68
Device B **SynP-NR$_{0.95\ eV}$-EDT-2L/** QD$_{1.4\ eV}$- EDT -2L	0.33 ± 0.01 (0.35)	16.37 ± 0.07 (16.43)	40.32 ± 1.79 (41.49)	2.11 ± 0.20 (2.40)	16.07

[a] Results were averaged with standard deviation across 5-8 devices. The J_{SC}, V_{OC}, FF, and PCE of the devices with maximum efficiencies are quoted in the brackets.

[b] Theoretical J_{SC} calculated by integrating the EQE spectrum with the AM 1.5 G solar spectrum.

Table 4.7. Additional device parameters for PbSe QD and NR Solar Cells (ITO/TiO$_2$/PbSe QDs-PbSe NRs/ MoOx/Au) (shown in Figure 4.27). [a]

Device Architecture	**R_S (ohm cm^2)**	**R_{SH} (ohm cm^2)**
QD$_{1.0\ eV}$- EDT -2L / QD$_{1.4\ eV}$- EDT-2L	5.75	18.38
SynP-NR$_{0.95\ eV}$-EDT-2L / QD$_{1.4\ eV}$- EDT -2L	9.50	97.46

[a] R_{SH} and R_S were determined from the slope of the IV curve near J_{SC} and V_{OC} points, respectively.

Nathaniel et al. reported the first solar cell composed of PbSe NRs and generate multiple excitons.[2] PbSe NRs with 0.80 eV, 0.95 eV, and 1.05 eV reached 109 ± 3 %, 113 ± 4%, and 122 ± 3 % EQE, respectively. Although impressive EQE values have been reported, the TEM images shows non-uniform samples composed of highly branched nanoparticles with different shape and size. Another study reported by Han. et al. showed that the solar cells fabricated by using NRs yield extremely low PCE which was attributed to the poor film formation or NRs.[74] Formation of pinholes and low packing density of NRs during spin coating have been reported to be the main reasons of low current densities and PCE. [74]

In the light of this observations, a bulk nano-heterojunctions (BNH) platform in which NRs were blended with QDs was suggested. Cells were designed in a way an energy cascaded structure allows carriers to be extracted effectively by the respective electrodes. The first layer of the cells was composed of a thin layer of the QDs (E_G = 1.0 eV) to improve the contact between the electron transporting TiO_2 layer and NR layer. Then a BNH layer composed of PbSe QDs (E_G = 1.0 eV) and PbSe NRs (E_G = 1.0 eV) mixture, was spin coated to improve the film morphology. On the top of the pinhole free BNH layer, a thin layer of PbSe QDs with E_G = 1.4 eV was coated as hole transporting layer. BNH mixture was prepared by blending PbSe QDs (50 mg/ml) with PbSe NRs (50 mg/ml) in an equal volume. In order to investigate the effect of bulk nano-heterojunction concept, two cells composed of NRs only and BNH layer are compared and results are represented in Figure 4.28. Comparison of these two devices showed that the BNH platform provides an enhancement in J_{SC} from 16.54 ± 0.63 mA/cm^2 to 20.29 ± 0.90 mA/cm^2 and V_{OC} from 0.24 ± 0.01 V to 0.27 ± 0.01 V as shown in J-V characteristics in Table 4.8. Increase in the EQE of the cells in UV region of the spectrum that corresponds to MEG suggest a higher generation rate of excitons (see Figure 4.28-a). Besides better morphology of thin films ensured higher FF (37.28 ± 2.7 %) and PCE (1.92 ± 0.12 %) as shown in Table 4.8.

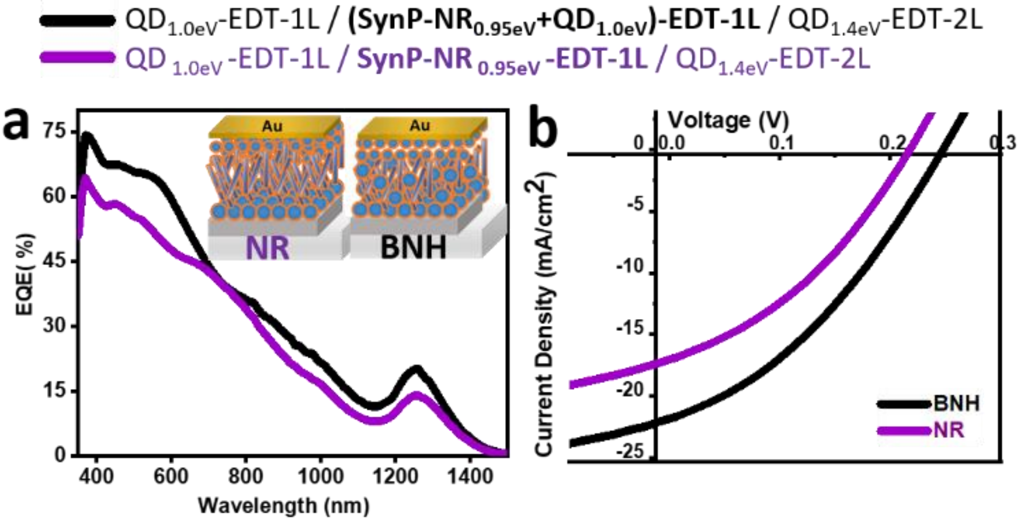

Figure 4.28. Effect of BNH platform on solar cell characteristics. **a)** External quantum efficiencies and **b)** current density-voltage behavior of the devices with a device architecture of $QD_{1.0\ eV}$- EDT-1L / (SynP-$NR_{0.95\ eV}$ + $QD_{1.0\ eV}$)-EDT-1L / $QD_{1.4\ eV}$- EDT-2L (black) and $QD_{1.0\ eV}$- EDT-1L / SynP-$NR_{0.95\ eV}$-EDT-1L / $QD_{1.4\ eV}$- EDT-2L (purple).

Table 4.8. Device parameters for BNH of PbSe NR and PbSe QD Solar Cells (ITO/TiO_2/NR or BNH/QD/MoOx/Au) (shown in Figure 4.28) under AM 1.5 spectral illumination (1000 W/m^2). [a]

Cells	**V_{OC} (V)**	**J_{SC} (mA/cm^2)**	**FF (%)**	**PCE (%)**	**Jsc from EQE (mA/cm^2) [b]**
$NR_{0.95\ eV}$ + $QD_{1.0\ eV}$	0.27 ± 0.01 (0.28)	20.29 ± 0.90 (21.62)	37.28 ± 2.7 (41.34)	1.92 ± 0.12 (2.05)	20.33
$NR_{1.0\ eV}$	0.24 ± 0.01 (0.25)	16.54 ± 0.63 (17.21)	35.17 ± 0.90 (36.23)	1.36 ± 0.13 (1.55)	17.27

[a]Results were averaged with standard deviation across 5-8 devices. The J_{SC}, V_{OC}, FF, and PCE of the devices with maximum efficiencies are quoted in the brackets.

[b] Theoretical J_{SC} calculated by integrating the EQE spectrum with the AM 1.5 G solar spectrum.

To get more insight about the role of each layer in the BNH platform in cell performance, thicknesses of the layers were optimized. Device architectures and EQE spectrums are illustrated in Figure 4.29-a, and the results are summarized in Table 4.9. Comparison between cell B and C reveals the effect of thickness of the front NR layer when total thickness of the cell is kept constant. Optimum thickness of the front NR layer was found as 2 layers due to the slight decrease in J_{SC} for thicker NR front layer and sharp increase in EQE in the UV region for the thinner front layer as shown in Figure 4.29-a. When device A, C and D are compared, the role of the thickness of the BNH platform can be understood. A sharp decrease in device parameters was observed when the number of BNH layer was increased. In addition to this, maximum EQE was reached in UV region was measured from device C which reveals that thinner BNH layer decreases the recombination for the electron and hole pairs.

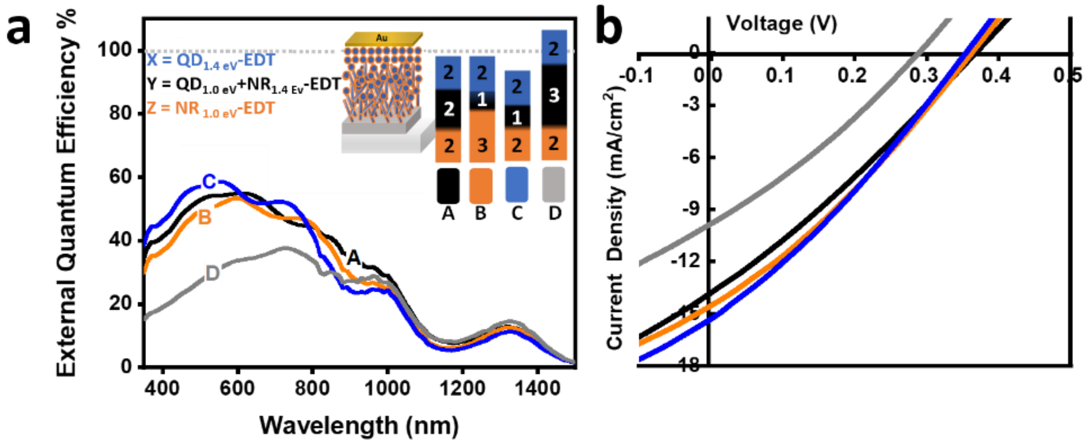

Figure 4.29. Optimization of the thickness of the layers in the bulk nano-heterojunction platform. **a)** External quantum efficiencies and **b)** J-V characteristics of the cells. Devices with different thickness are denoted by letters (A, B, C and D) and the generalized device architecture is provided as inset. Front $NR_{1.0\ eV}$ layer, middle BNH layer ($NR_{1.0\ eV}$ + $QD_{1.4\ eV}$) and back $QD_{1.4\ eV}$ layer thicknesses are denoted by X, Y and Z. Device A: X=2, Y=2, Z=2, B: X=3, Y=1, Z=2, C: X=2, Y=1, Z=2 and D: X=2, Y=3, Z=2.

Table 4.9. Device parameters for BNH of PbSe NR and PbSe QD Solar Cells (ITO/TiO_2/NR/ BNH/QD/MoOx/Au) (shown in Figure 4.29) under AM 1.5 spectral illumination (1000 W/m^2). [a]

Cells	V_{OC} (V)	J_{SC} (mA/cm^2)	FF (%)	PCE (%)
A	0.36 ± 0.01 (0.37)	12.57 ± 0.93 (13.80)	28.58 ± 0.87 (29.70)	1.33 ± 0.11 (1.45)
B	0.35 ± 0.01 (0.36)	13.56 ± 0.83 (14.54)	29.97 ± 0.28 (30.31)	1.46 ±0.10 (1.61)
C	0.35 ± 0.01 (0.36)	14.27 ± 0.78 (15.31)	29.76 ± 0.81 (30.36)	1.51 ± 0.10 (1.62)
D	0.31 ± 0.02 (0.33)	9.51 ± 2.70 (9.83)	28.87 ± 0.29 (29.19)	0.88 ± 0.03 (0.91)

[a] Results were averaged with standard deviation across 5-8 devices. The J_{SC}, V_{OC}, FF, and PCE of the devices with maximum efficiencies are quoted in the brackets.

In addition to thickness, NR to QD ratio is another parameter that controls the generation and extraction of excitons through the cells. To investigate the effect of NR/QD ratio in BNH layer, several cells were prepared in which NR/QD ratio set as 0:1, 1:3,1:2, 1:1, 2:1 and 1:0. The device architecture is shown in Figure 4.30-a. The NR/QD ratio of the middle BNH layer was changed while the front and back layers 1:2. The maximum EQE in the MEG region was also measured from the cells with NR:QD ratio of 1:2 as represented in Figure 4.30-c.

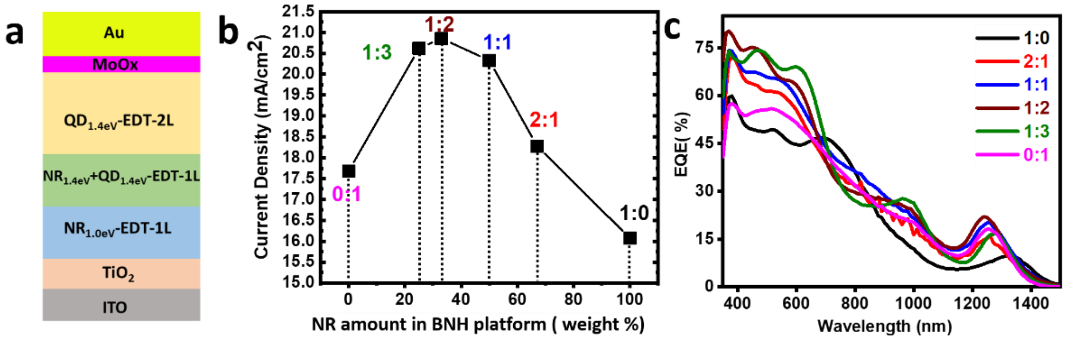

Figure 4.30. Effect of NR:QD ratio in cells with BNH architecture. **a)** The cell architecture used for the optimization study. NR:QD ratio was changed as 0:1 (pink), 1:3 (green), 1:2 (brown), 1:1 (blue), 2:1 (red), 1:0 (black).**b)** change of theoretical current densities (calculated by integrating the EQE spectrum with the AM 1.5 G solar spectrum) with NR/QD ratio and **c)** External quantum efficiencies of the cells.

Strong dependence of EQE/J_{SC} on the NR/QD ratio in BNH layer suggest the presence of energy transfer from NRs to QDs. The photoluminescence of thin films were measured to investigate the energy transfer from NRs to QDs which act as donor and acceptor, respectively. Thin films with alternating NR/QD ratios were prepared and PL spectra are shown in Figure 4.31. A sharp decrease in PL intensity was observed when the QD/ NR ratio increased to 2:1. Quenching of PL can be attributed to the presence of non-radiative energy transfer from NRs to QDs.

Table 4.10. Device parameters for cells shown in Figure 4.32 under AM 1.5 spectral illumination (1000 W/m^2). [a]

NR: QD ratio	J_{SC} (mA/cm^2)	V_{OC} (V)	FF (%)	PCE (%)	J_{SC} from EQE (mA/cm^2) [b]
0:1	17.50 ± 0.74 (18.76)	0.17 ± 0.01 (0.18)	34.06 ± 0.9 (34.9)	1.01 ± 0.08 (1.10)	17.68
1:3	19.70 ± 0.83 (20.70)	0.29 ± 0.02 (0.32)	34.10 ± 0.9 (35.31)	1.93 ± 0.25 (2.26)	20.62
1:2	17.37 ± 1.01 (18.81)	0.25 ± 0.01 (0.26)	30.66 ± 0.3 (31.21)	1.34 ± 0.07 (1.46)	20.86
1:1	20.29 ± 0.90 (21.62)	0.27±0.01 (0.28)	37.28 ± 2.7 (41.34)	1.92 ± 0.12 (2.05)	20.33
2:1	18.79 ± 1.09 (19.71)	0.25 ± 0.03 (0.28)	36.71 ± 2.1 (39.67)	1.77 ± 0.47 (2.20)	18.28
1:0	16.37 ± 0.07 (16.43)	0.33 ± 0.01 (0.35)	40.32 ± 1.8 (41.49)	2.11 ± 0.20 (2.40)	16.07

[a] Results were averaged with standard deviation across 5-8 devices. The J_{SC}, V_{OC}, FF, and PCE of the devices with maximum efficiencies are quoted in the brackets.

[b] Theoretical J_{SC} calculated by integrating the EQE spectrum with the AM 1.5 G solar spectrum.

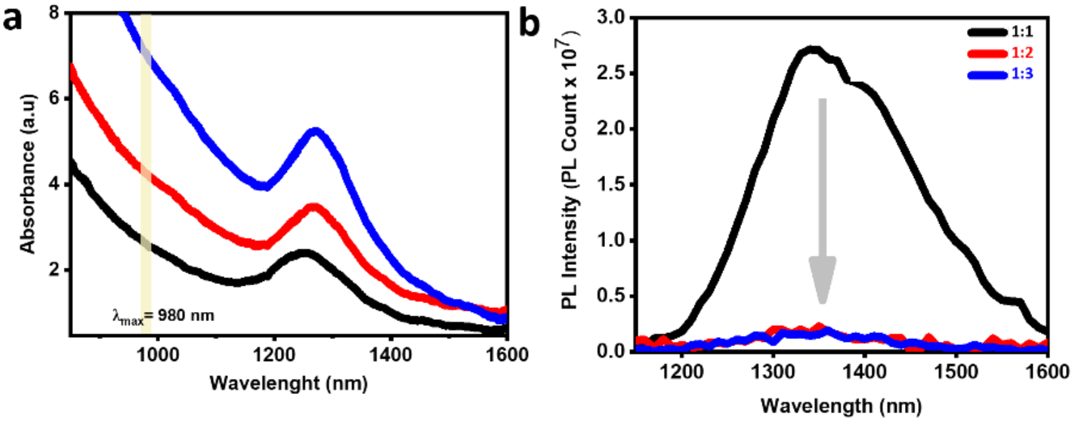

Figure 4.31. **a)** Absorbance and **b)** Photoluminescence spectra of thin films of PbSe NRs prepared as changing QD to NR ratio as 1:1 (black), 2:1 (red), and 3:1 (blue) (λ_{ex}=980 nm).

4.2.3.2. How does ligand type effects the photovoltaic performance?

The electrical properties are strongly dependent on the choice of exchanging ligand. Previous studies showed that containing ligands such as TBAI, PbI_2, and CdI_2 exhibit suppressed recombination, faster charge transfer rate, and longer carrier lifetimes than EDT capped PbSe QDs.[77] In the light of these observations, cells consisting of one layer of PbSe QD (E_G = 1.0 eV) as front layer and one layer of BNH mixture were fabricated using different types of ligands as represented in Figure 4.32-a. According to the cell parameters summarized in Table 4.11, maximum current and PCE were obtained from EDT exchanged NRs in contrast to the QDs where cell performance has been reported to be higher for ligands that contain iodine.

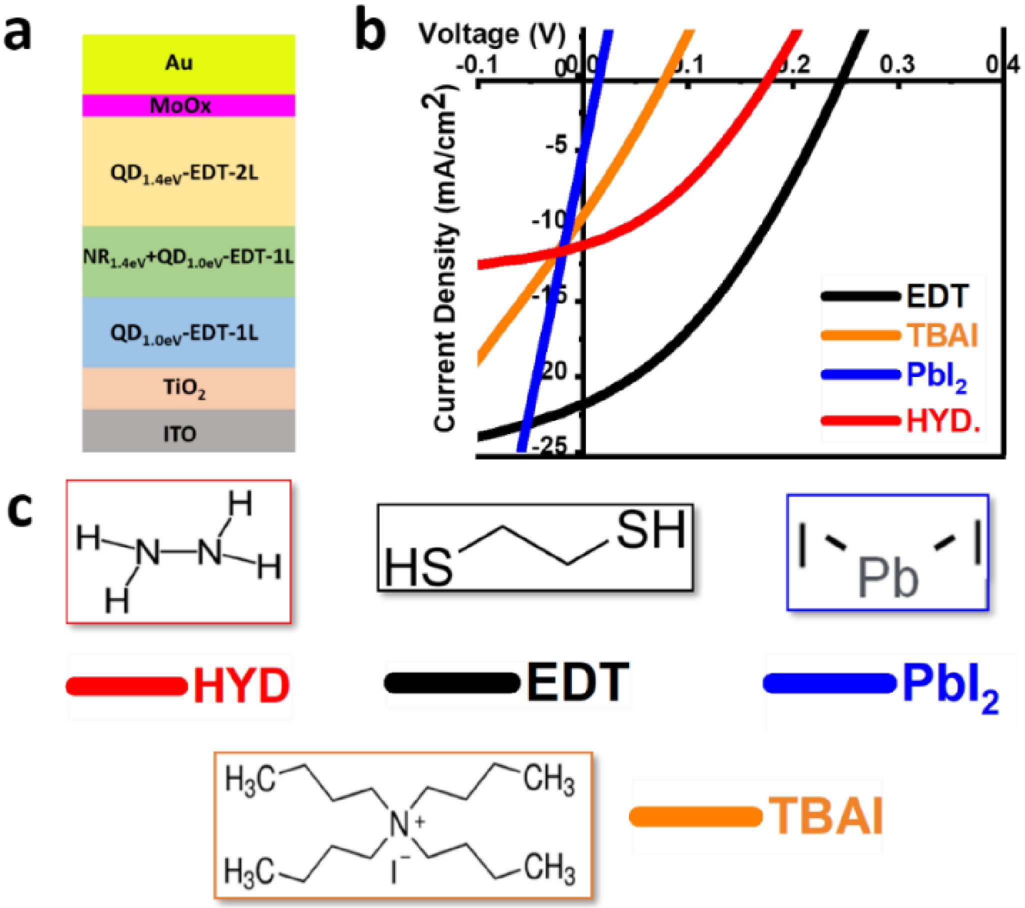

Figure 4.32.Role of ligand type on the solar cell characteristics. **a)** Cell architecture, **b)** Current density-voltage behavior of the devices with a device architecture shown in a and **c)** structures of ligand which were used.

Table 4.11. Device Parameters for PbSe QD and NR Solar Cells (ITO/TiO_2/PbSe QDs /BNH /PbSe QDs / MoOx/Au) (shown in Figure 4.32) under AM 1.5 spectral illumination (1000 W/m^2). [a]

Ligand	**V_{OC} (V)**	**J_{SC} (mA/cm^2)**	**FF (%)**	**PCE (%)**	**J_{SC} from EQE (mA/cm^2) [b]**
PbI_2	0.02 ± 0.01 (0.02)	4.91 ± 0.22 (5.07)	27.56	0.051± 0.07 (0.074)	-
TBAI	0.13 ± 0.01 (0.15)	10.55 ± 0.71 (11.62)	28.07± 1.82 (30.92)	0.39 ± 0.07 (0.50)	9.14
Hydrazine	0.18 ± 0.00 (0.18)	11.14 ± 0.63 (11.63)	34.80 ± 1.07 (36.51)	0.68 ± 0.08 (0.77)	12.35
EDT	0.27 ± 0.01 (0.28)	20.29 ± 0.90 (21.62)	37.28 ± 2.7 (41.34)	1.92 ± 0.12 (2.05)	20.33

[a] Results were averaged with standard deviation across 5-8 devices. The J_{SC}, V_{OC}, FF, and PCE of the devices with maximum efficiencies are quoted in the brackets.

[b] Theoretical J_{SC} calculated by integrating the EQE spectrum with the AM 1.5 G solar spectrum.

To investigate the effect of ligand structure on cell parameters further, another small organic passivating ligand, BDT was tested and the results are summarized in Figure 4.33-b and Table 4.12. Comparison of device A with device C shows that maximum current is obtained from EDT whereas maximum V_{OC} is obtained from BDT exchanged QDs. All the device parameters dropped dramatically when one layer of NRs ligand exchanged with BDT (device B) was inserted to the device A. Different behavior was observed when device C is composed to device D where the front QD layer was replaced by NRs in device D. In addition to dramatic drop in the cell parameters, maximum EQE in the UV region also show a significant drop when BDT is used as the ligand exchange reagent. Additionally, lack of excitonic peak of NRs at 1300 nm in the EQE spectrum (Figure 4.33-a) when BDT is used as ligand exchange reagent points out to the limitations on the excitation operation. Enhanced EQE at all wavelength when EDT is used suggest the significance of ligand structure.

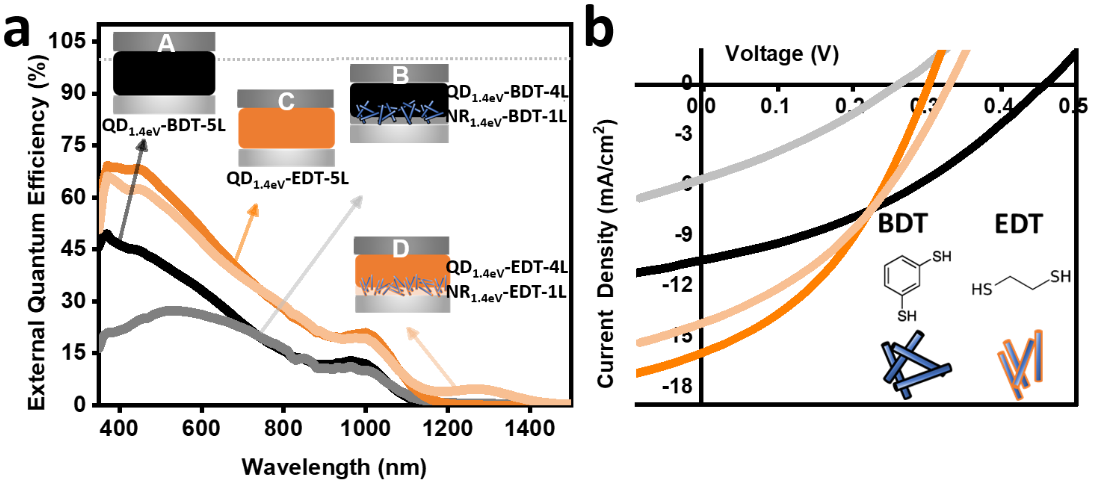

Figure 4.33. Effect of ligand type on the PbSe NR (E_G = 1.0 eV) with PbSe QD (E_G = 1.4 eV) solar cell characteristics. **a)** External quantum efficiencies and b) current density-voltage behavior of the devices with a device architectures of $QD_{1.4eV}$-BDT-5L (black), $NR_{1.0eV}$-BDT-1L / $QD_{1.4eV}$-BDT-4L (gray), $QD_{1.4eV}$-EDT-5L (dark orange) and $NR_{1.0eV}$- EDT-1L/ $QD_{1.4eV}$- EDT-4L (light orange).

To investigate the effects of ligand structure on the morphology of thin films, TEM images of BDT and EDT exchanged PbSe NRs were investigated as represented in Figure 4.34-a and b, respectively. EDT exchanged NRs are aligned in a more ordered way due to the reduced interparticle spacings. However, BDT exchanged NRs-yield poorly interconnected NRs which might have detrimental effects on exciton generation transport. On the other hand, higher degree of order due to preferential orientation of NRs enhance the device parameters and exciton generation at all wavelengths.

In addition to the reduced cell parameters due to the disordered thin films of BDT exchanged NRs, photophysical properties were also found to be strongly dependent on the ligand structure and thin film morphology. Figure 4.34-c shows the photoluminescence spectra of thin films prepared from EDT and BDT ligand exchanged PbSe NRs. Almost six times higher PL intensity of EDT exchanged NRs can be assigned to the high sensitivity of excited state dynamics and recombination pathways on thin film morphology

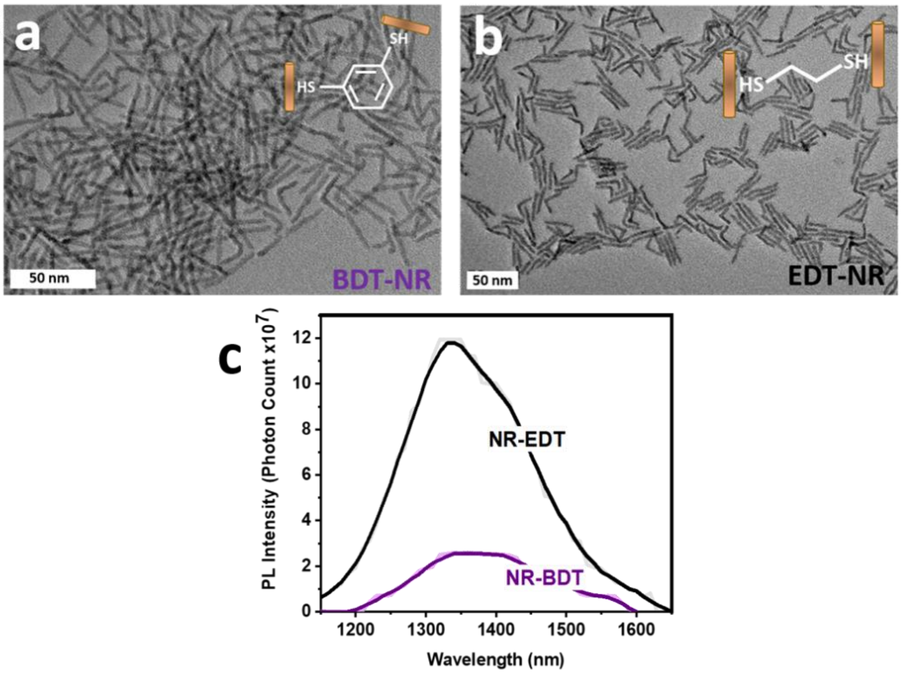

Figure 4.34. TEM images of **a)** BDT and **b)** EDT capped PbSe NRs. Samples were prepared with dip coating method onto 200 Mesh, carbon coated copper TEM grids. **c)** Photoluminescence spectra of thin films of PbSe NRs treated with EDT (black) and BDT (purple).

Table 4.12. Device Parameters for PbSe QD and NR Solar Cells (ITO/TiO$_2$/PbSe QDs-PbSe NRs/ MoOx/Au) (shown in Figure 4.33) under AM 1.5 spectral illumination(1000 W/m^2). [a]

Devices	V_{OC} (V)	J_{SC} (mA/cm^2)	FF (%)	PCE (%)
QD$_{1.4eV}$ - BDT-5L **Device (A)**	0.40 ± 0.05 (0.46)	12.54 ± 2.93 (11.05)	34.54 ± 1.02 (36.42)	1.43 ± 0.22 (1.67)
NR$_{1.0eV}$ -BDT-1L / QD$_{1.4eV}$ -BDT-4L **Device (B)**	0.22 ± 0.03 (0.26)	4.58 ± 1.5 (5.62)	29.66 ± 3.0 (31.51)	0.30±0.12 (0.43)
QD$_{1.4eV}$ -EDT-5L **Device (C)**	0.30	15.16 ± 0.61 (15.93)	37.83 ± 1.20 (38.96)	1.64 ± 0.97 (1.77)
NR$_{1.0eV}$ -EDT-1L / QD$_{1.4eV}$ - EDT-4L **Device (D)**	0.29 ± 0.03 (0.33)	14.75 ± 0.43 (15.22)	36.86 ± 0.75 (37.38)	1.48 ±0.17 (1.66)

[a]Results were averaged with standard deviation across 5-8 devices. The J_{SC}, V_{OC}, FF, and PCE of the devices with maximum efficiencies are quoted in the brackets.

To investigate the stability behavior of PbSe NR solar cells, several ligands known to enhance the endurance of NRs towards ambient conditions were applied during the study. Preliminary studies showed that PbI_2 and CdI_2 reagents with optimized concentrations minimizes the air sensitivity of the cells. Stability behavior of an unoptimized cell architecture is shown in Figure 4.35-a. Current density of the devices remained almost same up to 54 days under inert atmosphere after a sharp rise in the first 100 h. The reason of this sharp rise in J_{SC} and PCE is under investigation and the role of mixed ligand strategy will be investigated further on the cells to enhance the air stability of PbSe NR based solar cells.

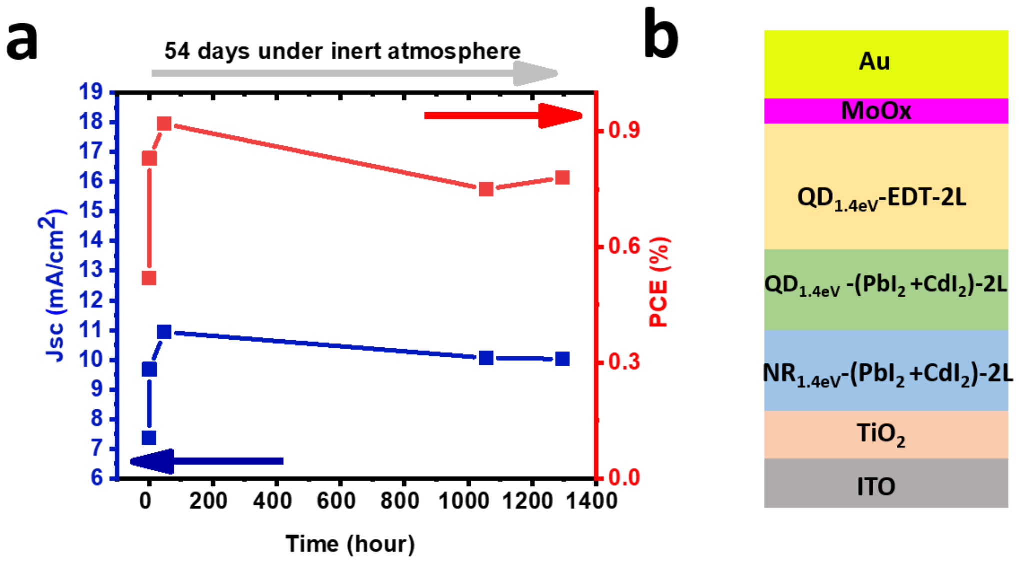

Figure 4.35. Stability behavior of solar cells. **a)** Current density (blue) and power conversion efficiency (red) of cells and **b)** device architecture of the cells. A mixture of PbI_2 and CdI_2 with 1:2 molar ratio in DMF were used as ligand exchange medium.

CHAPTER 5

CONCLUSIONS

In summary, extremely air stable thin films and solar cells utilizing dually passivated PbTe QDs are reported in the first part of the study. Discovery of the strong dependence of the stability on the size and shape enables us to reveal the origins of the air instability which diminishes beyond a critical size (3.6-3.9 nm) where the shape changes from octahedron to truncated octahedron. Growth phase ligand exchange method determines the shape of the QDs by controlling the {111}/ {200} facet ratio and bound halides have command of the LBL process by improving the resistance of the surface atoms to oxidation, eliminating the MGS formation, increasing the ligand exchange rate and dictating the crystal packing direction. Utilization of the combinatorial surface passivation protocol with passivating reagents like RbI and CdI_2, targets the traps states formed during the solid-state ligand exchange process. Moreover, the solar cells prepared from the dually passivated PbTe QDs exhibit higher PCEs and un-encapsulated cells retain their photovoltaic performance for more than six months. The challenge in controlling the surface properties of the QDs during the growth phase and ligand exchange processes (such as LBL) has been one of the major obstacles hindering the utilization of the PbTe QDs in solid state electronic devices. In this sense, results of study will provide useful information to the community for the development of PbTe QD based solid state electronics as well as for the other lead chalcogenides in the near future. In the second part of the study, the optical and morphological properties of PbSe NRs were tuned by several reaction parameters such as injection temperature, growth temperature profile, OA/Pb ratio and DPP concentration. The aspect ratio of PbSe NRs strongly depends on OA/Pb ratio. Increasing OA/Pb ratio increases the length and branching percentage of NRs while the diameter remains almost same. Transformation of dots to rods starts when the OA/Pb ratio increases from 1.5 to 3.5. The optimum ratio for the minimum branching and maximum length was found as 2.5. The existence of DPP plays a profound role in the rate of the reaction and yield. Increase in the yield comes at the cost of inhibiting the NR formation mechanism. Excess DPP promotes the formation of QDs by splitting up already formed NRs to QDs at early stages of the growth process. Optimized DPP concentration and injection temperature lead to uniform and unbranched PbSe NRs. PbSe NRs shows degradation signs after exposure to ambient conditions. Solar cells containing CdI_2 and PbI_2 ligand exchanged PbSe NRs show a performance with a slight decrease in device performance for more than 50 days storage in nitrogen filled glovebox. Solar cells contain only PbSe NRs showed a poor performence due to the poor thin film formation. On the other hand, fabrication of devices using a mixture of PbSe NRs and PbSe QDs (bulk nano heterojunction) enhances photo current in the UV region which correspond to the MEG process. In addition, ligand type and structure affects the device performance changing the photocurrent of the devices. Utilization of the EDT exchanged PbSe NRs leads to a small interparticle spacings and ordered alignment with respect to the BDT exchanged PbSe NRs. Moreover, non radiative energy transfer between the PbSe QDs and PbSe NRs was observed with the PL measurement. Further studies will be devoted to reach the MEG from the devices containing PbSe NRs and PbTe QDs by the optimizations on the electron transport layer.

REFERENCES

1. Asil D, Walker BJ, Ehrler B, et al. Role of PbSe structural stabilization in photovoltaic cells. *Adv Funct Mater*. 2015;25(6):928-935. doi:10.1002/adfm.201401816
2. Davis NJLK, Böhm ML, Tabachnyk M, et al. Multiple-exciton generation in lead selenide nanorod solar cells with external quantum efficiencies exceeding 120%. *Nat Commun*. 2015;6(May):1-7. doi:10.1038/ncomms9259
3. Shockley W, Queisser HJ. Detailed balance limit of efficiency of p-n junction solar cells. *J Appl Phys*. 1961;32(3):510-519. doi:10.1063/1.1736034
4. Rogach AL, Gaponik N, Lupton JM, et al. Light-emitting diodes with semiconductor nanocrystals. *Angew Chemie - Int Ed*. 2008;47(35):6538-6549. doi:10.1002/anie.200705109
5. Aydt AP, Blair S, Zhang H, Chernomordik BD, Beard MC, Berezin MY. Synthesis and spectroscopic evaluation of PbS quantum dots emitting at 1300 nm for optimized imaging in optical window II. *Reporters, Markers, Dye Nanoparticles, Mol Probes Biomed Appl VIII*. 2016;9723(April 2016):97230Z. doi:10.1117/12.2214509
6. Eisler HJ, Sundar VC, Bawendi MG, Walsh M, Smith HI, Klimov V. Color-selective semiconductor nanocrystal laser. *Appl Phys Lett*. 2002;80(24):4614-4616. doi:10.1063/1.1485125
7. García De Arquer FP, Gong X, Sabatini RP, et al. Field-emission from quantum-dot-in-perovskite solids. *Nat Commun*. 2017;8:1-8. doi:10.1038/ncomms14757
8. Shrestha A, Batmunkh M, Tricoli A, Qiao SZ, Dai S. Near-Infrared Active Lead Chalcogenide Quantum Dots: Preparation, Post-Synthesis Ligand Exchange, and Applications in Solar Cells. *Angew Chemie - Int Ed*. 2019. doi:10.1002/anie.201804053
9. Ganesan A, Houtepen A, Crisp R. Quantum Dot Solar Cells: Small Beginnings Have Large Impacts. *Appl Sci*. 2018;8(10):1867. doi:10.3390/app8101867
10. Klimov V. *Nanocrystal Quantom Dots*. Vol 134.; 2007.

11. By P. World ’ s largest Science , Technology & Medicine Open Access book publisher.

12. Chukwuocha EO, Onyeaju MC, Harry TST. Theoretical Studies on the Effect of Confinement on Quantum Dots Using the Brus Equation. *World J Condens Matter Phys*. 2012;02(02):96-100. doi:10.4236/wjcmp.2012.22017

13. Talapin D V., Lee JS, Kovalenko M V., Shevchenko E V. Prospects of colloidal nanocrystals for electronic and optoelectronic applications. *Chem Rev*. 2010;110(1):389-458. doi:10.1021/cr900137k

14. Talapin D V., Rogach AL, Haase M, Weller H. Evolution of an ensemble of nanoparticles in a colloidal solution: Theoretical study. *J Phys Chem B*. 2001;105(49):12278-12285. doi:10.1021/jp012229m

15. Lamer VK, Dinegar RH. Theory, Production and Mechanism of Formation of Monodispersed Hydrosols. *J Am Chem Soc*. 1950;72(11):4847-4854. doi:10.1021/ja01167a001

16. Park J, Joo J, Soon GK, Jang Y, Hyeon T. Synthesis of monodisperse spherical nanocrystals. *Angew Chemie - Int Ed*. 2007;46(25):4630-4660. doi:10.1002/anie.200603148

17. Haciefendioglu T, Alptekin DA. PbSe Nanorods for hybrid solar cells: Optimization of synthesis protocols and investigation of surface stability. *PVCon 2018 - Int Conf Photovolt Sci Technol*. 2018. doi:10.1109/PVCon.2018.8523936

18. Bodnarchuk MI, Kovalenko M V. Engineering colloidal quantum dots. *Colloid Quantum Dot Optoelectron Photovoltaics*. 2013:1-29. doi:10.1017/cbo9781139022750.002

19. Ravich YI. *Semiconducting Lead Chalcogenides*. Plenum Press; 1970. doi:10.1007/978-1-4684-8607-0

20. Yin Y, Alivisatos AP. Colloidal nanocrystal synthesis and the organic-inorganic interface. *Nature*. 2005;437(7059):664-670. doi:10.1038/nature04165

21. Wu Z, Yang S, Wu W. Shape control of inorganic nanoparticles from solution. *Nanoscale*. 2016;8(3):1237-1259. doi:10.1039/c5nr07681a

22. Hersch P, Zweibel K. *Basic Photovoltaic Principles and Methods*. United

States of America: Technical Information Office; 1982.

23. Riordan C, Hulstrom R. What is an air mass 1.5 spectrum? *IEEE*. 1990:1085-1088. doi:0160-8371/90/0000-1085

24. Air Mass | PVEducation. https://www.pveducation.org/pvcdrom/properties-of-sunlight/air-mass. Accessed December 27, 2019.

25. The global standard spectrum (AM1-5g). https://www2.pvlighthouse.com.au/resources/courses/altermatt/The Solar Spectrum/The global standard spectrum (AM1-5g).aspx. Accessed December 27, 2019.

26. Ocilovo BYC, Ashimura AKIH, Weet DOJT, Outsas TO V, Orwood ROAN. Highly transparent light-harvesting window film. 2015;54(30):8990-8998.

27. This Month in Physics History. https://www.aps.org/publications/apsnews/200904/physicshistory.cfm. Accessed December 27, 2019.

28. Fraas LM. History of Solar Cell Development. In: *Low-Cost Solar Electric Power*. Cham: Springer International Publishing; 2014:1-12. doi:10.1007/978-3-319-07530-3_1

29. Best Research-Cell Efficiency Chart | Photovoltaic Research | NREL. https://www.nrel.gov/pv/cell-efficiency.html. Accessed December 27, 2019.

30. Löper P, Pysch D, Richter A, et al. Analysis of the temperature dependence of the open-circuit voltage. *Energy Procedia*. 2012;27:135-142. doi:10.1016/j.egypro.2012.07.041

31. Series Resistance | PVEducation. https://www.pveducation.org/pvcdrom/solar-cell-operation/series-resistance. Accessed December 27, 2019.

32. Shunt Resistance | PVEducation. https://www.pveducation.org/pvcdrom/solar-cell-operation/shunt-resistance. Accessed December 27, 2019.

33. Ananda W. External quantum efficiency measurement of solar cell. *QiR 2017 - 2017 15th Int Conf Qual Res Int Symp Electr Comput Eng*. 2017;2017-Decem(July 2017):450-456. doi:10.1109/QIR.2017.8168528

34. Instrumentation for quantum efficiency measurement of solar cells - Renewable Energy World. https://www.renewableenergyworld.com/2010/07/01/instrumentation-for-

quantum-efficiency-measurement-of-solar-cells/#gref. Accessed December 27, 2019.

35. Rational Design of Solar Cells for Efficient Solar Energy Conversion - Google Kitaplar. https://books.google.com.tr/books?id=uzptDwAAQBAJ&pg=PT356&lpg=PT356&dq=solar+cells+are+categorized+as+first+second+third&source=bl&ots=mJOzvh_k-m&sig=ACfU3U034DL8SJXNFvSngBZfcFRMMG3FMw&hl=tr&sa=X&ved=2ahUKEwiekfKuuNXmAhXF0aQKHVlEA1QQ6AEwC3oECAoQAQ#v=onep. Accessed December 27, 2019.

36. Polman A, Knight M, Garnett EC, Ehrler B, Sinke WC. Photovoltaic materials: Present efficiencies and future challenges. *Science (80-)*. 2016;352(6283). doi:10.1126/science.aad4424

37. Solar Efficiency Limits. http://solarcellcentral.com/limits_page.html. Accessed December 27, 2019.

38. Nozik AJ. Multiple exciton generation in semiconductor quantum dots. *Chem Phys Lett*. 2008;457(1-3):3-11. doi:10.1016/j.cplett.2008.03.094

39. Böhm ML, Jellicoe TC, Tabachnyk M, et al. Lead telluride quantum dot solar cells displaying external quantum efficiencies exceeding 120%. *Nano Lett*. 2015;15(12):7987-7993. doi:10.1021/acs.nanolett.5b03161

40. Semonin OE, Luther JM, Choi S, et al. Peak external photocurrent quantum efficiency exceeding 100% via MEG in a quantum dot solar cell. *Science (80-)*. 2011;334(6062):1530-1533. doi:10.1126/science.1209845

41. Speirs MJ, Dirin DN, Abdu-Aguye M, Balazs DM, Kovalenko M V., Loi MA. Temperature dependent behaviour of lead sulfide quantum dot solar cells and films. *Energy Environ Sci*. 2016;9(9):2916-2924. doi:10.1039/C6EE01577H

42. Padilha LA, Stewart JT, Sandberg RL, et al. Carrier multiplication in semiconductor nanocrystals: Influence of size, shape, and composition. *Acc Chem Res*. 2013;46(6):1261-1269. doi:10.1021/ar300228x

43. Urban JJ, Talapin D V., Shevchenko E V., Murray CB. Self-assembly of PbTe quantum dots into nanocrystal superlattices and glassy films. *J Am Chem Soc*. 2006. doi:10.1021/ja058269b

44. Murphy JE, Beard MC, Norman AG, et al. PbTe colloidal nanocrystals:

Synthesis, characterization, and multiple exciton generation. *J Am Chem Soc*. 2006;128(10):3241-3247. doi:10.1021/ja0574973

45. Koh WK, Bartnik AC, Wise FW, Murray CB. Synthesis of monodisperse PbSe nanorods: A case for oriented attachment. *J Am Chem Soc*. 2010;132(11):3909-3913. doi:10.1021/ja9105682

46. Yang L, Tabachnyk M, Bayliss SL, et al. Solution-processable singlet fission photovoltaic devices. *Nano Lett*. 2015;15(1):354-358. doi:10.1021/nl503650a

47. ImageJ. https://imagej.nih.gov/ij/index.html. Accessed December 27, 2019.

48. Carlson B, Leschkies K, Aydil ES, Zhu XY. Valence band alignment at cadmium selenide quantum dot and zinc oxide $(10\bar{1}0)$ interfaces. *J Phys Chem C*. 2008;112(22):8419-8423. doi:10.1021/jp7113434

49. LANGFORD BJI, WILSON AJC. Scherrer after Sixty Years: A Survey and Some New Results in the Determination of Crystallite Size. *J Appl Cryst*. 11:102-113. doi:10.1061/9780784479896.140

50. Han L, Fang H, Du C, Sun J, Li Y, Ma W. Synthesis of ultra-narrow PbTe nanorods with extremely strong quantum confinement. *J Mater Sci Technol*. 2019;35(5):703-710. doi:10.1016/j.jmst.2018.10.019

51. Bode DE, Levinstein H. Effect of oxygen on the electrical Properties of Lead telluride films. *Phys Rev*. 1954;96(2):259-265. doi:10.1103/PhysRev.96.259

52. Jacquemoud S, Ustin SL. *Application of Radiative Transfer Models to Moisture Content Estimation and Burned Land Mapping*.

53. Tan L, Li P, Sun B, Chaker M, Ma D. Stabilities Related to Near-Infrared Quantum Dot-Based Solar Cells: The Role of Surface Engineering. *ACS Energy Lett*. 2017;2(7):1573-1585. doi:10.1021/acsenergylett.7b00194

54. Tang J, Kemp KW, Hoogland S, et al. Colloidal-quantum-dot photovoltaics using atomic-ligand passivation. *Nat Mater*. 2011;10(10):765-771. doi:10.1038/nmat3118

55. Choi J, Ko J-H, Kim Y-H, Jeong S. Steric-Hindrance-Driven Shape Transition in PbS Quantum Dots: Understanding Size-Dependent Stability. *J Am Chem Soc*. 2013;135:5278-5281.

56. Morgan WE, Van Wazer JR. Binding energy shifts in the X-ray photoelectron spectra of a series of related group IV-a compounds. *J Phys Chem*.

1973;77(7):964-969. doi:10.1021/j100626a023

57. Mandale AB, Badrinarayanan S. X-ray photoelectron spectroscopic studies of the semimagnetic semiconductor system Pb1-xMnxTe. *J Electron Spectros Relat Phenomena*. 1990;53(1-2):87-95. doi:10.1016/0368-2048(90)80343-9

58. Kraut EA, Grant RW, Waldrop JR, Kowalczyk SP. Semiconductor core-level to valence-band maximum binding-energy differences: Precise determination by x-ray photoelectron spectroscopy. *Phys Rev B*. 1983;28(4):1965-1977. doi:10.1103/PhysRevB.28.1965

59. Hewavitharana IK, Brock SL. When Ligand Exchange Leads to Ion Exchange: Nanocrystal Facets Dictate the Outcome. *ACS Nano*. 2017;11(11):11217-11224. doi:10.1021/acsnano.7b05534

60. Casavola M, Van Huis MA, Bals S, Lambert K, Hens Z, Vanmaekelbergh D. Anisotropic cation exchange in PbSe/CdSe core/shell nanocrystals of different geometry. *Chem Mater*. 2012;24(2):294-302. doi:10.1021/cm202796s

61. Steckel JS, Yen BKH, Oertel DC, Bawendi MG. On the mechanism of lead chalcogenide nanocrystal formation. *J Am Chem Soc*. 2006;128(40):13032-13033. doi:10.1021/ja062626g

62. Joo J, Pietryga JM, McGuire JA, et al. A Reduction Pathway in the Synthesis of PbSe Nanocrystal Quantum Dots. *J Am Chem Soc*. 2009;131(30):10620-10628. doi:10.1021/ja903445f

63. Kim D, Kim DH, Lee JH, Grossman JC. Impact of stoichiometry on the electronic structure of PbS quantum dots. *Phys Rev Lett*. 2013;110(19). doi:10.1103/PhysRevLett.110.196802

64. Ko DK, Maurano A, Suh SK, et al. Photovoltaic Performance of PbS Quantum Dots Treated with Metal Salts. *ACS Nano*. 2016;10(3):3382-3388. doi:10.1021/acsnano.5b07186

65. Semonin OE, Luther JM, Choi S, et al. in a Quantum Dot Solar Cell. *Science (80-)*. 2011;334(December):1530-1534. doi:10.1126/science.1209845

66. Cunningham PD, Boercker JE, Foos EE, et al. Enhanced multiple exciton generation in quasi-one-dimensional semiconductors. *Nano Lett*. 2011;11(8):3476-3481. doi:10.1021/nl202014a

67. Boercker JE, Foos EE, Placencia D, Tischler JG. Control of PbSe nanorod

aspect ratio by limiting phosphine hydrolysis. *J Am Chem Soc*. 2013;135(40):15071-15076. doi:10.1021/ja404576j

68. Zhao F, Mukherjee S, Ma J, Li D, Elizondo SL, Shi Z. Influence of oxygen passivation on optical properties of PbSe thin films. *Appl Phys Lett*. 2008;92(21):211110. doi:10.1063/1.2938417

69. Hughes BK, Ruddy DA, Blackburn JL, et al. Control of PbSe quantum dot surface chemistry and photophysics using an alkylselenide ligand. *ACS Nano*. 2012;6(6):5498-5506. doi:10.1021/nn301405j

70. Ip AH, Thon SM, Hoogland S, et al. Hybrid passivated colloidal quantum dot solids. *Nat Nanotechnol*. 2012;7(9):577-582. doi:10.1038/nnano.2012.127

71. Argeri M, Fraccarollo A, Grassi F, Marchese L, Cossi M. Density functional theory modeling of PbSe nanoclusters: Effect of surface passivation on shape and composition. *J Phys Chem C*. 2011;115(23):11382-11389. doi:10.1021/jp201112x

72. Hacıefendioğlu T, Solmaz TK, Erkan M, Asil D. A comprehensive approach for the instability of PbTe quantum dots and design of a combinatorial passivation strategy. *Sol Energy Mater Sol Cells*. 2020;207. doi:10.1016/j.solmat.2019.110362

73. Choi JJ, Bealing CR, Bian K, et al. Controlling Nanocrystal Superlattice Symmetry and Shape-Anisotropic Interactions through Variable Ligand Surface Coverage. *J Am Chem Soc*. 2011;133(9):3131-3138. doi:10.1021/ja110454b

74. Han L, Liu J, Yu N, et al. Facile synthesis of ultra-small PbSe nanorods for photovoltaic application. *Nanoscale*. 2015;7(6):2461-2470. doi:10.1039/c4nr05707d

75. Chuang CHM, Brown PR, Bulović V, Bawendi MG. Improved performance and stability in quantum dot solar cells through band alignment engineering. *Nat Mater*. 2014;13(8):796-801. doi:10.1038/nmat3984

76. Rath AK, Pelayo Garcia de Arquer F, Stavrinadis A, et al. Remote Trap Passivation in Colloidal Quantum Dot Bulk Nano-heterojunctions and Its Effect in Solution-Processed Solar Cells. *Adv Mater*. 2014;26(27):4741-4747. doi:10.1002/adma.201400297

77. Zhang Y, Ding C, Wu G, et al. Air Stable PbSe Colloidal Quantum Dot

Heterojunction Solar Cells: Ligand-Dependent Exciton Dissociation, Recombination, Photovoltaic Property, and Stability. *J Phys Chem C*. 2016;120(50):28509-28518. doi:10.1021/acs.jpcc.6b10920

CHAPTER 6

APPENDIX

6.1. APP-1

XPS spectrum of UP-PbTe QD

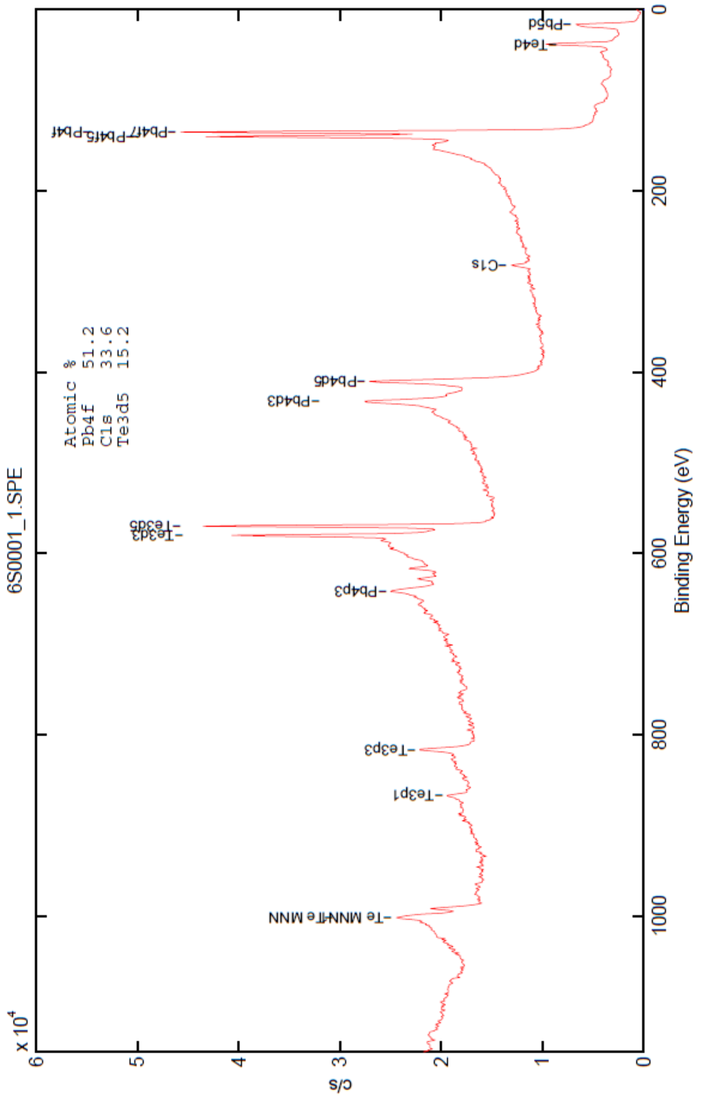

Figure 6.1. XPS spectrum of UP-PbTe QD.

6.2. APP-2

XPS spectrum of SynP-PbTe QD

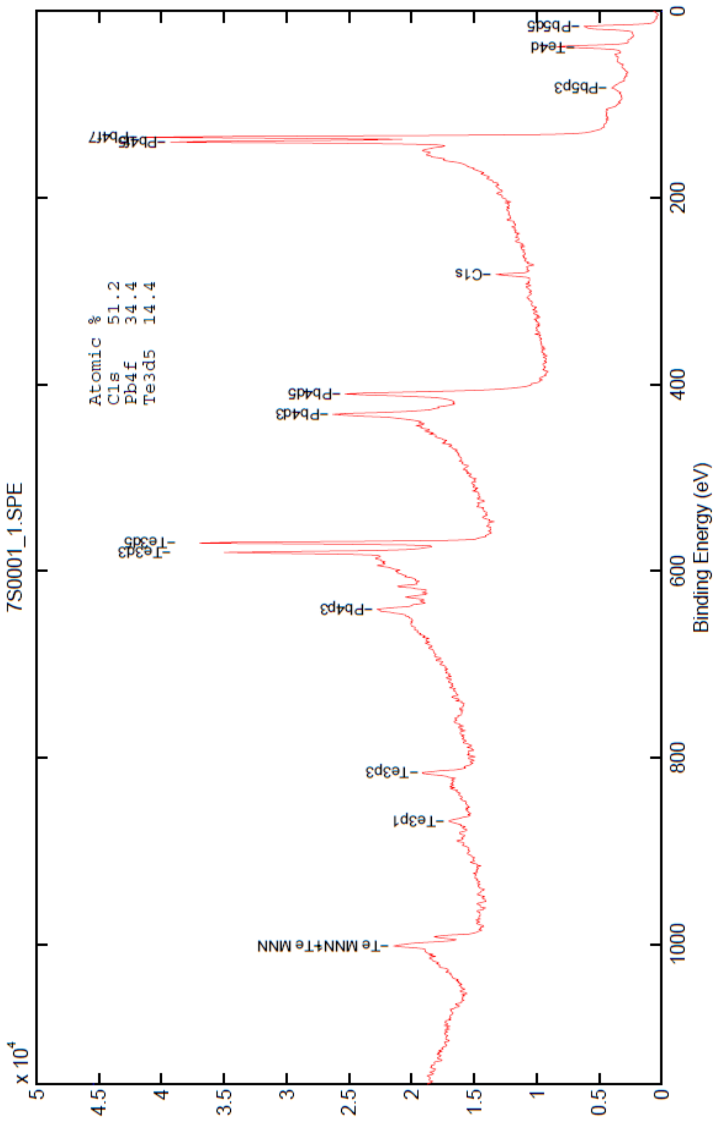

Figure 6.2. XPS spectrum of SynP-PbTe QD.